Acoustic Aberration and Methods for Correction in Transabdominal Histotripsy

by

Ellen M. Yeats

A dissertation submitted in partial fulfillment
of the requirements for the degree of
Doctor of Philosophy
(Biomedical Engineering)
in The University of Michigan
2024

Doctoral Committee:

Research Scientist Timothy L. Hall, Co-Chair
Professor Zhen Xu, Co-Chair
Professor J. Brian Fowlkes
Professor Yun Jing, Penn State University

Ellen M. Yeats

yeatsem@umich.edu

ORCID iD: 0009-0009-5177-1060

Dedication

To my dad, who did not get to see this PhD journey

but who was its most important co-author.

Acknowledgements

The defense of my PhD thesis is a bittersweet moment. The person I most wish I could share the Oral Defense day with cannot be there. My father, Steven A. Yeats, was my first academic mentor. From a young age, he actively instilled a love of learning in me and my brother Eric. He set high expectations but always gave endless support, helping with elementary school math homework and high school essays, science projects and college applications. He was an uncurable engineer and always went over the top helping us with anything academic. I remember that for my first elementary school science project (I was 5), Dad built two huge wooden lever systems that kids could step on to try and lift a cinderblock at the other end, demonstrating the difference between a short and long lever arm. His enthusiasm did not stop there. When I was 13, my 8th grade science teacher gave us an assignment to look at the research page on the website of a major research university and write a summary on one of the featured academic papers. I, of course, decided to try and summarize an impossible paper from a Biology professor at Stanford about molecular transcription and translation mechanisms in cells that I probably could not even understand now. Dad was all for it. We stayed up until 3 AM googling every other word in the abstract and writing an 8-page paper that I'm sure my science teacher did not expect. Dad was always so proud of that paper and even emailed the Stanford professor to show it off. Anyone who knew Dad knew that he

excessively celebrated any little academic achievement that Eric and I ever made. So when I decided to go to the University of Michigan for graduate school, he was over the moon. He was so excited that he started reading papers on our lab website, so much so that I'm positive he knew more about histotripsy than I did when I first committed to the lab.

Dad passed away a few months before I started graduate school. His absence is the hardest thing I have experienced in my life. I had to learn how to motivate myself without him, my biggest cheerleader. I wish more than anything that I could call him and talk to him about my research. This was his dream, and the day I defend my thesis will not be quite the same without him there.

Fortunately, a lot of wonderful people have helped me, even when I really felt like giving up. My mom, Carol Yeats, made sure I got moved up here to Ann Arbor and started my term on time. I would not have made it without her strength and unconditional love. I also thank my brother, Eric, who is currently working on his PhD in something I don't understand (machine learning) at Duke University in the lab of Hai Li and Yiran Chen. He always makes me laugh and was nice enough to entertain the thought of co-authoring a paper (look out for Yeats and Yeats, 2025). Thank you to my *gordo*, Luis, who I met soon after moving here and has been my rock ever since, and to my soul sister Katalya An, for staying by my side all these years. Many thanks as well to the cousins, aunts, and uncles that stepped in to help when Dad passed away and many of whom I have gotten to know better now that I live on the cold side of the country.

In addition to my dad, I have been blessed with some exceptional academic mentors. I would like to thank Zhen Xu for bringing me into the lab and for always being very patient, especially in the early years. I would like to thank Tim Hall for being the best teacher and

mentor I could have asked for. Tim is a patient teacher and always willing to help us students through problems in the lab. Thanks for believing in me (even in the early years, when things were a little rough). I also had some great research mentors before Michigan, including Jorge Camacho (who taught me the basics of ultrasound), Anita Mahadevan-Jansen (my undergraduate research adviser at Vanderbilt), and Christine O'Brien, who was my PhD Student mentor in my undergraduate lab and is now an Assistant Professor at Washington University in St. Louis. All of them helped me gain confidence in the world of research, and I wouldn't be where I am without them. I would also like to thank the other members of my Dissertation committee, Professor Brian Fowlkes and Professor Yun Jing, who have taken time out of their busy schedules to help me with this piece of my academic journey. Thanks as well to all the members of the histotripsy lab from past and present. It has been an honor to work with such kind and talented people. Finally, I want to express my gratitude for being able to play a small part in this histotripsy project. It is an honor to work on a technology with so much potential to improve peoples' lives, and I look forward to seeing how far histotripsy will go in the future.

Table of Contents

Dedication ..... **ii**

Acknowledgements ..... **iii**

List of Figures ..... **x**

List of Tables ..... **xv**

Abstract ..... **xvi**

Chapter 1 Introduction **1**

1.1 Phase Aberration in Ultrasound Imaging and Therapy 2

1.2 Aberration Effects in Transabdominal Histotripsy 4

1.3 Aberration Correction Methods for Histotripsy 7

1.3.1 Aberration Reduction Methods 8

1.3.2 Model-based Aberration Correction Methods 9

1.3.3 Signal-based Aberration Correction Methods 10

1.4 Structure of this Dissertation 17

Chapter 2 Effects of Phase Aberration on Histotripsy in the Human Abdomen **20**

2.1 Introduction 21

2.2 Methods 23

2.2.1 The Suitability of Using a Linear Acoustic Propagation Model 23

2.2.2 Acoustic propagation modelling and validation 26

2.2.3 Evaluation of Aberration using Human Data 29

2.2.4 Investigating Sources of Aberration 34
2.3 Results 35
2.3.1 The Suitability of Using a Linear Acoustic Propagation Model 35
2.3.2 Acoustic Propagation Modelling and Validation 38
2.3.3 Evaluation of Aberration using Human Data 38
2.3.4 Investigating Sources of Aberration 42
2.4 Discussion 43
2.5 Conclusion 50
Chapter 3 Effect of Aberration Correction on the Treatment Envelope for Transabdominal Histotripsy in the Human Liver 52
3.1 Introduction 53
3.2 Methods 54
3.2.1 Human abdominal models 54
3.2.2 Optimization of Transducer Orientation 55
3.2.3 Acoustic Propagation Simulations 58
3.3 Results 61
3.4 Discussion 65
3.5 Conclusion 69
Chapter 4 Aberration Correction of Transabdominal Histotripsy using Cavitation Emissions: *In vitro* study 71
4.1 Introduction 72
4.2 Methods 74
4.2.1 Histotripsy Phased Array 74

4.2.2 Optical and Acoustical Investigation of Histotripsy ACE Signals – Comparison of Bubble Cloud Nucleation and Collapse 76
4.2.3 ACE-Based Aberration Correction 78
4.2.4 Evaluation of ACE-based Aberration Correction with *Ex Vivo* Porcine Tissue 81
4.3 Results 84
4.3.1 Optical and Acoustic Investigation of Histotripsy ACE Signals – Comparison of Nucleation and Collapse 84
4.3.2 Evaluation of ACE-Based Aberration Correction with *Ex Vivo* Porcine Tissue 87
4.4 Discussion 94
4.5 Conclusion 101
Chapter 5 Aberration Correction of Transabdominal Histotripsy using Cavitation Emissions: *In vivo* study 103
5.1 Introduction 104
5.2 Methods 105
5.2.1 Animal handling and *in vivo* experimental setup 105
5.2.2 *In vivo* cavitation-based aberration correction procedure 107
5.2.3 Evaluation of Aberration Correction Efficacy 114
5.3 Results 116
5.4 Discussion 119
5.5 Conclusion 123
Chapter 6 Summary and Future Work 125
6.1 Summary 125
6.2 Outlook and Future Work 127

6.3 Conclusion 135

Appendix 137

A.1 Simulating Focused Ultrasound with k-Wave 137

A.2 Selected k-Wave Scripts 148

References 157

List of Figures

Figure 2. 1. CAD model of the histotripsy phased array considered in this study. Nonlinear acoustic output was measured from the entire array and from each of two 9-element clusters marked in blue. Measurements were acquired at 0, 2, and 5 mm from the geometric focus along the trajectory shown in red.....24

Figure 2. 2. (a) Half-section view of the experimental setup used to validate the segmented tissue acoustic propagation model. Porcine tissue embedded in gelatin was fixed within a bottomless stereotactic box with fiducial markers (dark blue). The box was rigidly and repeatably registered to the histotripsy array using a custom mating fixture (yellow). A waveform from each array element was recorded using a hydrophone at the array geometric focus. (b) MR image slice showing porcine tissue with fat suppression. (c) Image slice after segmentation. White denotes fat. Gray denotes muscle and other non-fat soft tissue. Black denotes water or gelatin. 26

Figure 2. 3. Different transducer (blue) focusing scenarios shown relative to sagittal (left) and coronal (right) views of the abdomen. The yellow dot marks the target site. Scenario 1 focuses through the front of the abdomen with the transducer depth axis normal to the skin surface. Scenario 2 is like Scenario 1 but rotates the transducer around its depth axis (see coronal view). Scenario 3 is like Scenario 1 but tilts the cranial edge of the transducer up away from the skin and the caudal edge of the transducer down (see sagittal view). 32

Figure 2. 4. Pressure waveforms (top) and log-compressed frequency spectra (bottom) acquired at different distances from the focus of the histotripsy transducer using constant source pressure close to the cavitation threshold. Frequency spectra are shown on a 40-decibel scale normalized to the peak amplitude at each distance. 36

Figure 2. 5. Focal waveforms at varying pressure amplitudes (peak rarefactional pressure range: 6 to 14 MPa P^-) from the full transducer aperture and two clusters of 9 elements. 37

Figure 2. 6. Simulated versus measured arrival delays to the geometric focus through abdominal wall tissue. The solid blue line denotes an exact match. The shaded region bordered by two dashed lines denotes error less than one quarter of an acoustic cycle at the central frequency. 37

Figure 2. 7. In all panels, tick marks are spaced 4 cm apart. (a): Aperture map of arrival time differences in the liver of one subject for targeting scenario 3. Differences are mapped as positive and negative delays relative to the median arrival time to the target in units of microseconds and acoustic cycles. The root mean squared delay quantifies the average arrival time difference along the aperture. Portions of the aperture obstructed by air pockets or bone appear as black and gray regions, respectively. (b), (c): Maps of water path length (b) and fat thickness (c) fluctuations for the same targeting scenario. The mapped values represent the local difference from the median. (d): Map of incidence angle to skin surface. 38

Figure 2. 8. (a), (b): Transverse cross section images showing the focus of the pressure field simulated in the liver without (a) and with (b) ideal phase correction. Pressure amplitude is shown on a 20 dB decibel scale normalized to the peak amplitude (0 dB) obtained in the corrected case. (c) One dimensional plots of the pressure along the depth direction, shown with (orange) and without (blue) aberration correction on a 35-decibel scale normalized to the peak amplitude (0 dB) obtained in the corrected case. The origin in all plots is the target location. ..41

Figure 2. 9. Focal pressure amplitude increase (a) and pre-focal shift (b) obtained by changing the sound speed of specific media to match that of non-fat soft tissue (1580 m s^{-1}). Focal pressure increases and pre-focal shifts are averages (means) by targeting scenario. Error bars indicate the standard error associated with each mean. Horizontal bars with asterisks denote statistical significance as determined by Student's t-test for pairs of means using data from all subjects and scenarios (*n*=30). The absence of an asterisk indicates that the relationship was not statistically significant. 43

Figure 3. 1. Couinaud segments of the liver. Image from Sibulesky [174]. 55

Figure 3. 2. Schematic of the simulated histotripsy transducer with 256 equal-area polygon shaped elements.....58

Figure 3. 3. Color-coded maps of the maximum achievable pressure amplitude per sub-volume in the liver of one subject with and without aberration correction. 62

Figure 3. 4. Maximum focal pressure amplitude versus percent blocked aperture for all focusing targets in all subjects, with and without aberration correction. Marker colors denote the Couinaud segment. Shaded regions at the bottom of the plots mark 20 MPa and 30 MPa, the nominal pressure amplitudes required to perform shock-scattering histotripsy and intrinsic threshold histotripsy, respectively.....63

Figure 3. 5. (a) Average focal pressure by liver segment, both with (blue) and without (red) aberration correction. (b) Average percent reduction in the acoustic power input with aberration correction. 64

Figure 3. 6. Treatment envelope for intrinsic threshold histotripsy (volumetric region with maximum focal pressure above 30 MPa) in the liver of each subject according to average aperture blockage (a) and body mass index (b), both with (crosses) and without (dots) aberration correction. Different subjects are shown in different colors.....65

Figure 3. 7. One subject with low average blockage of the liver. The transducer (blue) is shown targeting a location (red) in the liver (purple), which is obstructed by ribs (black) and air pockets (cyan).....67

Figure 3. 8. One subject with high average blockage of the liver. The transducer (blue) is shown targeting a location (red) in the liver (purple), which is obstructed by ribs (black) and air pockets (cyan).....67

Figure 4. 1. (a) CAD model of the receive-capable histotripsy phased array used in this study. **(b)** The experimental setup used to investigate histotripsy cavitation emissions optically and acoustically. The histotripsy array from (a) generated cavitation in de-gassed water behind a sample of porcine abdominal wall tissue. A broadband hydrophone recorded acoustic cavitation emissions at its position 12.1 cm away from the focus and in the focal depth plane. A camera and collimated LED strobe light source acquired optical 'shadowgraph' images of cavitation bubbles and emitted shockwaves.....76

Figure 4. 2. Signals received by the histotripsy array corresponding to cavitation cloud nucleation (top) and collapse (bottom). (a) Signals acquired by 3 elements. The time windows used for cross correlation appear as red rectangular shaded regions. (b), (c) The received wavefield from 1 pulse before (b) and after (c) correction using cross correlation delays. All amplitudes are shown on a normalized scale. 79

Figure 4. 3. Shockwaves from a histotripsy bubble cloud: (a) Hydrophone recordings of emissions from a histotripsy cavitation cloud, spanning nucleation to collapse. (b), (c) Hydrophone recording (b) and shadowgraph image (c) of the bubble cloud nucleation. (d), (e) Hydrophone recording (d) and shadowgraph image (e) of bubble cloud collapse. Cavitation bubbles, emitted shockwaves, and the transmitted pulse wavefront are marked by blue, red, and purple arrows, respectively. 85

Figure 4. 4. Shockwave images (top) and hydrophone recordings (bottom) of bubble cloud nucleation at varying focal pressure amplitudes. In the shockwave images, the direction of sound propagation is from bottom to top. Red arrows mark shockwave profiles. Purple arrows mark the transmitted pulse wavefront.....86

Figure 4. 5. Shockwave images (top) and hydrophone recordings (bottom) of bubble cloud collapse at varying focal pressure amplitudes. In the shockwave images, the direction of sound propagation is from bottom to top. Red arrows mark the shockwave profile. 87

Figure 4. 6. Aberration correction using acoustic cavitation emissions from varying numbers of pulses: (a) Focal pressure amplitude, normalized w.r.t. hydrophone correction, and (b) focal displacement for one tissue sample, obtained using nucleation and collapse corrections computed from 10 individual pulses and from medians of 5, 10, 15, and 20 pulses transmitted at the highest tested transducer power setting. 'No AC' denotes 'no aberration correction.'....89

Figure 4. 7. Comparison of aberration correction using different cavitation emission signals: Bar plots comparing the performance of no aberration correction, hydrophone aberration correction, and acoustic cavitation emissions (ACE)-based aberration correction (AC) using nucleation and collapse at varying transducer power settings. Transducer power is referenced as the peak negative pressure expected at the focus without correction (i.e., 31, 33 and 36 MPa P-). Colored bars denote sample means (n = 7). Error bars denote standard errors. (a) Focal pressure normalized to hydrophone-based aberration correction (HP AC). (b) Estimated focal volume. 90

Figure 4. 8. Focal displacement due to acoustic cavitation emission (ACE) aberration correction (AC): Average displacement of the focus from the aberrated (uncorrected) location, obtained using nucleation and collapse at varying transducer power settings. Transducer power is referenced as the peak negative pressure expected at the focus without correction (i.e., 31, 33 and 36 MPa P^-). Solid color bars denote the magnitude of the shift in the axial (depth) direction. Transparent bars denote the full shift (Euclidean distance between the focus with and without correction). Error bars denote the standard error (*n*=7). 92

Figure 4. 9. Arrival time differences measured using hydrophone, collapse, and nucleation signals: (a), (b), (c) Color-coded array maps of relative element-to-element arrival times measured using hydrophone (a), collapse (b), and nucleation (c) signals. (d), (e) Differences from the hydrophone arrival times for collapse (d) and nucleation (e). 93

Figure 4. 10. Focusing quality with aberration correction (AC): (a) - (d) Cross section maps of the log-compressed pressure field in the transverse focal plane with no aberration correction (a), nucleation-based correction (b), collapse-based correction (c), and hydrophone-based correction (d). Cavitation-based corrections were performed at the highest transducer power setting tested. Maps extend 5 × 5 mm and are centered at the focus (peak amplitude location). 94

Figure 5. 1. (a): Receive-capable histotripsy array with 260 trapezoidal elements arranged in concentric rings. A central port permits insertion of an ultrasound imaging probe for qualitative image guidance. (b): The histotripsy array and a coaxially inserted ultrasound imaging probe were coupled to the pig abdomen via a bath of de-gassed water and repeatably positioned in 3 dimensions by a robotic arm for in vivo experiments. 107

Figure 5. 2. (a), (b) Signals received on all array elements after pulse A (a) and subsequent pulse B (b). (c) Subtraction of pulse B from pulse A. (d) The coherence factor $C[ti]$ calculated at every timepoint of the subtracted signal in (c). 109

Figure 5. 3. (a) The subtracted, time-windowed receive data matrix R containing a collapse shockwave signal and overlying clutter. (b) The product $\boldsymbol{u1v1}*$, which contains only the signal component from collapse. (c) Alignment of R using the phase component of $\boldsymbol{u1}*$**.** Plots show the real part of signals with arbitrary intensity units on a linear scale. 112

Figure 5. 4. Example cavitation probabilities and fitted curves with (blue) and without (red) aberration correction as a function of free-field equivalent focal pressure for one location in the liver of one pig. The green horizontal line marks 50% cavitation probability (the threshold). ..116

Figure 5. 5. (a) Estimated acoustic output from the histotripsy array at the cavitation threshold (50% probability of generating cavitation with a single pulse) for all liver locations in all subjects both with (solid bars) and without (hashed bars) aberration correction. The pressure values represent the peak rarefactional focal pressure amplitude that would be generated at the array focus in the free field at the array power setting required to reach the cavitation threshold in vivo. Pressure amplitudes are de-rated to account for depth-dependent absorption by tissue as described in Section 5.2.3. (b) The percent reduction in acoustic power required to reach the cavitation threshold after aberration correction. *At location 2 in pig 3, cavitation could not be generated at any power setting without aberration correction. The power reduction was estimated by setting the threshold without correction to the de-rated focal pressure at maximum array output. 117

Figure 5. 6. Average spatial deviation of the collapse signal origin from the focus at each liver location. Plotted bars indicate the spatial deviation in the lateral (a) and axial (b) directions, respectively.....118

Figure 5. 7. The average difference between the final correction delay set (computed from the median over 10 collapse signals) and delay sets computed from the median of fewer collapse signals in numbers of acoustic cycles at the central frequency (750 kHz). The red line denotes the mean over locations. The blue area denotes the standard deviation.....119

List of Tables

Table 2. 1. Acoustic properties of sound path components 30

Table 2.2. Sound path statistics for different transabdominal focusing scenarios. 33

Table 2.3: Sound path variation statistics for simulated histotripsy propagation through the human abdomen. Statistics include RMS arrival time difference, RMS water path length fluctuation, RMS fat thickness fluctuation, and median incidence angle across the aperture. Mean values (bold font) and standard deviations (in parentheses) summarize each statistic across all subjects and by targeting scenario. 40

Table 2.4. Focusing quality for simulated transmission through the human abdomen. Mean (bold font) and standard deviations (in parentheses) of the focal pressure amplitude increase from aberration correction and the pre-focal shift with and without aberration are reported for each targeting scenario and across all subjects. 42

Table 3. 1. Couinaud segments 55

Table 3. 2. Acoustic properties of sound path components 60

Abstract

Histotripsy is a non-invasive, non-thermal ablation technique that focuses high-pressure, short-duration ultrasound pulses into the body to mechanically destroy tissues via acoustic cavitation. Histotripsy has been used to selectively ablate tumors in many abdominal and pelvic organs, including the liver, kidney and prostate. Notably, histotripsy was recently awarded FDA clearance for the non-invasive treatment of liver tumors.

Generation of the cavitation bubble cloud for histotripsy therapy requires a large rarefactional pressure amplitude at the acoustic focus. However, the ability to generate large pressure amplitudes is limited by phase aberration, or acoustic defocusing in heterogeneous tissues. Spatial variations in the speed of sound throughout tissue cause converging ultrasound waves to accumulate phase errors that shift, broaden, and weaken the focus. These focal changes hinder the safety and efficacy of histotripsy therapy, especially at deep-seated or highly obstructed regions of the liver. By limiting the range of feasible treatment locations for histotripsy, phase aberration restricts the number of patients who can receive treatment.

The first part of this Dissertation develops a computational model to investigate phase aberration effects for a histotripsy transducer focusing through the human abdomen. The model was experimentally validated with *ex vivo* porcine abdominal wall. Simulations show that

human abdominal tissues can severely aberrate the histotripsy focus. Importantly, the results indicate that correcting phase aberration could substantially increase focal pressure amplitude to expand the average treatment envelope (range of feasible treatment locations) from 50% to 75% of the liver.

The second part of the Dissertation develops a method for abdominal aberration correction (AC) based on using the histotripsy transducer to receive the acoustic emissions from cavitation cloud collapse. The phase errors from aberration were detected using the received signals and compensated to correct aberration. *In vitro* studies with excised porcine abdominal wall show that the collapse-based aberration correction method can restore nearly all focal pressure amplitude lost to aberration. For implementation *in vivo*, signal processing strategies were developed to enable robust, effective collapse-based AC in the presence of abdominal signal clutter and respiratory motion. *In vivo* experiments in a swine model showed that the collapse-based AC method reduces the acoustic power required to generate cavitation in the liver by up to 54% (average: 24%).

All simulations and experiments were performed with a histotripsy transducer of similar dimensions to the current clinical device. Together, the results of these investigations indicate that aberration correction is feasible and could substantially increase the efficacy, efficiency, and safety of transabdominal histotripsy therapy. Importantly, aberration correction could allow histotripsy treatment at more locations in the liver and in more diverse body types, thus enabling non-invasive, non-thermal histotripsy treatment for a broader population of patients.

Chapter 1
Introduction

This dissertation investigates the effects of acoustic phase aberration on histotripsy (a soft tissue ablation technique based on ultrasound) and develops methods for histotripsy aberration correction. The dissertation specifically considers aberration by tissues of the abdomen, which is the target region for the first clinical histotripsy treatments. This first chapter of the dissertation introduces phase aberration and histotripsy, reviews relevant prior work on these topics, and motivates the research presented in remaining chapters by discussing the knowledge and technologies required to advance the clinical implementation of aberration correction for transabdominal histotripsy.

*Note: portions of this chapter were published as listed below.

1. **Yeats E**, Gupta D, Xu Z, Hall TL. Effects of phase aberration on transabdominal focusing for a large aperture, low f-number histotripsy transducer. Physics in Medicine & Biology. 2022 Jul 19;67(15):155004.
2. **Yeats E,** Hall TL. Aberration correction in abdominal histotripsy. International Journal of Hyperthermia. 2023 Dec 31;40(1):2266594.
3. **Yeats E**, Lu N, Sukovich JR, Xu Z, Hall TL. Soft Tissue Aberration Correction for Histotripsy Using Acoustic Emissions From Cavitation Cloud Nucleation and Collapse. Ultrasound in Medicine & Biology. 2023 May 1;49(5):1182-93.

1.1 Phase Aberration in Ultrasound Imaging and Therapy

As the sound field from a spatially distributed acoustic source propagates through the body, wavefront phase errors accrue due to varying speed of sound for different bodily tissues and heterogeneous propagation paths [1]. Tissue boundaries that are not normal to the direction of propagation also cause refraction of an acoustic beam [2]. These effects will be collectively referred to as 'phase aberration' in this Dissertation. Phase aberration has a significant adverse effect on ultrasound imaging. Accrued phase errors undermine constructive interference, producing a weakened, blurred imaging focus and thereby compromising contrast and spatial resolution [3]–[5]. At the typical frequencies (≥3 MHz) used to image tissue, even small inhomogeneities (such as muscle striations) can severely distort the focus [6]. To address this problem, the field of ultrasound imaging has developed methods for aberration correction (AC). Broadly, AC estimates wavefront phase errors by maximizing correlations among backscattered ultrasound signals [1], [7]–[11], updating phase estimates to optimize measures of focusing quality [12], [13], or estimating the local sound speed distribution [14]–[16]. AC has been shown to improve image contrast and resolution by strengthening and narrowing the focus [17].

Therapeutic ultrasound (TU) typically uses lower frequencies (≤1.5 MHz) than ultrasound imaging. Therefore, phase aberration from small intra-tissue inhomogeneities is significantly reduced. However, TU studies nonetheless report a considerable aberration effect from intervening soft tissues. Breast, abdominal and pelvic tissues can induce large phase errors that distort the shape, shift the location, and reduce the intensity of the TU focus [18]–[26].

These focal changes can hinder therapy, reducing its efficacy, efficiency, and safety by necessitating increased source output to reach a required focal intensity. Clinical studies of High Intensity Focused Ultrasound (HIFU) in the kidney reported that treatments failed in some patients despite low obstruction from bone [25]. The failed treatments were later attributed to de-focusing by thick layers of abdominal fat [24], [27], [28]. Similarly, Khokhlova et al found that TU treatments in porcine liver failed in some subjects due to aberration induced by the abdominal wall [29]. This substantial soft tissue aberration effect has been attributed to the large aperture and strong curvature (f-number ≤ 1.5) of TU transducers [26], [30]. Due to the large transducer aperture, the TU beam passes through a large tissue volume. Throughout this large volume, tissue morphology and travel distances through individual tissues to the focus can vary extensively. As a result, sound waves can take varying paths to the focus, causing phase errors [26]. The strong curvature of the transducer creates large angles of incidence. Sound waves from outer portions of the transducer can therefore refract strongly at tissue boundaries, deviating the TU beam [30].

These observations suggest that TU transducer geometry could increase the aberration caused by large-scale tissue features, thereby degrading the focus despite the use of low acoustic frequencies. This situation opposes that of ultrasound imaging, where small-scale internal tissue structures dominate focal distortion effects [6]. This difference may result from the contrasting frequencies and transducer geometries used. High imaging frequencies are sensitive to small-scale inhomogeneities, while lower therapeutic frequencies are not. Along small, flat imaging transducer apertures, tissue path variations and incidence angles are moderate; however, along large, curved TU apertures, path differences and refraction can be

extreme. Thus, although the mechanism of aberration in TU differs from US imaging, the resulting focal distortion can be substantial.

1.2 Aberration Effects in Transabdominal Histotripsy

Histotripsy is a therapeutic ultrasound technique that uses ultrasound-induced cavitation to mechanically destroy soft tissues [31]. Specifically, histotripsy focuses high amplitude (peak rarefactional pressure amplitudes >20 MPa), short (microseconds-duration) ultrasound pulses repeated at low duty cycle (typically <1%) into the body to generate a finely controlled, localized cloud of small (millimeter sized) inertial cavitation bubbles that expand and contract to rupture adjacent cells [32]. The cavitation cloud can be generated directly by a local rarefactional pressure exceeding the intrinsic threshold for cavitation bubble nucleation (‘intrinsic threshold’ histotripsy) [33] or indirectly via shock scattering, where the ultrasound pulse reflects at the cavitation surface and undergoes phase inversion to add to the rarefactional pressure of subsequent incoming cycles (‘shock scattering’ histotripsy) [34]. Histotripsy is non-invasive, non-ionizing, and non-thermal and thus avoids comorbidities from incision, radiation, and thermal damage, making histotripsy an attractive alternative to other tissue removal methods like surgery, solid beam radiation therapy, and thermal ablation [35]. Furthermore, unlike thermal methods which are susceptible to heat dissipation, histotripsy permits precise control of the ablation zone, producing sharp, sub-millimeter margins that often bisect individual cells [36]. Histotripsy has been used to selectively ablate tissue in the brain, heart, liver, kidney, and prostate [37]–[47]. Notably, histotripsy recently completed

multi-center clinical trials in the US (NCT04572633) and Europe (NCT04573881) and has received FDA approval for the treatment of liver tumors.

Early in its development, histotripsy was considered 'resilient' to aberration. This idea of resiliency arose because histotripsy was shown to generate precise lesions in the presence of strong aberrations from skull and ribs [48]–[50]. Diffraction through ribs can distort and split the ultrasound focus into multiple 'grating' lobes for long or continuous exposures as in High Intensity Focused Ultrasound (HIFU) [51]–[55], causing collateral damage (necrosis outside of the main focal lobe) [56]. The short pulses used in histotripsy greatly reduce the amplitude of grating lobes [57]. Additionally, histotripsy is governed by a threshold mechanism, which restricts the generation of cavitation (and thus any damage) to regions where the pressure exceeds a critical amplitude (>28 MPa) [58], [59]. Therefore, histotripsy lesions can be created without collateral damage by setting the transducer power output such that only the main focal lobe exceeds the cavitation threshold while any secondary lobes remain below the cavitation threshold [48], [60]. For these reasons, aberration correction appeared to be less critical for histotripsy than for other TU modalities. Aberration from soft tissue was considered even less critical. The differences in the speed of sound among soft tissues are relatively modest (<10%) [61]. Additionally, histotripsy uses relatively low ultrasound frequencies (usually ≤1 MHz) [35], [62]. Arrival time variations in soft tissue were assumed to be much shorter than an acoustic cycle and thus unlikely to cause significant aberration effects.

However, as histotripsy began *in vivo* studies in large animal models, observations suggested that soft tissue phase aberration could strongly decrease histotripsy focusing quality despite low frequencies [49], [63]. In one study, cavitation could not be generated at targets

deep below the skin. The observed attenuation exceeded the loss that would be expected for absorption alone, suggesting that phase aberration from heterogeneous abdominal layers significantly decreased the focal pressure amplitude [64]. Additionally, *in vivo* transabdominal histotripsy studies have reported 1-5 mm shifts in the location of the bubble cloud away from the target, suggesting that refraction shifted the focus [49]. These focal changes could have important consequences for histotripsy therapy. For tissue targets located at-depth or heavily obstructed by bone and air pockets, aberration could combine with ultrasound absorption and reflection to severely attenuate focal pressure, limiting the size and density of the cavitation cloud [60] or preventing treatment altogether [64]. At shallow, accessible tissue targets, increasing the transducer output power could compensate reduced pressure amplitude, enabling therapy despite strong pressure loss from aberration. However, due to the decreased focal gain, the energy deposited in intervening tissues could also increase, elevating the risk for adverse effects like tissue heating. Additionally, for fine tissue targets like small liver tumors (<20 mm), the focal shift could cause a significant targeting error [65]. Therefore, soft tissue aberration could substantially reduce the efficacy, safety, and accuracy of histotripsy therapy. Furthermore, soft tissue aberration, particularly in transabdominal applications, may be more severe for histotripsy than other therapeutic ultrasound (TU) techniques because histotripsy transducers have especially large aperture and strong curvature (f-number ≤1) [66].

The effects of aberration on transabdominal histotripsy have been observed in animals [49] and animal tissues [63] but have not been studied in humans. Knowledge of aberration effects in human tissues will be critical to assessing the need for aberration correction in clinical transabdominal histotripsy treatments and to developing effective aberration correction

methods. It is currently unknown how much aberration limits the treatment envelope (range of feasible treatment locations) for histotripsy in the human abdomen. Quantification of the treatment envelope with and without aberration correction would help determine the clinical benefit of implementing aberration correction, which adds to the cost and complexity of treatments. The first part of this thesis develops and validates a simulation-based model to investigate aberration effects for a histotripsy transducer focusing through the human abdomen (considering the geometry of the current clinical histotripsy device). The model is used to quantify the treatment envelope in the human liver.

1.3 Aberration Correction Methods for Histotripsy

Aberration can be corrected by subdividing the aperture of the histotripsy transducer into an array of smaller transducer elements (a 'phased array') and adjusting the transmission phase of each element to compensate spatially varying phase differences, which are determined using one of two groups of methods [67]–[69]. The first group maps the speed of sound distribution in tissue (typically with pre-operative medical imaging) and feeds this map into a numerical acoustic propagation model to predict the phase errors accumulated along the path to the target. These methods are called 'model-based methods' in this dissertation. The second group, here called 'signal-based methods,' use the histotripsy array to sense the acoustic signals that backpropagate from the focus and thereby measure the phase differences between elements. These aberration correction approaches, as well as some earlier work on 'aberration reduction', are reviewed in the following sub-sections.

1.3.1 Aberration Reduction Methods

Aberration correction for histotripsy requires a phased array of many elements (typically >100) and phase detection strategies based on modelling acoustic propagation or receiving ultrasound signals on the array elements. To avoid this additional complexity, some early work sought not to correct but to reduce aberration by modifying the frequency content of the therapeutic ultrasound beam [70]–[72]. Lower frequency waves are less susceptible to decorrelation in heterogeneous tissue than higher frequencies and thus maintain greater coherence in the presence of aberration [73]. However, higher frequencies are desirable because they produce a smaller focus and thus enable selective spatial targeting of the therapy. White et al [71] and later Lin et al [72] proposed to combine these properties by specially designing the therapy beam. White et al took advantage of nonlinear propagation effects to convert the energy of the therapy beam from the fundamental frequency (272 kHz) to the second harmonic (544 kHz) at a point between the nearfield and focus [71]. As a result, the therapy beam propagated through the aberrating region (*ex vivo* human skull) at low (272 kHz) frequency and then focused in the target region at higher frequency (544 kHz). The focus of this nonlinearly propagated beam showed reduced aberration effects (improved focal symmetry) compared to simple linear propagation of a 544-kHz source. In another approach developed specifically for histotripsy, Lin et al combined low and high frequencies by direct linear summation of two confocal sources, each transmitting at subtherapeutic amplitude such that only the summed amplitude at the focus exceeded the cavitation threshold [72]. The idea was to deliver one portion of the beam energy at a lower frequency and thus mitigate attenuation

from absorption and aberration. The other portion was delivered at higher frequency to restrict the focus size and thus maintain spatial selectivity of histotripsy therapy. Proof-of-concept was demonstrated for these 'aberration reduction' techniques by simulation and by experiments *in vitro* [71], [72]. However, these techniques only modestly improve the focal pressure (White et al achieved a maximum transcranial focusing gain of 60% [71]) and in general do not correct the focal shift.

1.3.2 Model-based Aberration Correction Methods

Prior to transabdominal histotripsy treatment, the target tissue (e.g., tumor) is identified on pre-operative MRI and/or CT images [74]. These images provide an anatomical reference to the clinician during histotripsy therapy, which is performed under B-mode ultrasound guidance [75]. Unlike the ultrasound images, the MRI and/or CT images provide 3-D anatomical maps with sufficient soft tissue resolution to differentiate among major tissue types (e.g., skin, fat, muscle, organs). Therefore, if each tissue is assigned appropriate acoustic properties, these 3-D maps can be input to a numerical acoustic propagation to predict the path of the histotripsy beam through the abdomen and thereby estimate phase errors for aberration correction. This "model-based" approach has been applied successfully to correct phase aberration through the skull for histotripsy and HIFU [76]–[84] and to minimize energy deposition at the ribs during transcostal HIFU [85]–[91]. Model-based aberration correction methods incorporating aberration from abdominal soft tissues have been proposed but have remained largely theoretical due to the challenges that elastic soft tissue deformation and organ shift pose to image registration [92], [93]. Unlike rigid skull and ribs, which can be repeatably registered to a

pre-operative image, soft tissues and organs readily shift and deform, thereby altering the tissue path and invalidating the phase estimates obtained from the numerical model.

Importantly, while model-based aberration correction methods are effective for correcting focal shift, they may not substantially increase pressure amplitude at the focus. The phase errors that decrease pressure amplitude must be known with high accuracy to maximize focal coherence [92]. Medical images have limited spatial resolution (often >λ/2 at typical histotripsy wavelengths) and soft tissue resolution (ability to distinguish tissues beyond major types like muscle, fat, etc.), which limit the resolution of fine tissue features. Additionally, published values for acoustic properties vary substantially, and it is possible that this variance is intrinsic [94]. Sound speed estimates derived from CT Hounsfield units are prone to system-specific bias [95]. Therefore, model-based approaches are unlikely to predict phase with sufficient accuracy to maximize coherence at typical histotripsy frequencies.

1.3.3 Signal-based Aberration Correction Methods

Signal-based aberration correction methods aim to determine phase errors by receiving ultrasound signals from the focus. Unlike model-based methods, signal-based methods make direct acoustic measurements and thus avoid errors from modelling and co-registration. Also, acoustic data collection can be very fast and potentially interleaved with therapy emissions to update the aberration correction for focusing at different locations within a large treatment volume. Signal-based methods were first developed for aberration correction of ultrasound imaging [1], [7], [8], [12], [96] and were extended to therapeutic ultrasound and histotripsy following the introduction of receive-capable therapeutic arrays [97]–[100]. Signal-based

methods can be divided into two categories based on the type of signals used for correction. These are ultrasound speckle signals and signals from bubbles (contrast agents or cavitation). Correction methods based on each signal type are discussed below.

1.3.3.1 Ultrasound Speckle Signals

The ideal signal for aberration correction is a point source or beacon [1], [7]. Beacon signals have high spatial coherence and deterministic phase and thus enable accurate determination of the element-to-element phase differences from just one signal acquisition [1]. However, beacons are rarely available endogenously in biological tissue. The most common signal source is scattering of the ultrasound beam by sub-wavelength reflectors within tissues ("speckle") [101]. Speckle signals originating from the beam focus can be used for aberration correction but have limited spatial coherence and stochastic phase. Consequently, the speckle signals on spatially distant array elements have low covariance, hindering the determination of the element-to-element phase differences [102]. The spatial coherence of speckle depends on the focal spot size and thus decreases with acoustic frequency [102]. Therefore, aberration correction based on speckle signals is especially challenging for low-frequency modalities like histotripsy.

Thomas et al addressed the challenge of low speckle coherence for histotripsy by taking advantage of nonlinear effects at the focus and by iteratively estimating the phase differences [103]. The large pressure amplitudes employed in histotripsy produce strong nonlinear effects including the generation of harmonic frequencies at the focus [104]. The resulting harmonic echoes have a smaller focal spot size than the fundamental frequency and thus increase the spatial coherence of speckle [105]. To increase the signal-to-noise ratio of the harmonic echoes,

Thomas et al employed a pulse-inversion scheme, transmitting two pulses of opposite polarity with a 1.5-MHz boiling histotripsy array and receiving the amplified second harmonic (3-MHz) on the therapy elements [103]. Then, the spatial coherence at the focus was improved iteratively by estimating the phase differences from the received speckle, re-transmitting with phase correction, and repeating. Iterative correction progressively decreased the focal spot size and improved the covariance of the received signals until converging at an optimal phase correction, restoring the focal pressure amplitude and focusing quality to unaberrated levels when focusing through an abdominal wall phantom *in vitro*. The technique was later applied in vivo and successfully reduced the acoustic power required for therapy in the pig by up to 45% [106].

For effective convergence of the iterative estimation technique, every signal acquisition must represent the same group of sub-wavelength reflectors. In vitro, convergence was achieved after 7.6 iterations on average, requiring ~7.6 s total [103]. However, convergence is complicated in vivo by tissue motion. Movement from respiration cyclically alters the position of the focus in tissue and thus varies the distribution of sub-wavelength reflectors contributing to the speckle signal. To converge in the presence of tissue motion, each iteration must acquire speckle signals from the same point in the breath cycle (i.e., the same group of reflectors). In vivo, speckle signals were acquired over a duration >1 breath cycle at each iteration to track and identify the signals corresponding to the same group of reflectors, slowing the iteration rate to below the respiration rate [106]. For each focus location, the iterative estimation converged in ~1 minute on average. This convergence time is clinically acceptable if the correction procedure is required at only a few different focus locations but may become

unacceptably long if phase estimation is required at many locations (e.g., over a large treatment volume).

To perform speckle-based aberration correction without iteration, Herbert et al indirectly estimated the aberration phases via measurements of the focusing quality, building on earlier work from ultrasound imaging [12], [13]. Instead of directly comparing signals between elements to estimate phase differences, Herbert et al measured the focusing quality as a function of different orthogonal combinations of element phase in transmission and then inverted the relationship to solve for aberration phase errors using a linear best fit [107]. Each orthogonal combination of element phase was encoded into one pulse transmission of the therapy array. (A total of 4N pulses were required, where N is the number of array elements). Focusing quality was measured non-invasively by receiving speckle signals from the focus and detecting spatial shifts of the tissue due to the acoustic radiation force, which is proportional to the focal pressure amplitude [108], [109]. Using this technique, Herbert et al demonstrated reduction of the element-to-element phase differences and improved focusing through an aberrating phantom in vitro. However, the technique has significant challenges that limit its applicability to histotripsy in vivo. First, in vivo tissue clutter can reduce the signal-to-noise ratio of speckle signals received from the focus and may therefore hinder the measurement of acoustic radiation force displacements [5], [110]. Second, the displacements from the acoustic radiation force are very small (<0.1 mm) and difficult to distinguish from tissue motion. For in vivo implementation, tissue motion would have to be removed from signals by applying a high-pass filter across pulses or compensated by gating each phase encoded pulse with the

respiratory and/or cardiac cycles. For a typical histotripsy array with >100 elements, the latter approach would quickly become intractable (given that 4N emissions are required).

1.3.3.2 Signals from Bubbles

Due to the challenges of aberration correction with speckle signals, researchers have proposed to place a beacon signal at the focus by introducing a bubble [111]–[114]. Signals from bubbles (scattering and emissions) approximate point sources and thus allow phase measurement without iteration and by direct comparison of the received signals across elements [1]. Bubbles can be introduced via intravascular injection (*e.g.*, contrast agents like microbubbles or droplets) or by using the histotripsy array to generate inertial cavitation at the focus.

In the first method, chemically stabilized gas bubbles or bubble-forming droplets are injected, arrive at the target tissue through the bloodstream, and are then insonified by low (subtherapeutic) amplitude pulses from the transducer [115]–[118]. If the bubbles are small compared to the ultrasound wavelength, the backscattered waves from the bubbles appear omnidirectional to the array and can thus act as an effective beacon [119]. Notably, Haworth *et al* formed bubbles at the focus by vaporizing injected liquid droplets with ultrasound pulses and then received backscatter from the bubbles to correct for phase differences induced by *ex vivo* human skull [120]. Similarly, phase aberration correction with microbubble contrast agents has been applied to improve transcranial ultrasound imaging of cerebral vasculature [121]–[126]. One advantage of using droplets or contrast agents is that beacon-like echoes can be obtained using low amplitudes (does not require large focal pressure amplitude at the focus) [127]. The

primary disadvantage of these techniques for histotripsy is that they require an otherwise unnecessary injection.

Beacon signals for aberration correction can also be introduced non-invasively by generating cavitation at the focus. Inertial cavitation bubbles emit acoustic signals corresponding to their initial nucleation (formation), oscillation, and eventual collapse (termination) [128]–[130]. These acoustic emissions can be received to serve as beacon signals for AC. Notably, the nucleation and collapse of histotripsy bubble clouds produce highly broadband shockwave signals that propagate spherically out from the focus and thus approximate an ideal point source [131], [132]. Pernot *et al* first proposed to correct aberration with acoustic cavitation emissions and demonstrated proof-of-concept for an US imaging transducer focusing through an aberrating phantom [111]. The cavitation-based correction restored focusing quality to non-aberrated levels. Continuing this work, Gateau *et al* used a therapeutic US transducer to generate cavitation and receive the resulting emissions for transcranial phase correction [133]. The cavitation-based correction closely matched the AC performance of a hydrophone (the laboratory gold standard), increasing the focal pressure to 95% of the hydrophone-corrected amplitude on average with a standard deviation over 60 trials of 1%. This method was later applied specifically to histotripsy for aberration correction through *ex vivo* human skull [84] and porcine abdominal wall [134].

Like other signal-based methods, cavitation-based correction methods cannot correct focal shift, because the signals used for correction originate from the aberration-shifted focus. However, cavitation-based AC can substantially increase the focal pressure amplitude and the focusing quality to improve treatment efficacy and efficiency. Cavitation signals could also have

significant advantages over speckle signals for aberration correction of transabdominal histotripsy. Abdominal tissues move constantly due to respiratory and cardiac activity and thus extend the time required for iterative speckle-based methods to converge. Tumors in abdominal organs often exceed 3 cm in diameter [135] and require re-focusing the histotripsy beam at multiple locations within the tumor for complete ablation [136]. Aberration correction at multiple locations with a speckle-based method would significantly extend the total procedure time. Furthermore, updating the correction throughout treatment would be intractable. Cavitation-based aberration correction permits accurate phase estimation without iteration and could therefore substantially reduce the time required for correction. Additionally, cavitation-based AC may allow updates of the phase correction in 'real-time' (at the treatment pulsing rate) to adapt to any shifts or deformations of abdominal tissues.

In a preliminary in vitro study by Macoskey et al, transabdominal cavitation-based AC attained only 77% of the focal pressure amplitude achieved by the gold standard (hydrophone) correction [134]. This relatively modest performance was hypothesized to result from the type of emission signal used. Specifically, Macoskey et al considered the emission from bubble cloud nucleation, a relatively large-amplitude signal that permitted detection with a low-sensitivity receiver. One limitation noted was that, during nucleation, each bubble forming the cloud emits a shockwave. Because neighboring bubbles were separated by less than a wavelength (at 500-kHz receiver frequency), the emitted shockwaves overlapped as they propagated outwards, precluding the isolation of a single shockwave for phase correction. To reduce this ambiguity, Macoskey et al estimated phase differences by detecting the leading edge of the first-arriving shock wave. However, the edge detection method was highly sensitive to amplitude variations

and consequently added error to the phase estimates. Also, isolation of the first-arriving shockwave introduced a systematic, 2 – 3-mm post-correction shift of the focus towards the transducer.

Recent improvements in the sensitivity of histotripsy transducer receive hardware have enabled the detection of smaller-amplitude bubble emissions such as the collapse signal [131], [137]. Collapse emissions may have advantages as acoustic beacons. Bubble clouds often collapse concertedly, emitting a single shock wave from the cloud center (the focus) [138]–[140]. Unlike the superimposed nucleation shock waves, the collapse shock wave approximates an ideal point source, suggesting its suitability as a beacon for histotripsy AC.

The second part of this dissertation investigates the feasibility of using the collapse signal for transabdominal histotripsy aberration correction. Signal processing methods are developed to enable robust and fast cavitation-based AC in the presence of abdominal signal clutter and tissue motion in vivo. The efficacy of cavitation-based AC is then evaluated in an in vivo swine model.

1.4 Structure of this Dissertation

This Dissertation aims to improve histotripsy treatments by investigating the effects of aberration on transabdominal focusing and developing methods for transabdominal aberration correction. This research includes 2 parts. The first part investigates the effects of phase aberration on histotripsy in the human abdomen. Specifically, a computational model is developed and validated to simulate focusing of a large aperture, low f-number histotripsy transducer through human abdominal tissues. The model is applied to assess the effect of

aberration correction on the treatment envelope for transabdominal histotripsy in the liver. This work is presented in Chapters 2 and 3. The second part of the Dissertation develops a method for transabdominal histotripsy aberration correction based on receiving the acoustic emission from cavitation cloud collapse. *In vitro* experiments in Chapter 4 show that correction with the collapse emission approximates the correction performance of a true point source. Experiments with a live swine model in Chapter 5 demonstrate that the correction method is robust and effective despite abdominal signal clutter and respiratory motion *in vivo*. Each chapter of the Dissertation is summarized below.

Chapter 1 introduces acoustic phase aberration and its effects on transabdominal histotripsy, reviews prior work on aberration and correction methods for transabdominal therapeutic ultrasound, and motivates the work presented in subsequent chapters.

Chapter 2 develops and experimentally validates a computational model of a large aperture, low f-number histotripsy transducer focusing through abdominal tissues. Simulations with human data indicate that aberration correction could substantially increase focal pressure amplitude and focusing quality for transabdominal histotripsy therapy.

Chapter 3 applies the model developed in Chapter 2 to quantify the effects of transabdominal aberration on focusing as a function of location in the human liver. This study provides the first quantitative estimates of the treatment envelope for transabdominal histotripsy in the liver, both with and without aberration correction. The results suggest that aberration correction could substantially expand the range of feasible treatment locations for transabdominal histotripsy in the liver.

Chapter 4 develops a method for histotripsy aberration correction based on receiving the acoustic emissions from cavitation and evaluates its efficacy *in vitro* with excised porcine abdominal wall. The study compares the AC performance of acoustic signals from cavitation cloud nucleation and collapse. The results indicate that the cavitation-based method with the collapse signal closely matches the AC performance of a hydrophone (the laboratory gold standard method).

Chapter 5 develops signal processing methods to enable robust, effective AC using the low-amplitude collapse signal in the presence of high-amplitude abdominal signal clutter and respiratory motion *in vivo*. The methods are validated in an *in vivo* swine model targeting the liver.

Chapter 6 first discusses how the Dissertation research furthers knowledge of aberration effects in transabdominal histotripsy and improves upon prior AC methods by taking advantage of the collapse emission, a pseudo-point source. Then, the final chapter outlines the remaining work needed to improve focusing in transabdominal histotripsy and advance aberration correction methods to the clinic.

Chapter 2
Effects of Phase Aberration on Histotripsy in the Human Abdomen

The effects of phase aberration on acoustic focusing in transabdominal histotripsy are not well known. This Chapter develops and validates a computational model to investigate how phase aberration from human abdominal tissue affects focusing of a large, strongly curved histotripsy transducer. The findings suggest that human abdominal tissues can severely aberrate histotripsy sound fields despite low therapeutic frequencies. Additionally, the simulations show that different heterogeneity sources distinctly affect focusing quality. The water path strongly affects the focal shift, while irregular tissue boundaries (e.g., fat) dominate pressure loss.

*Note: This chapter was adapted from the publication listed below.

1. **Yeats E**, Gupta D, Xu Z, Hall TL. Effects of phase aberration on transabdominal focusing for a large aperture, low f-number histotripsy transducer. Physics in Medicine & Biology. 2022 Jul 19;67(15):155004.

2.1 Introduction

Aberration effects have been observed in transabdominal histotripsy treatments but have not been investigated quantitatively. For instance, the bubble cloud has been observed to shift away from the target and closer to the skin by several centimeters due to refraction. In treatment planning, this shift is estimated using an empirically derived linear relationship with target depth and compensated by moving the transducer closer to the skin by the predicted distance. However, the prediction error of the empirically derived relationship is large compared to the magnitude of the focal shifts, indicating that a simple linear relation with target depth may not be sufficient to predict focus shift and suggesting the need for further study. It has also been noted that the input energy required to generate cavitation for histotripsy varies substantially from patient to patient. It is not known how much of this variation results from aberration. Therefore, it is not known how much of the required input energy could be reduced with aberration correction. Systematic, quantitative study of transabdominal aberration effects will be critical to guiding treatment planning strategies and technological development as clinical adoption of histotripsy grows.

Because aberration cannot be directly measured in human patients, most measurements of aberration effects in therapeutic ultrasound are from phantoms [141], [142] or animal tissues [22], [24], [29], [30], [143]. Phantoms can oversimplify the heterogeneity of biological tissues. Animal tissues can have similar composition to human tissues but often have a very different spatial conformation due to anatomical differences, thereby limiting their validity as models for aberration effects in people. To avoid these limitations, some researchers have used excised

tissues from human donors to study aberration effects in ultrasound imaging [6], [144]. However, excised tissues lose their *in vivo* spatial conformation. For a large aperture, therapeutic ultrasound transducer, which intersects a large region of the body, the relative spatial arrangement of tissues strongly influences the observed aberration. Therefore, excised human tissues cannot fully represent aberration in the intact human body during histotripsy therapy.

An alternative is to model aberration effects using computational simulation. Simulations permit study of human tissues in their native conformation and have been used to study aberration effects in therapeutic ultrasound, including in the brain, breast, liver, kidney, and uterus [20], [28], [80], [82], [92], [145]. However, these studies are specific to HIFU therapy. Histotripsy has different features from HIFU that may cause distinct aberration effects. First, unlike HIFU, which uses continuous ultrasound waves, histotripsy uses short pulses. Therefore, histotripsy aberration does not result from relative phase errors but rather from absolute arrival time differences that can exceed one acoustic cycle. Second, histotripsy transducers typically have larger aperture and lower f-number than HIFU transducers. As discussed in Section 1.2, these features can increase aberration effects. The large aperture expands the ultrasound beam, which causes it to intersect a larger and more heterogeneous tissue volume, while the large curvature increases angles of incidence between the transducer and tissue, increasing refractive aberrations [30], [86]. Therefore, studies of aberration specific to histotripsy are required.

The present study aimed to investigate the effects of phase aberration from the human abdomen on a large aperture, low *f*-number histotripsy transducer. We focused our study on

histotripsy treatment of the liver and considered the geometry of the transducer currently in clinical use. Our approach was first to experimentally validate a computational acoustic model (k-Wave) with *ex vivo* porcine abdominal wall tissue. Then, we apply the validated model to simulate acoustic propagation through segmented abdominal computed tomography (CT) scans of human subjects. Currently, efficient methods to simulate nonlinear acoustic propagation in heterogeneous media to the degree required by histotripsy are unavailable [146]. We hypothesized that a linear propagation model would be sufficient to model phase aberration of the rarefactional pressure field, which governs histotripsy cavitation for this scenario. Specifically, that nonlinear propagation effects do not significantly change the arrival time of the peak rarefactional pressure to the focus. We evaluated this hypothesis for the transducer simulated herein in Section 2.2.1 of the Methods. Next, we validated the simulation by comparing simulated propagation delays to hydrophone measurements through a block of heterogeneous *ex vivo* tissue in part Section 2.2.2. Finally, in Sections 2.2.3 and 2.2.4, we applied the validated model to perform acoustic simulations for three target locations in each of ten human subjects. The purpose of the human abdominal simulations was (1) to evaluate how phase aberration affects histotripsy focusing quality through human abdominal tissue and (2) to assess how specific components of the transabdominal sound path affect focal distortion.

2.2 Methods

2.2.1 The Suitability of Using a Linear Acoustic Propagation Model

This study simulated a histotripsy transducer designed for transcutaneous liver tumor ablation with dimensions closely matching those currently in clinical use [147]. The transducer was a large aperture, spherically curved 750-kHz phased array with a 14.2-cm focal radius. The ellipsoid aperture had maximum extents of 23.0 and 15.7 cm in the long and short transverse axes, respectively. The f-number along the long and short axes was 0.62 and 0.90, respectively. The array had 260 elements arranged in concentric rings around a 4-cm diameter circular cutout at the apex. Figure 2.1 gives a schematic of the array geometry. The array is controlled by a custom driver that permits individual transmit and receive on each element.

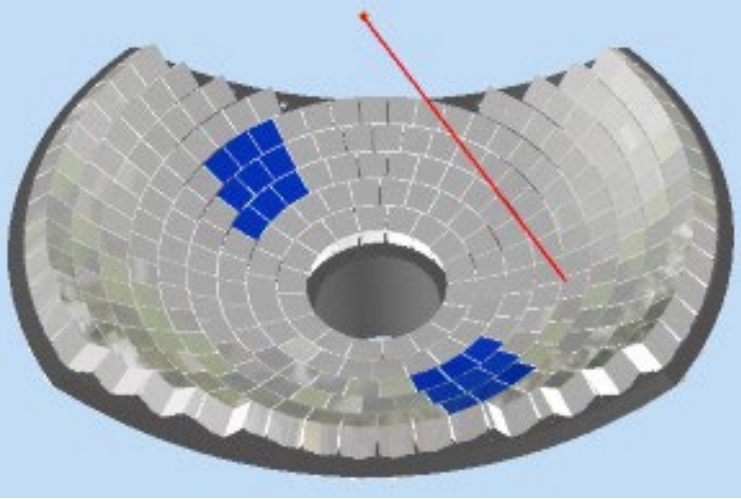


Figure 2. 1. CAD model of the histotripsy phased array considered in this study. Nonlinear acoustic output was measured from the entire array and from each of two 9-element clusters marked in blue. Measurements were acquired at 0, 2, and 5 mm from the geometric focus along the trajectory shown in red.

The suitability of using a linear acoustic propagation model for simulating histotripsy aberration effects was determined by assessing the effect of nonlinear acoustic propagation on arrival time. The array was placed in degassed, deionized water. A broadband fiber optic hydrophone (HFO-690, Onda Corporation, Sunnyvale, California, USA) was aligned orthogonally to the array axis. The hydrophone was connected to a 3-axis motor positioning system (Daedal,

Harrison City, PA) and an oscilloscope. A 4-cm thick section of excised porcine abdominal wall (skin, muscle, fat, connective tissue) was placed in the path, leaving a 2-cm gap between the tissue and the hydrophone. The effective focus was located by mechanically scanning the hydrophone until the peak-to-peak voltage of the oscilloscope signal was maximized.

Empirical measurements were acquired in two sets. The first set of measurements evaluated the degree of nonlinear waveform distortion as a function of distance from the focus. All array elements were driven simultaneously (in parallel) by a pulse with a single prominent negative cycle to generate a peak focal rarefactional pressure amplitude just below the cavitation threshold. The hydrophone was displaced by 0, 2, and 5 mm from the focus along a ray shown in red in Figure 2.1. (This trajectory was selected to bisect an acoustically active zone of the transducer along the lateral axis with lowest f-number, where the largest amplitudes along the wavefront (and thus strongest nonlinear effects) were expected to occur). At each location, 64 replicates of the resulting waveform were averaged and saved.

A second set of measurements investigated the effect of nonlinear propagation on arrival time to the focus. The hydrophone was placed at the measured focus. The pressure amplitude output from the array was incrementally increased from 6 to 14 MPa P-. Higher amplitudes were not possible because of spontaneous cavitation at the hydrophone. The waveform at each pressure amplitude was averaged and saved. Focal waveforms were also collected from each of 2 different 9-element clusters to evaluate the dependence of arrival time on nonlinearity at different aperture locations. Waveforms were measured from focused element clusters instead of unfocused individual elements to more closely approximate local contributions to the focused wavefront of the full aperture. The two clusters marked in blue in Figure 2.1 were

selected to represent opposing sides of the aperture (and thus different paths through the tissue sample). The amplitude generated by each cluster was incrementally increased from 0.4 to 1.8 MPa P- to compare arrival time at linear (low) amplitudes and at nonlinear (high) amplitudes. This amplitude range corresponds to a linearly estimated focal pressure of 7 MPa to 57 MPa P- (extrapolated by dividing the total number of array elements by 9 and multiplying by the amplitude from one cluster).

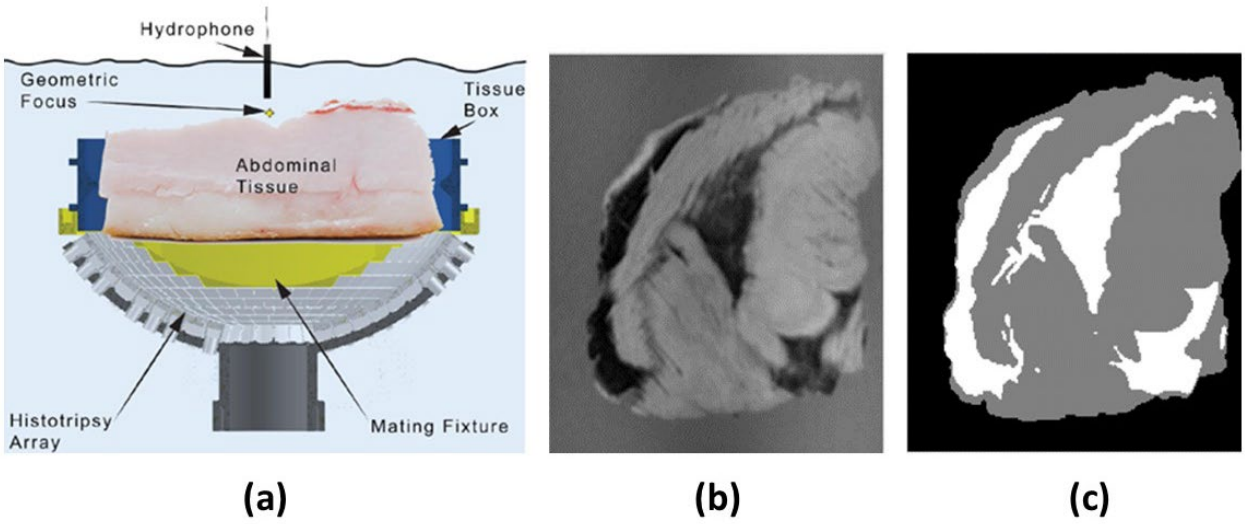


Figure 2. 2. (a) Half-section view of the experimental setup used to validate the segmented tissue acoustic propagation model. Porcine tissue embedded in gelatin was fixed within a bottomless stereotactic box with fiducial markers (dark blue). The box was rigidly and repeatably registered to the histotripsy array using a custom mating fixture (yellow). A waveform from each array element was recorded using a hydrophone at the array geometric focus. (b) MR image slice showing porcine tissue with fat suppression. (c) Image slice after segmentation. White denotes fat. Gray denotes muscle and other non-fat soft tissue. Black denotes water or gelatin.

2.2.2 Acoustic propagation modelling and validation

Once the suitability of using a linear acoustic propagation model to simulate histotripsy aberration was confirmed, a linear acoustic propagation simulation based on a segmented tissue model was used to predict arrival time differences through tissue. Simulations were

implemented with k-Wave, a MATLAB Toolbox for simulating acoustic wave fields in heterogeneous media with power law absorption of the form $\alpha = \alpha_0 \omega^y$, where α represents the depth and frequency-dependent attenuation, α_0 is the tissue-dependent attenuation coefficient, and ω is acoustic frequency [148]. In this study, the power law exponent y was set to 1.1 (because the power law implementation in k-Wave requires $y \neq 1$) [149]. The simulation space and time steps were 0.3 mm and 11.8 ns, respectively, to give a Courant Friedrichs Lewy number of 0.06 in soft tissue (1580 m s^{-1}) [150]. A preliminary study to optimize the space and time resolutions found that this combination of step values was sufficient to maintain propagation time errors from numerical dispersion below 100 ns. The simulation domain spanned 243 × 176.4 × 153.6 mm (810 × 588 × 540 grid points). All dimensions included a 4.8 mm artificial absorbing layer at the outer edges to prevent sound waves exiting the domain from reappearing due to periodic Fourier boundary conditions. The simulated time duration was 111.8 μs (9471 time steps). Simulations were accelerated by a distributed computing cluster. Each simulation was parallelized over 36 computing cores (Xeon Gold 6154 3.00 GHz, Intel, Santa Clara, California, USA) with 40 GB of collective memory. The average simulation execution time was 4 h.

Experimental validation of the segmented linear k-Wave simulations was performed using the setup in Figure 2.2 (a). A 4-cm thick sample of porcine abdominal wall tissue was embedded in 5% porcine skin gelatin (Sigma-Aldrich, Saint Louis, Minnesota, USA) that fixed its position within a custom 3D printed stereotactic box. The box was rigidly secured to the front of the transducer array in the acoustic propagation path with a mating fixture, ensuring repeatability. A hydrophone (Dynasen Inc, Goleta, California, USA) was placed at the geometric focus and

connected to a digital oscilloscope (PicoScope 5443D, Pico Technology, Cambridgeshire, UK). Waveforms were recorded from each array element pulsed individually at low (linear) pressure amplitude.

A simulation was set up to match the experiment by segmenting a magnetic resonance (MR) image of the stereotactic box containing the tissue. All MR images were acquired on a 3T GE MR750 scanner (GE Healthcare, Waukesha, WI) using 8-channel DuoFLEX 24 cm array coils (MR Instruments, Minneapolis, MN, USA). A liver acquisition with volume acceleration flex (LAVA-Flex) sequence incorporating a two-point Dixon method was used to produce water and fat images [151]. Scanning parameters were TE/TR = 1.9/4.5 ms, flip angle = 15 degrees, NEX = 3 and image resolution = 0.66 × 0.66 × 1 mm. The images were segmented to create a 3D mesh representing the acoustic properties of the propagation medium. Porcine fat, muscle (and other non-fat soft tissues), and the tank water (18.7˚C) were assigned sound speeds of 1460, 1550, and 1478 m s^{-1} and densities of 911, 1050, and 998 kg m^{-3}, respectively. The gelatin was assumed to have the same acoustic properties as water. Figures 2.2 (b) and (c) show a slice of the water-highlighting image before and after segmentation. The segmented image was registered to the array using fiducial markers on the stereotactic box. Acoustic propagation was simulated in reverse (from the target to the transducer) to reduce computational requirements. A point source at the geometric focus emitted a Gaussian pulse (750 kHz, 90% bandwidth). Each element had a point sensor at its center that recorded the acoustic pressure for the duration of the simulation. Arrival times of forward propagation (from the elements to the focus) were then deduced from the recorded signals using the principle of time reversal [152]. Use of the time reversal approach substantially reduced the number of simulations needed to estimate

the arrival times. A forward propagation approach would require 260 separate simulations of the same size and duration as the one described.

Relative arrival times to the geometric focus were determined for both sets of waveforms (experimental and simulated) from cross correlation between each waveform and a reference waveform. The lag that maximized the correlation value was converted to microseconds and used as the relative arrival delay. To enable comparison of the experiment and simulation, the median delay of each set was subtracted from all delays in the set. Simulated delays were considered sufficiently accurate if they deviated from the measured delays by <0.25 acoustic cycles. This benchmark limits the error between two simulated pulses to 0.5 cycles, where complete destructive interference occurs.

2.2.3 Evaluation of Aberration using Human Data

To evaluate the aberration effect in the human during histotripsy, acoustic maps of the human abdomen were constructed from CT scans of 10 deidentified adult subjects obtained from the Cancer Imaging Archive [153]–[157]. Subjects included 5 males and 5 females of varying body sizes. The CT images had a slice spacing of 1 mm and pixel size ranging from 0.68 × 0.68 mm to 0.94 x 0.94 mm. First, all images were interpolated to have the same spatial resolution as the simulation domain. Then, the images were segmented by first detecting the outer edge of the abdomen in each slice. Using the detected edge, the skin was assigned a fixed thickness (1.4 mm) [158]. All pixels outside the skin were labeled as water. Inside the skin, Hounsfield unit thresholds were applied to segment bone (>150 HU), cartilage (70 – 150 HU), non-fat soft tissue (-29 – +50 HU), fat (-190 – -30 HU), and air in the bowels and lungs (<-190 HU) [159]–[161]. Because costal cartilage has similar HU values to nearby liver, cartilage was

segmented by first applying a manually generated mask to spatially isolate the rib cage from the viscera and then applying the Hounsfield unit range for cartilage [162], [163]. Table 2.1 gives the acoustic property values assigned to each map component. The mass density of air was artificially increased to prevent instability of the simulation; however, the impedance mismatch and absorption were still sufficient to limit transmission to negligible amounts. Sound waves striking air were not expected to contribute constructively to the focus and were considered 'blocked'.

Table 2. 1. Acoustic properties of sound path components

Component	**Sound Speed** ($m\ s^{-1}$)	**Mass Density** ($kg\ m^{-3}$)	**Absorption Coefficient** ($dB\ MHz^{-1.1}\ cm^{-1}$)
Water* (20°C)	1483	998	0.0012
Skin	1620	1100	1.6
Fat	1430	916	0.4
Non-fat Soft Tissue	1580	1050	0.5
Bone	3520	1960	12
Cartilage†	1650	1100	5
Air (Bowel/Lung)‡	343	100	20

Acoustic properties were obtained from Duck [61] unless otherwise noted.
* Sound speed [164], density [165], and absorption [166]
† Sound speed [94]
‡ Density and absorption were artificially increased to maintain simulation stability while still minimizing effective transmission.

A set of k-Wave simulations was performed on the segmented human data to assess acoustic phase aberration that would be encountered for the histotripsy transducer described previously. The transducer was modelled as a single surface without element divisions to eliminate confounding effects of element size. The transducer was represented in the discrete domain by a cloud of 10000 points randomly sampling the aperture. The average spacing

between adjacent points was 0.57 wavelengths in water at the central frequency (750 kHz). The human abdomen maps were used to define a transcutaneous tissue path with the geometric focus in the liver. For each map, 3 scenarios were simulated. The scenarios represented different ‘extremes’ of plausible transducer angulations to assess how phase aberration varies with large changes in transducer angle. Figure 2.3 illustrates the position and orientation of the transducer relative to the abdomen in each scenario. All scenarios place the transducer in front of the abdomen. In scenario 1, the array axis was normal to the skin surface, and the array transverse dimensions were aligned with the left – right and cranial – caudal axes of the abdomen. Scenarios 2 and 3 were like scenario 1 but used different orientations. Scenario 2 rotated the transducer about its depth axis to avoid bowel when targeting a medial portion of the liver. Scenario 3 inclined the transducer to point more cranial and thus avoid lung when targeting a cranial portion of the liver. The 3 simulated scenarios represent practical angulations for targeting different parts of the liver. The straight-on orientation of scenario 1 permits targeting of deep regions. The axis rotation of scenario 2 helps avoid the bowel when targeting caudal portions of the liver. The cranial-caudal tilt reduces blockage by ribs and lung when targeting highly cranial portions of the liver.

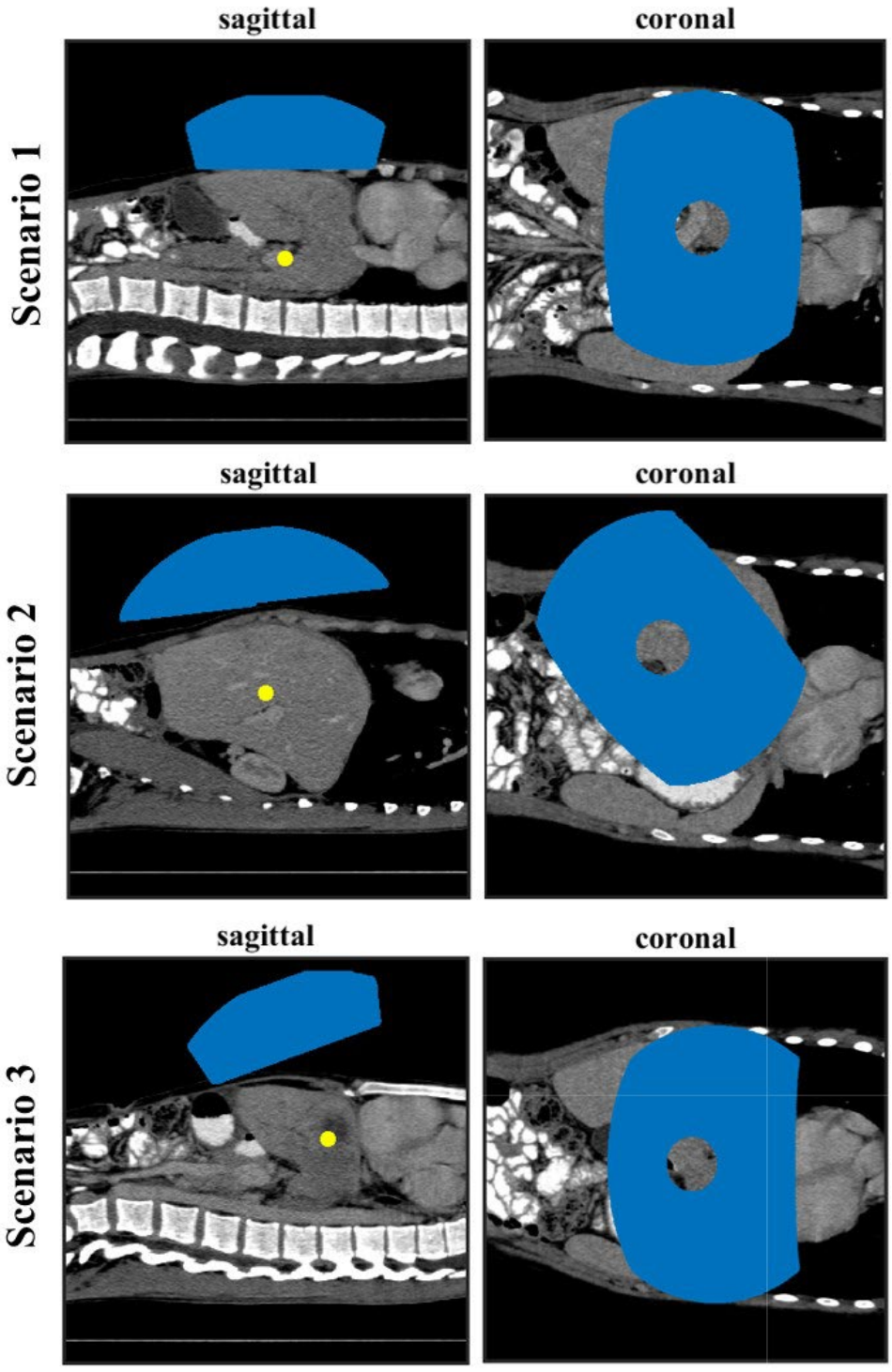


Figure 2. 3. Different transducer (blue) focusing scenarios shown relative to sagittal (left) and coronal (right) views of the abdomen. The yellow dot marks the target site. Scenario 1 focuses through the front of the abdomen with the transducer depth axis normal to the skin surface. Scenario 2 is like Scenario 1 but rotates the transducer around its depth axis (see coronal view). Scenario 3 is like Scenario 1 but tilts the cranial edge of the transducer up away from the skin and the caudal edge of the transducer down (see sagittal view).

For clarity, Figure 2.3 shows the abdomen in a fixed position while the transducer changes position. In practice, the transducer location was fixed in all simulations, while the abdomen maps were translated and rotated to recreate the focusing scenarios in Figure 2.3. As a result, the transducer axes (depth, long transverse, short transverse) were always aligned with the cardinal axes of the 3D simulation domain, which facilitated analysis of the 3D pressure field in the transducer transverse and depth planes. Table 2.2 summarizes by scenario the percentage of the aperture blocked by bone and air, the thickness of the tissue path, and the thickness of the fat in front of the target for all abdomen maps.

Table 2.2. Sound path statistics for different transabdominal focusing scenarios.

Scenario	Aperture Blocked (%)	Average Tissue Depth (cm)	Average Fat Thickness (cm)
1	24.3	10.0	1.6
2	19.8	8.7	1.7
3	23.6	9.0	1.8
All scenarios	21.4	9.0	1.7

Sound path variations over the aperture were calculated assuming a straight-line propagation trajectory. Given values are medians across subjects.

For each targeting scenario, 3 simulations were performed. The first simulation modelled reverse propagation by using the transducer points to receive signals from a point source placed at the geometric focus. Arrival times were determined from the received data using cross correlation with a reference kernel as described above. Relative delays were calculated by subtracting the median arrival time from each element's arrival time in the set.

The average magnitude of the relative delay over the transducer surface was quantified by computing the RMS value (hereafter termed RMS delay). The other two simulations modelled forward propagation and used the transducer points as sources. Maximum pressure amplitude was recorded over the entire sound field. In one of the forward simulations, all transducer points transmitted synchronously, thus modelling focusing without aberration correction. In the second forward simulation, transmission from each transducer point was delayed to exactly compensate the relative arrival time differences detected using the first (reverse propagation) simulation. This simulation modelled an ideal time-reversal based phase correction, where the transducer surface is composed of point elements with sub-wavelength spacing and the arrival delay for each element is known exactly. The focal pressure (the maximum pressure amplitude) and the focal shift (the displacement of the focus location from the target) were calculated from the simulated sound fields.

2.2.4 Investigating Sources of Aberration

The individual effects of specific sound path components on focusing quality degradation were investigated using 3 additional forward simulations for each targeting scenario. Instead of performing delay-based aberration correction, two of the simulations each separately changed the speed of sound of fat and the water bath to match non-fat soft tissue (1580 m s^{-1}). In a third simulation, the sound speed of the entire path was constant (1580 m s^{-1}). Absorption coefficients were left unchanged. Acoustic impedances were maintained by adjusting the mass density to compensate changes in sound speed. The simulated pressure field was used to calculate the focal pressure and shift obtained for each manipulation of the sound path. Change

in the focal pressure and shift was evaluated statistically by paired Student's t-tests of means across different manipulations.

2.3 Results

2.3.1 The Suitability of Using a Linear Acoustic Propagation Model

Nonlinear distortion of the measured pressure waveform decreased substantially at a short distance (<5 mm) from the array focus. Figure 2.4 gives waveforms and corresponding frequency spectra at 0, 2, and 5 mm from the focus. At the focus, the waveform was highly asymmetric. The positive phase had a sharp peak characteristic of a developing shockwave. The corresponding frequency spectrum had peaks above -20 dB at the harmonic frequencies of 1.5 and 2.25 MHz. At the pre-focal locations 2 and 5 mm, the waveform was markedly smoother and more symmetric. Also, spectral amplitude at the harmonic frequencies was negligible (≤20

dB relative to the amplitude at the central frequency).

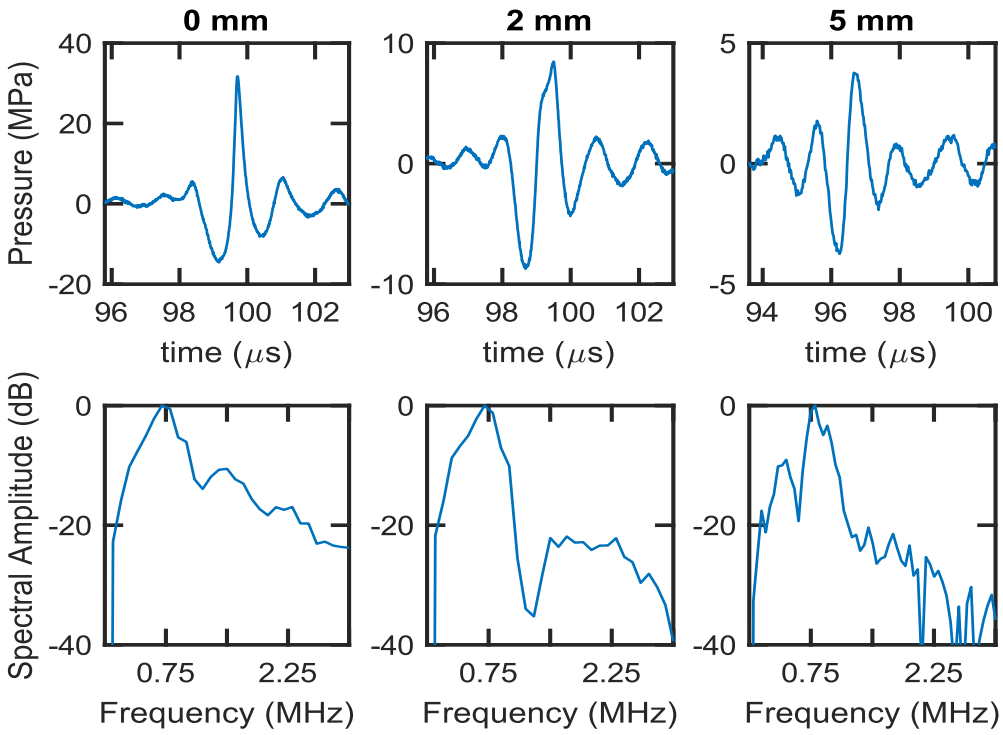


Figure 2. 4. Pressure waveforms (top) and log-compressed frequency spectra (bottom) acquired at different distances from the focus of the histotripsy transducer using constant source pressure close to the cavitation threshold. Frequency spectra are shown on a 40-decibel scale normalized to the peak amplitude at each distance.

Arrival time of the peak negative phase to the focus showed a small positive dependence on pressure amplitude. Figure 2.5 shows focal waveforms with varying amplitude generated by the full aperture and by two clusters of 9 array elements. For all waveforms, nonlinear distortion increased visibly with pressure amplitude. However, change in the arrival time of the peak negative pressure was limited. For the full aperture, the arrival time increased by <0.04 µs (~.03 cycles at the central frequency) between the lowest and highest amplitude. For the 9-element clusters, the maximum arrival time increase was <0.25 µs (~0.19 cycles at the central frequency).

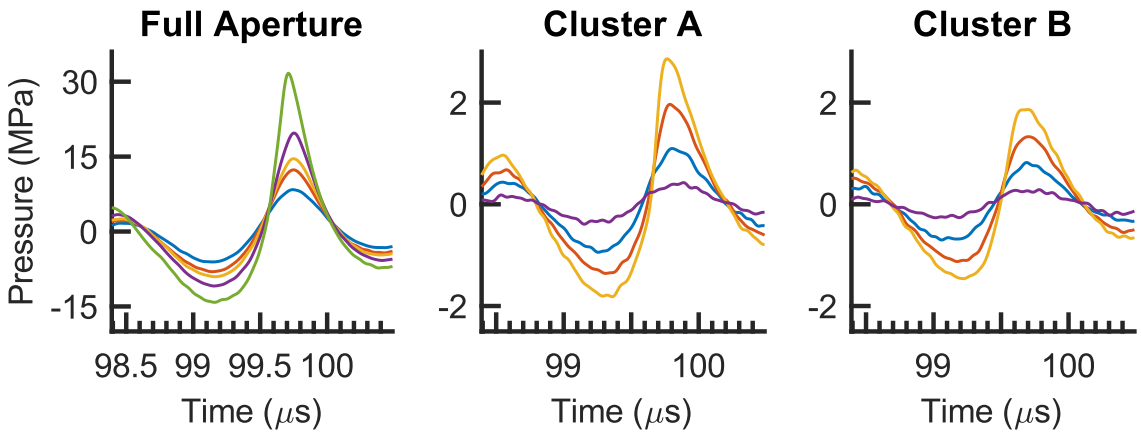


Figure 2. 5. Focal waveforms at varying pressure amplitudes (peak rarefactional pressure range: 6 to 14 MPa P_-) from the full transducer aperture and two clusters of 9 elements.

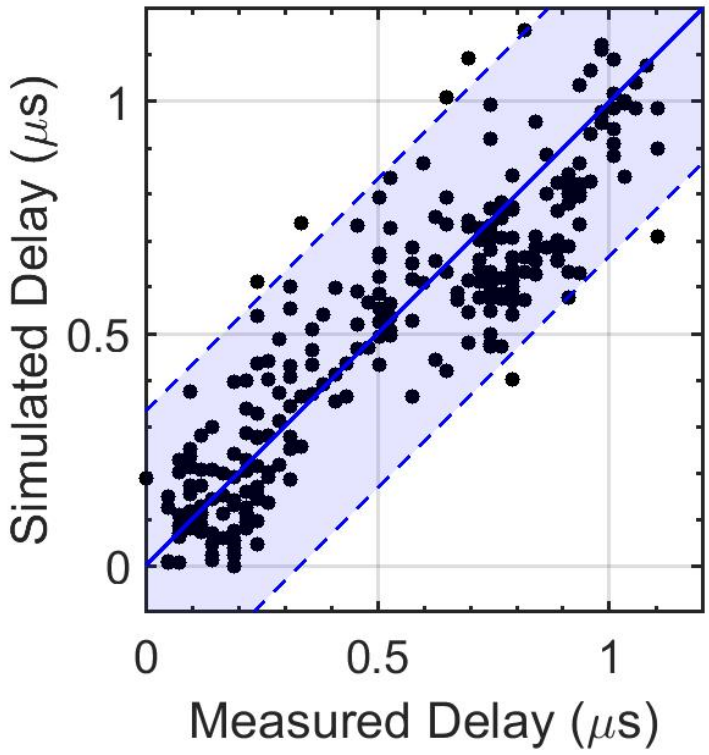


Figure 2. 6. Simulated versus measured arrival delays to the geometric focus through abdominal wall tissue. The solid blue line denotes an exact match. The shaded region bordered by two dashed lines denotes error less than one quarter of an acoustic cycle at the central frequency.

2.3.2 Acoustic Propagation Modelling and Validation

Arrival times simulated using the segmented tissue model matched well with measured arrival times. Figure 2.6 plots the simulated versus measured arrival time for the 260 array elements. The root-mean-square (RMS) prediction error was 0.14 µs, about one tenth of an acoustic cycle at the central frequency. 97% of elements had errors less than one quarter of a cycle.

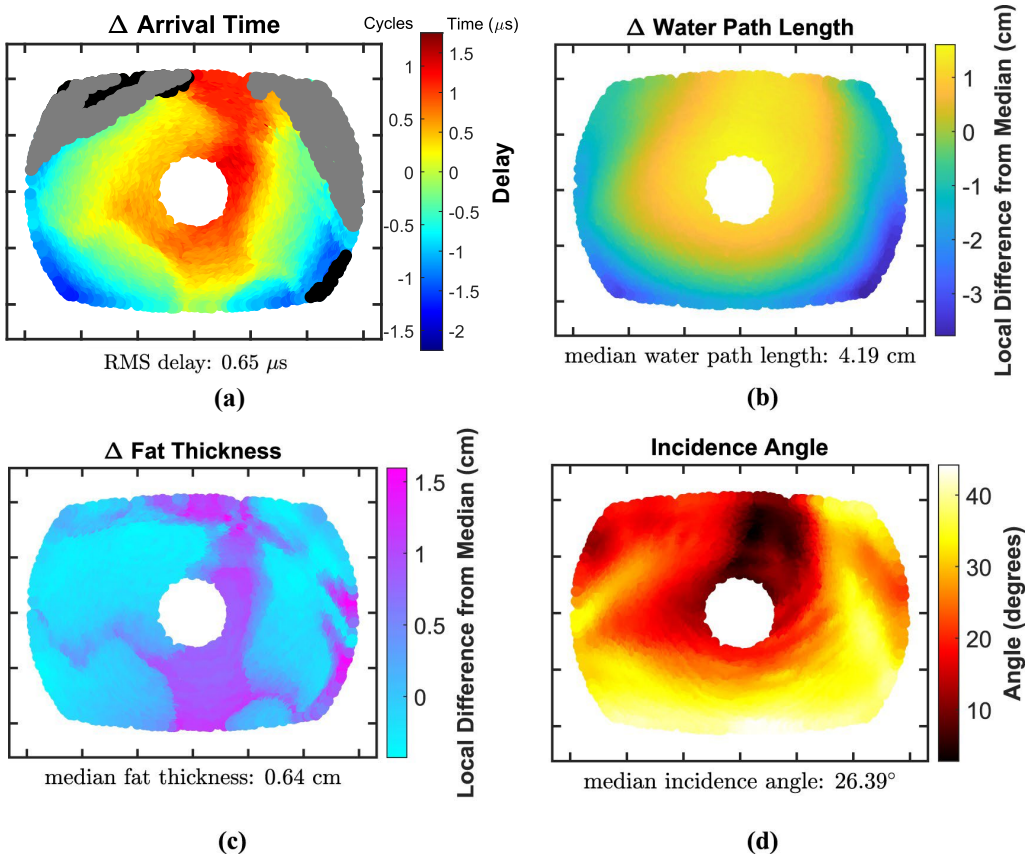


Figure 2. 7. In all panels, tick marks are spaced 4 cm apart. (a): Aperture map of arrival time differences in the liver of one subject for targeting scenario 3. Differences are mapped as positive and negative delays relative to the median arrival time to the target in units of microseconds and acoustic cycles. The root mean squared delay quantifies the average arrival time difference along the aperture. Portions of the aperture obstructed by air pockets or bone appear as black and gray regions, respectively. (b), (c): Maps of water path length (b) and fat thickness (c) fluctuations for the same targeting scenario. The mapped values represent the local difference from the median. (d): Map of incidence angle to skin surface.

2.3.3 Evaluation of Aberration using Human Data

2.3.3.1 Time of Arrival Variations at the Geometric Focus

Propagation through the human abdomen produced large arrival time differences across the simulated aperture. The aperture map in Figure 2.7 (a) shows color coded relative arrival times to the geometric focus for one representative subject. The delay between the earliest (blue) and latest (red) arriving pulses exceeded one cycle of the central frequency (1.3 μs). The average (RMS) arrival delay over the aperture was 0.65 μs, a phase shift of ~0.5 cycles. More than 60% of the aperture had phase shifts ≥0.25 cycles. The orientation of the transducer also influenced the delay pattern. Figure 2.7 shows an example of scenario 3. The transducer incline caused sound from the bottom edge to travel through mostly tissue and arrive early (relative to the top edge, which traveled through mostly water and arrived late). Fig. 2.7 (d) maps the angle of incidence to the skin surface of rays extending from the aperture to the geometric focus. Due to the transducer incline, the bottom edge had larger incidence angles (>45˚) than the top. Normal orientations (scenario 1), conversely, produced radially symmetric patterns without additional gradients. These orientation-specific patterns persisted across subjects.

Arrival time differences across the aperture were substantial for all subjects and targeting scenarios. For each given subject and scenario, the average magnitude of the arrival time difference across the aperture was quantified by the RMS delay. Further averaging over all subjects and scenarios (all 30 reverse simulations), the mean RMS delay was 0.65 μs with standard deviation 0.20 μs. The magnitude of the arrival time differences across the aperture varied by targeting scenario. For each targeting scenario, Table 2.3 gives the mean and standard deviation across all subjects of the RMS arrival delay, RMS fluctuation in water path length, RMS fluctuation in fat layer thickness, and median incidence angle over the aperture. Rotating

the transducer as in scenarios 2 and 3 created notably larger arrival time differences than orienting the transducer normal to the skin. This trend in average delay magnitude between oblique and normal transducer orientations paralleled similar trends in the average water path length fluctuation, fat thickness fluctuation, and incidence angle; on average, scenarios 2 and 3 had larger water path length fluctuations, fat thickness fluctuations, and incidence angles along the aperture than scenario 1.

Table 2.3: Sound path variation statistics for simulated histotripsy propagation through the human abdomen. Statistics include RMS arrival time difference, RMS water path length fluctuation, RMS fat thickness fluctuation, and median incidence angle across the aperture. Mean values (bold font) and standard deviations (in parentheses) summarize each statistic across all subjects and by targeting scenario.

Scenario	RMS Δ Arrival Time (μs)	RMS Δ Water Path Length (cm)	RMS Δ Fat Thickness (cm)	Median Incidence Angle (°)
1	**0.58** (0.12)	**1.1** (0.2)	**0.6** (0.2)	**26.7** (5.7)
2	**0.63** (0.25)	**1.3** (0.3)	**0.8** (0.3)	**27.**1 (5.0)
3	**0.73** (0.21)	**1.5** (0.3)	**0.8** (0.4)	**32.4** (4.0)
All	**0.65** (0.20)	**1.3** (0.3)	**0.7** (0.3)	**28.7** (5.5)

2.3.3.2 Effect of Aberration on Focusing Quality

Phase aberration by the human abdominal wall strongly distorted and lowered the amplitude of the pressure field. Figure 2.8 shows the log-compressed pressure field simulated using the same subject and targeting scenario as Figure 2.7. Transverse cross section images in Figure 2.8 (a) and (b) show the focus (the point of peak field pressure) without and with phase correction applied, respectively. The aberrated focus has a diffuse, irregular shape with extended side lobes. The amplitude of the secondary lobe (-7.4 dB) is close to that of the primary lobe (-6.2 dB). Contrastingly, the corrected focus forms a sharp ellipse with small (<-13 dB) side lobes. Correction increased the peak field pressure by 6.5 dB (+112%) relative to the aberrated focal

peak. In this example, the focus was not shifted from the target in the transverse dimensions. In other subjects and scenarios, aberration caused a small transverse focal shift (1.5 mm on average). Shift of the focus in the depth direction was highly pronounced for all subjects. Figure 2.8 (c) plots axial pressure field lines intercepting the focus both with (orange) and without (blue) aberration correction. The aberrated peak amplitude is shifted closer to the transducer by 9.0 mm, while the corrected peak occurs at the target depth. Aberration also broadened the focus in the depth direction.

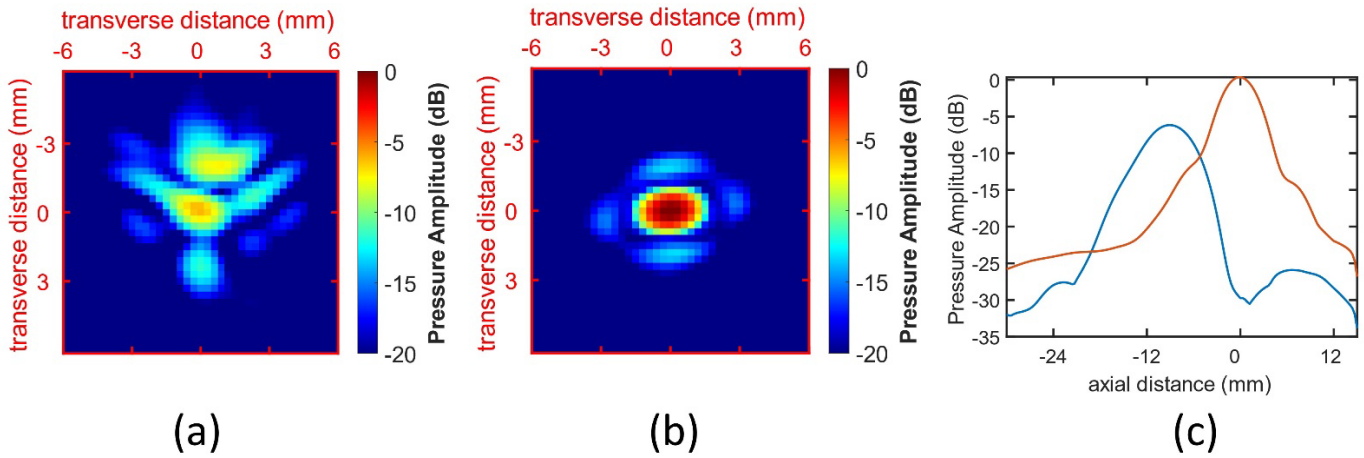


Figure 2. 8. (a), (b): Transverse cross section images showing the focus of the pressure field simulated in the liver without (a) and with (b) ideal phase correction. Pressure amplitude is shown on a 20 dB decibel scale normalized to the peak amplitude (0 dB) obtained in the corrected case. (c) One dimensional plots of the pressure along the depth direction, shown with (orange) and without (blue) aberration correction on a 35-decibel scale normalized to the peak amplitude (0 dB) obtained in the corrected case. The origin in all plots is the target location.

Phase correction recovered substantial pressure amplitude across all subjects. Table 2.4 gives the percent increase in pressure amplitude obtained using ideal phase correction (the increase relative to the peak uncorrected amplitude). The mean and standard deviation of the pressure increase are given by targeting scenario. Across all scenarios and subjects, the mean pressure increase was 95% with standard deviation 37%. 90% of the simulated corrections increased the peak aberrated pressure by

>50%. Also, in agreement with the arrival delays, scenarios 2 and 3 had larger pressure increases on average than scenario 1.

Targeting error due to phase aberration was substantial. The average focal shift was 6.8 mm (with standard deviation 2.8 mm). Most of the shift (93%, on average) was along the depth dimension and towards the transducer (pre-focal). Table 2.4 gives the depth-wise pre-focal shift before and after aberration correction by targeting scenario. The pre-focal shift was 6.4 mm on average. Scenario 1 had the largest average pre-focal shift of 7.2 mm. Ideal phase correction effectively returned the focus to the target within the simulation grid resolution limits for all cases.

Table 2.4. Focusing quality for simulated transmission through the human abdomen. Mean (bold font) and standard deviations (in parentheses) of the focal pressure amplitude increase from aberration correction and the pre-focal shift with and without aberration are reported for each targeting scenario and across all subjects.

Targeting Scenario	Pressure Amplitude Increase with PAC	Pre-Focal Shift (no PAC)	Pre-Focal Shift (with PAC)
1	**85%** (26)	**7.2 mm** (2.5)	**0.3 mm** (0.1)
2	**97%** (36)	**5.5 mm** (3.1)	**0.0 mm** (0.0)
3	**103%** (48)	**6.7 mm** (3.1)	**0.3 mm** (0.1)
All	**95%** (37)	**6.4 mm** (2.9)	**0.2 mm** (0.0)

2.3.4 Investigating Sources of Aberration

Figure 2.9 (a) illustrates how modifying the sound speed of different media affected the pressure amplitude. Changing the sound speed of fat to match that of non-fat soft tissue (1580 m s^{-1}) increased the peak pressure amplitude by 4.3 dB on average. This increase approached that achieved by using ideal phase correction (5.6 dB) or by setting all sound speeds to be constant (5.8 dB). Conversely, modifying the sound speed of water did not appreciably alter the peak pressure.

The water path strongly affected the pre-focal shift. Figure 2.9 (b) compares the pre-focal shift obtained by modifying the sound speed of different media to the pre-focal shift obtained without

modification or phase correction. Matching the sound speed of water to soft tissue reduced the focal shift to an average of 1.9 mm, which approached the diffraction and attenuation limited shift of 1.2 mm achieved when the entire medium sound speed is constant. Modifying the fat had no appreciable effect on the focal shift.

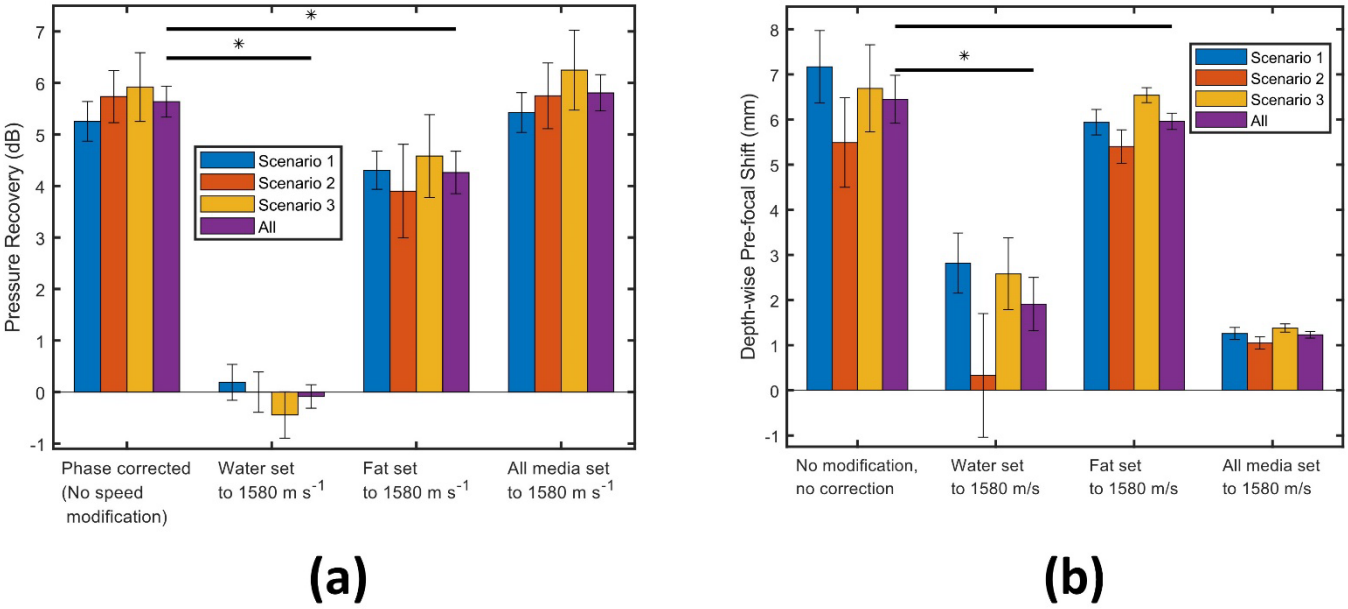


Figure 2. 9. Focal pressure amplitude increase (a) and pre-focal shift (b) obtained by changing the sound speed of specific media to match that of non-fat soft tissue (1580 m s^{-1}). Focal pressure increases and pre-focal shifts are averages (means) by targeting scenario. Error bars indicate the standard error associated with each mean. Horizontal bars with asterisks denote statistical significance as determined by Student's t-test for pairs of means using data from all subjects and scenarios (*n*=30). The absence of an asterisk indicates that the relationship was not statistically significant.

2.4 Discussion

Simulation has been used extensively to study phase aberration of therapeutic ultrasound in the breast, abdomen, and pelvis [20], [23], [27], [28], [92], [145]. Simulation permits study of intact human tissues in their natural conformation and thus has some advantages over in vitro study. However, to be useful, the simulation must properly represent the physical relationships that govern aberration and its effects. One potential concern here is that, due to the large

pressures employed by histotripsy, sound propagation can become very nonlinear, especially near the focus [167]. Despite this strong nonlinear effect, the suitability of the linear model for investigating histotripsy phase aberration is suggested by two observations. First, the strong focal gain of low f-number histotripsy transducers limits most nonlinear distortion to a small region around the focus [66]. As shown by Figure 2.4, this transition occurs very close to the focus (<5 mm). Therefore, linear effects govern wave propagation speed along most of the path. Second, the peak rarefactional pressure phase maintains a nearly constant arrival time, shape, and width despite strong nonlinear effects in the focal region (see Figure 2.5). The linear model is thus unlikely to strongly alter predictions of the rarefactional pressure focus and gives a sufficient model of histotripsy phase aberration. A comparison of the waveforms from clusters A and B in Figure 2.5 suggests that nonlinear distortion slightly increases arrival time differences across elements. A likely result of this effect is that the linear model will moderately underestimate histotripsy phase aberration in the human abdomen.

The simulations used here predict arrival time through abdominal soft tissues with reasonable accuracy. As illustrated by Figure 2.6, simulated arrival delays agreed well with measurements in porcine abdominal wall (average error, ~0.10 acoustic cycles at the central frequency). Almost all errors were <0.25 cycles, where time difference would begin to destructively interfere. Most error likely resulted from MR image segmentation inaccuracies that misrepresented the size and shape of fat inclusions in the tissue sample. These small, distributed segmentation inaccuracies added random error to the arrival time estimates. Another potential source of error is numerical dispersion [168]. Error from numerical dispersion was reduced by using small space and time steps in the simulations but was not eliminated.

Preliminary simulations with the selected step parameters showed that dispersion errors were small (<30 ns) on average but could occasionally reach ~100 ns (~0.075 acoustic cycles). Additionally, slight mis-registration of the image or sound speed misestimation could have added a small systematic error. It should be noted that the experimental validation used MR images for the segmented model, while the simulations of human tissue used CT images. CT has lower soft tissue contrast, which could cause segmentation errors at the boundaries between soft tissues and sensitivity to the intensity thresholds used for segmentation. However, small additional segmentation errors are unlikely to substantially alter the simulation results. The speed of sound differs by 0.14 mm/μs between fat and other soft tissue. To produce an arrival time error of >0.25 cycles, the segmentation error must exceed 4.7 mm. Because soft tissue sound speed differences are moderate, large arrival time differences require large-scale tissue path differences (e.g., from spatial variations in the thickness of fat) to accrue.

The validated simulations indicate that human abdominal soft tissue severely aberrates acoustic fields from large aperture, low f-number histotripsy transducers. Arrival time differences at the geometric focus are large (~0.5 cycles at the central frequency, on average) and thus compromise constructive interference at the target. The resulting degradation of focus quality and amplitude has strong implications for transabdominal histotripsy. Notably, phase correction can theoretically recover substantial pressure amplitude. The phase corrections simulated here increased pressure amplitude by 95%, on average. This increase very likely exceeds the improvement obtainable in actual clinical practice because the phase corrections were calculated with the same tissue configuration as in the forward simulations from an ideal point source and applied using point elements with sub-wavelength spacings.

However, as shown in Figure 2.7, the arrival time variations are smoothly varying with relatively low spatial frequencies. Therefore, signal-based correction with finite-sized elements of practical dimensions could likely recover substantial amplitudes. Increased focal pressure amplitude could improve histotripsy treatment efficacy and efficiency, as well as expand the treatment range to include challenging targets where acoustic access (and thus pressure amplitude) is limited.

Histotripsy transducer geometry increases phase aberration by creating large-scale tissue path variations. The large, tightly curved aperture requires coupling to the skin via a bath or water-filled cushion. Over the large aperture, the ratio of path distance through water and tissue can vary extensively, increasing propagation time variance (see Figs. 2.7 (a) and (b)). Additionally, the strong curvature creates large angles of incidence to the skin surface (see Fig. 2.7 (d)). As a result, sound waves refract at tissue boundaries, further varying their path (and thus propagation time) through tissue. Furthermore, the large aperture focuses sound through a wide extent of the abdomen. As illustrated in Figure 2.7 (b), the thickness of irregularly distributed tissues like fat can vary substantially over this large extent. These spatial fluctuations in fat layer thickness further increase the heterogeneity of the tissue path and, hence, propagation time variance. By amplifying macroscopic differences in the tissue path (like water path length and fat thickness variation), histotripsy transducer geometry produces a severe aberration effect in soft tissues despite low therapeutic frequencies.

Although water path length and fat thickness variation both contribute to phase aberration, their effects on focus distortion are distinctly different. Figure 2.9 shows that the water path negligibly affects the focal pressure amplitude but strongly affects the focal shift. These

contrasting outcomes likely result from the geometric mismatch between the strongly curved transducer and the flatter skin surface. Propagation distances from a spherically curved source to an approximately planar surface have spatial symmetry. Symmetry in the resulting phase errors shifts the focus without strongly affecting pressure amplitude, permitting constructive interference of the sound waves at an off-target location. For example, the radially symmetric arrival time pattern shown in Figure 2.7 (a) constrains focusing errors to the axial (depth) dimension. Because the sound waves are spherical, axial phase error is compensated by changing the time and depth at which the focus occurs. Here, outer waves propagate faster than inner waves. Thus, trailing portions of the outer spherical waves intersect leading portions of inner spherical waves to interfere with maximal coherence. The resulting focus has minimal pressure loss but is shifted towards the transducer. Conversely, the fat layer negligibly affects the focal shift but strongly affects the focal pressure. The irregularly shaped fat layer produces anisotropic path differences that do not favor any single direction. This asymmetry prevents focal shift but causes destructive interference that strongly decreases the focal pressure amplitude. Hence, the two main sources of large-scale soft tissue heterogeneity distinctly affect focusing quality. Gross layer divisions (such as water to tissue) govern the focal shift, while irregular layer morphologies (as in abdominal fat) dominate pressure loss.

Due to these geometrical factors, abdominal aberration depends on the orientation of the transducer. Aligning the axes of the transducer with those of the body (left-to-right, head-to-foot, belly-to-back) as in scenario 1 creates a strongly axisymmetric delay pattern and thus a large axial shift. Deviating from this alignment, as in scenarios 2 and 3, creates asymmetric path differences and incidence angles that strongly decrease focal pressure. Thus, transducer

orientation can have consequences for focusing quality. Normal orientations (like scenario 1) can increase targeting depth error, while oblique orientations that avoid rib blockage can increase aberration-mediated pressure loss.

One important limitation between the simulations in this study and histotripsy in vivo is the absence of a true water bath or coupling cushion, which typically flattens the abdomen. The CT images used for the simulations represent the abdomen without the compression of water coupling. Therefore, the simulated abdomens are significantly more curved than during a true procedure. This study shows that aberration severity depends strongly on geometry, and specifically, that flatter interfaces should increase aberration effects. Therefore, a potential result of simulating a round abdominal shape is that the simulations here underestimate aberration in transabdominal histotripsy.

The findings of this study imply that large-scale tissue features, including gross layer divisions (e.g., water to tissue) and irregular tissue boundaries (e.g., fat), govern transabdominal histotripsy aberration. This conclusion contradicts ultrasound imaging studies of abdominal aberration, which show that small-scale internal tissue structures dominate focal distortion effects [6]. The difference in aberration between histotripsy and ultrasound imaging arises from the different frequencies and transducer geometries used. High imaging frequencies are sensitive to small-scale intra-tissue inhomogeneities, while lower therapeutic frequencies are not. Along small, flat imaging apertures, thickness variations and incidence angles are moderate; however, along large, curved histotripsy apertures, the effects of path differences and refraction can be extreme. Thus, the mechanism of aberration in histotripsy differs from ultrasound imaging, but the resulting focal distortion is nonetheless substantial.

The findings also have implications for aberration correction of transabdominal histotripsy treatments. The results suggest that correcting aberration from the water path can substantially reduce targeting error. One simple correction approach is substitution of the water bolus with a coupling fluid 'matched' to the average sound speed in soft tissue. This approach would require minimal modification to the existing clinical system. However, the study results also show that water path correction alone cannot recover substantial pressure amplitude, which depends strongly on aberration from heterogeneous tissue paths. Recovery of pressure amplitude for transabdominal histotripsy treatments will therefore require a transition from the monolithic transducer currently in clinical use to a phased array design. Pressure amplitude recovery will be especially critical for the successful ablation of deep-seated or highly obstructed liver tumors, which are currently not treated with histotripsy in the clinic. Transabdominal histotripsy presents unique challenges to phase aberration correction. Namely, abdominal soft tissues and organs readily shift and deform, thereby complicating PAC techniques that rely on registration of a tissue model derived from pre-operative images with the intra-operative configuration of the tissue and transducer, as used in therapeutic ultrasound of the brain and breast [26], [80], [82], [141]. In addition to sensitivity to registration, such propagation modeling-based approaches can be highly computationally intensive. Full-wave propagation models like k-Wave can entail unacceptably long compute times for clinical implementation [77], [78]. Alternative, computationally efficient propagation models have been proposed but are still sensitive to inaccurate tissue acoustic property estimations and mis-registration of the image [81], [169]–[171].

The present findings suggest that for transabdominal histotripsy, the focal shift depends strongly on water path aberration, while pressure amplitude depends strongly on soft tissue heterogeneity. This relative independence between targeting accuracy and focal gain in transabdominal histotripsy may permit an alternative two-part PAC approach which combines a preliminary water path correction to reduce focal shift with a subsequent ultrasound signal-based correction to recover pressure amplitude and focal gain at the corrected location. The preliminary water path correction could employ a direct substitution method (as described above) or could use a receive-capable histotripsy phased array to map the water path length (as in Fig. 2.7b) from pulse-echo measurements off the skin surface and estimate propagation times with a rapid, two-layer ray tracing algorithm. Water path correction using either method could reduce a substantial portion of the targeting error without materially extending procedure times. For the second part, a receive-capable phased array could acquire signals from ultrasound backscatter [103] or emissions from acoustic cavitation [63] to estimate and compensate propagation differences at the corrected focus location. Such signal-based PAC methods can recover substantial pressure amplitude but cannot correct focal shift. Employed together, water path correction followed by signal-based PAC could improve both targeting accuracy and focal pressure amplitude for transabdominal histotripsy without tissue-model registration and within clinically acceptable execution times.

2.5 Conclusion

A suitable computational model for histotripsy phase aberration was identified and experimentally validated for a large aperture, low f-number histotripsy transducer focusing

through abdominal soft tissue. Simulations using human data showed that transabdominal phase aberration of large, strongly curved histotripsy transducers is severe despite low therapeutic frequencies. Phase aberration correction could potentially recover substantial pressure amplitude, increase focal gain, and correct focal shifts to improve transabdominal histotripsy treatments.

Unlike in transabdominal ultrasound imaging, large-scale tissue path differences strongly affect phase aberration in transabdominal histotripsy. The reason for this difference is transducer geometry. The large histotripsy transducer aperture causes the propagation distance through different tissue layers to vary extensively. Large angles of incidence from the strong curvature further distort the histotripsy beam. Thus, although histotripsy uses lower frequencies than ultrasound imaging, the transabdominal aberration effect is nonetheless substantial.

Geometrical factors also cause different components of the transabdominal sound path to have distinct effects on focal distortion from aberration. The water path creates symmetry in the resulting phase distribution that effectively “steers” the wavefront, shifting the focus without substantially decreasing the maximum pressure amplitude. Conversely, tissues with irregular boundaries (like fat) create asymmetry in the phase distribution, resulting in strong focal pressure loss.

Chapter 3
Effect of Aberration Correction on the Treatment Envelope for Transabdominal Histotripsy in the Human Liver

In the previous chapter, a histotripsy transducer was simulated focusing at a small number of locations in the human liver. Those simulations therefore cannot inform on how focusing quality varies as a function of space, which is necessary to quantify the treatment envelope. This chapter simulates transabdominal focusing over the entire liver to map the spatial variation in focal pressure amplitude both with and without aberration correction. The results suggest that aberration correction can substantially expand the treatment envelope for transabdominal histotripsy in the liver.

3.1 Introduction

The number of patients who can receive histotripsy treatment is currently limited. To date, clinical trials have only included patients with tumors in relatively shallow, acoustically accessible locations below the ribs where the histotripsy transducer can produce a large pressure amplitude and thereby generate a large and dense bubble cloud for therapy [172]. At deeper, more cranial locations, focal pressure amplitude is strongly attenuated by acoustic obstructions (i.e., ribs and lung), acoustic absorption, and phase aberration. If severe, this attenuation can impede bubble cloud formation, thus preventing histotripsy treatment altogether. In other cases, attenuation can be overcome by increasing acoustic power input from the transducer. However, these targets are often located behind ribs, which strongly absorb the incident sound, heating surrounding tissues at a rate that increases with the incident acoustic intensity [98], [173]. This effect, along with decreased focal pressure amplitude, can hinder the safety and efficacy of histotripsy in these regions and thus limits the treatment envelope (range of locations in the liver where histotripsy treatment is feasible).

Acoustic obstruction and absorption cannot be avoided. However, phase aberration can be corrected to substantially improve focusing gain through the abdomen, as shown in Chapter 2. Aberration correction could potentially restore sufficient focal pressure amplitude to enable bubble cloud generation at locations where treatment would otherwise be prevented. Also, by improving the focal gain, aberration correction could decrease the input power required to perform therapy, thus reducing the risk of heating for targets obstructed by ribs. Therefore, aberration correction could potentially expand the treatment envelope of transabdominal histotripsy in the human liver, thereby enabling the treatment of more patients.

The objectives of this study were (1) to quantify the treatment envelope for histotripsy of the human liver and (2) assess the effect of aberration correction on the treatment envelope. Our approach was to systematically map the focal pressure in the liver both with and without aberration correction using the validated computational model from Chapter 2 with anatomical data from 10 adult subjects of varying body size. For clinical relevance, we simulate a histotripsy transducer with similar dimensions to the current clinical device segmented into a phased array with practical-size elements. The results of the study indicate that aberration correction could substantially expand the treatment envelope of transabdominal histotripsy in the liver to enable treatment of a broader patient population.

3.2 Methods

3.2.1 Human abdominal models

The acoustic path through the human abdomen was modelled using 3-D CT scans of 10 de-identified adult subjects obtained from an open access medical imaging repository [153]–[157]. The subjects included 5 males and 5 females. The body mass index (BMI) of each subject was estimated from the CT images by converting voxels to weight in kilograms assuming a tissue mass density of 1050 kg m^{-3} and dividing by the height in meters squared. The average estimated BMI was 27.8 with range 17.1 to 36.6. The CT images were segmented into air (lung, bowel), bone, cartilage, skin, fat, and other soft tissue using Hounsfield unit thresholds as described in section 2.2.3. The liver was segmented manually and then sub-divided into 30 equal sub-volumes (average over subjects: 75 cm^3, range: 40 – 125 cm^3). The center of mass of each volume was set as a target for focusing. To aid clinical reference, the liver of each subject

was also manually divided into Couinaud segments, a set of 8 anatomical regions often used to describe liver tumor location [174]. An illustration of the Couinaud segments is given in Figure 3.1. The average number of focusing targets per segment and average segment volumes are given in Table 3.1.

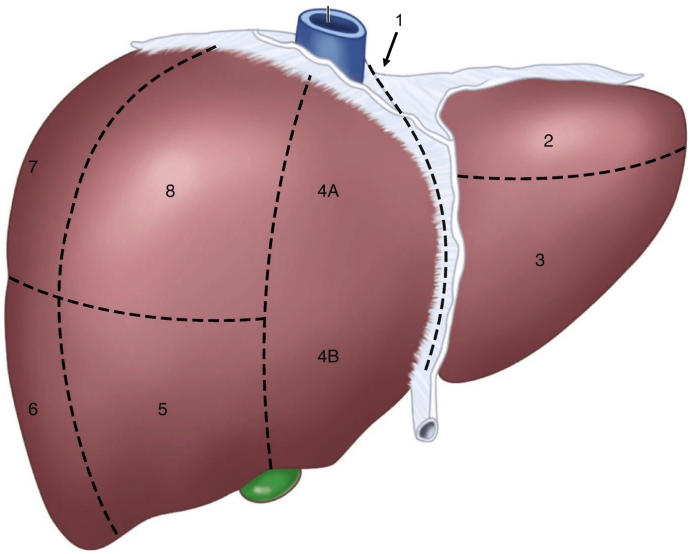


Figure 3. 1. Couinaud segments of the liver. Image adapted from Sellers [175].

Table 3. 1. Couinaud segments

Segment	Average volume (cm^3)	Average number of targets	Average blocked aperture
I	60	1	47%
II	325	4	21%
III	154	2	28%
IV	502	6	34%
V	349	5	21%
VI	157	2	30%
VII	328	4	52%
VIII	388	5	51%

3.2.2 Optimization of Transducer Orientation

This study considered a transducer with similar dimensions to the current clinical device. The transducer had a truncated spherical aperture with maximum lateral extents of 23 and 15.7 cm, a 13.8-cm focal radius, and a 6-cm circular cutout at the apex. The central frequency f_c was 750 kHz. To simulate a phased array, the transducer aperture was sub-divided into 256 equal-area elements with irregular polygon shapes and a pseudo-random arrangement following the method described by Rosnitskiy et al [176]. The transducer geometry is shown in Figure 3.2.

For a given focusing target, the amount of obstruction in the acoustic path depends on the orientation of the transducer with respect to the body. For example, obstruction by ribs can be reduced when targeting subcostal portions of the liver by tilting the transducer along the cranial – caudal axis towards the feet. Thus, for each focusing target, obstruction was minimized by finding the transducer orientation that maximized the free (unblocked) area of the transducer aperture. First, rays were traced in discrete CT image space from the target to a spherical surface of radius equal to the focal length, which defines the possible range of rotations for the transducer. The maximum distance between rays on the surface was 1.3 mm ($0.65\lambda_c$, where λ_c is the wavelength in water at 750 kHz). Rays that intersected CT pixels with air or rib were marked as 'blocked.' Initially, the long lateral axis, short lateral axis, and depth axis of the transducer were aligned with the x, y and z axes of the CT image, which run left-to-right, cranial-to-caudal, and ventral-to-dorsal along the body, respectively. From this initial position, the transducer geometry was rotated about the x, y, and z axes at angles θ, φ, and γ, which were varied in 5° increments over ranges of -70° to 70°, -70° to 70°, and -45° to 45°, respectively. Transducer rotations were numerically simulated by rotating the x, y, and z axis unit vectors $\vec{\boldsymbol{\imath}}$, $\vec{\boldsymbol{\jmath}}$, and $\vec{\boldsymbol{k}}$ by each combination of angles θ, φ, and γ using

$$\vec{\boldsymbol{\imath}}_{\boldsymbol{rot}} = \cos\varphi\cos\gamma\,\vec{\boldsymbol{\imath}} + \sin\gamma\,\vec{\boldsymbol{\jmath}} - \sin\varphi\cos\gamma\vec{\boldsymbol{k}}$$

$$\vec{\boldsymbol{\jmath}}_{\boldsymbol{rot}} = -\sin\gamma\,\vec{\boldsymbol{\imath}} + \cos\theta\cos\gamma\,\vec{\boldsymbol{\jmath}} + \sin\theta\cos\gamma\vec{\boldsymbol{k}}$$

$$\vec{\boldsymbol{k}}_{\boldsymbol{rot}} = \sin\varphi\,\vec{\boldsymbol{\imath}} - \sin\theta\cos\varphi\,\vec{\boldsymbol{\jmath}} + \cos\theta\cos\varphi\vec{\boldsymbol{k}}$$

where $\vec{\boldsymbol{\imath}}_{\boldsymbol{rot}}$, $\vec{\boldsymbol{\jmath}}_{\boldsymbol{rot}}$, and $\vec{\boldsymbol{k}}_{\boldsymbol{rot}}$ are the axis unit vectors of the rotated reference frame. Then, the coordinates x_r, y_r, and z_r of each ray $\vec{r}$ were projected onto the rotated reference frame using

$$x_{r,\mathrm{proj}} = \vec{\boldsymbol{\imath}}_{\boldsymbol{rot}} \cdot \vec{r}$$

$$y_{r,\mathrm{proj}} = \vec{\boldsymbol{\jmath}}_{\boldsymbol{rot}} \cdot \vec{r}$$

$$z_{r,\mathrm{proj}} = \vec{\boldsymbol{k}}_{\boldsymbol{rot}} \cdot \vec{r}$$

where $\cdot$ is the dot product, and $x_{r,\mathrm{proj}}$, $y_{r,\mathrm{proj}}$, and $z_{r,\mathrm{proj}}$ are the coordinates of the ray $\vec{r}$ in the rotated reference frame. All projected rays lying within the bounds of the transducer aperture were then counted as blocked or unblocked to calculate the total blocked aperture area for each combination of angles. Orientations that placed the transducer within the body were discarded. After all angle combinations were tested, the orientation with least blocked aperture was selected for the given focusing target. The average percent blocked aperture after optimization is given by Couinaud segment in Table 3.1.

For some targets in the liver located deep below the skin, the transducer could not be placed without intersecting the body. A practical solution in this case would be to place the transducer at a radial distance greater than the focal length away from the target and then electronically steer the acoustic focus by appropriately time delaying elements. However, at the time of this writing, these scenarios have not been successfully simulated and were thus excluded from the current study (an average of 4 targets per subject, with range 0 to 8). This issue is discussed in Section 3.4.

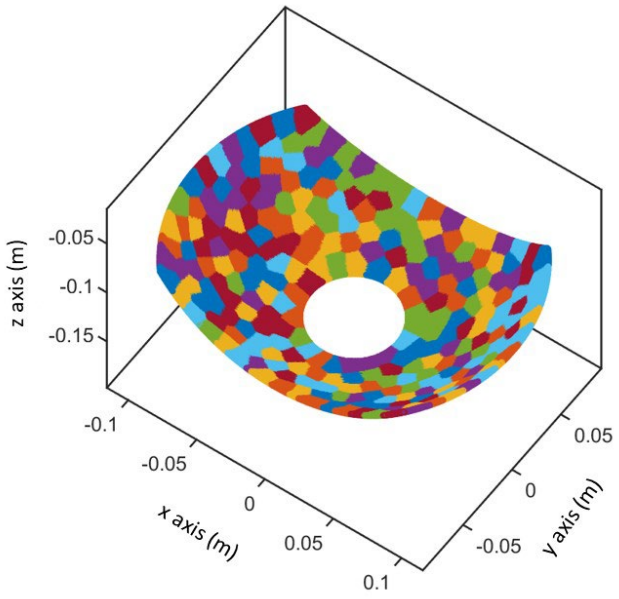


Figure 3. 2. Schematic of the simulated histotripsy transducer with 256 equal-area polygon shaped elements.

3.2.3 Acoustic Propagation Simulations

Once the transducer orientation was optimized for each target, acoustic propagation was simulated to assess focusing quality with and without aberration correction. Acoustic propagation was simulated in the linear regime. The suitability of the linear model for simulating aberration correction in histotripsy is discussed in Chapter 2. Simulations were performed with k-Wave, a MATLAB Toolbox that numerically solves the wave equation for arbitrarily shaped acoustic sources in heterogeneous media with power law absorption of the form $\alpha = \alpha_0 \omega^y$, where α represents the depth and frequency-dependent attenuation, α_0 is the tissue dependent attenuation coefficient, ω is acoustic frequency, and y is the power law exponent [148]. For speed, k-Wave solves the wave equation in the spatial frequency domain or k-space, which permits numerically efficient approximations of the spatial and temporal derivatives [168]. The space and time steps in all simulations were 0.3 mm and 11 ns,

respectively. The simulation domain spanned 243 × 176.4 × 162 mm (810 × 588 × 540 grid points), which included a 2.4-mm perfectly matched layer (PML) around the edges to prevent sound waves exiting the domain from re-entering due to periodic Fourier boundary conditions. The simulated time duration was 110 μs (10000 time steps). Simulations were accelerated by a distributed computing cluster. Each simulation was parallelized over 30 computing cores (Xeon Gold 6154 3.00 GHz, Intel, Santa Clara, California, USA) with 60 GB of collective memory. The average simulation execution time was 4 h.

To represent the curved aperture transducer from Section 3.2.2 in the k-Wave simulations, two problems had to be addressed. One problem was that the finite-sized aperture has infinite bandwidth in the spatial frequency domain, while k-Wave represents k-space with a finite set of spatial frequencies [177]. Representation of an infinite bandwidth surface in band-limited k-space can distort the simulated acoustic field [178]. The other problem was that a curved surface intersects few points in discrete Cartesian space. Interpolation of curved surfaces to the discrete grid can cause staircasing errors and uneven spatial sampling [179], [180]. Therefore, the transducer was modelled using the kWaveArray object class from the k-Wave Toolbox, which returns samples of a spatially band-limited version of each element with appropriate scaling to compensate for variations in the sampling density [178].

In all simulations, the transducer axes were aligned with the orthogonal axes of the domain. The segmented CT images were rotated and interpolated to place the target at the geometric center of the simulated transducer in the optimal orientation from Section 3.2.2. The voxels representing the abdomen were assigned acoustic properties given in Table 3.2. All voxels outside the body were assigned the acoustic properties of water. In k-Wave simulations, large

impedance differences (like between air and bone) can cause numerical errors and instability. The goal of this study was not to accurately model sound propagation in air or bone but to model air and bone as acoustic obstructions (i.e., as strong attenuators). Therefore, to decrease the difference in impedance, bone and air were both assigned the same acoustic properties of sound speed c = 900 m s^{-1}, density ρ = 100 kg m^{-3}, and α_0 = 15 dB MHz^{-2} cm^{-1}, which were selected to simulate strong reflection and attenuation while limiting numerical errors. In all simulations, the power law exponent y was set to 2, which limits errors from dispersion without significantly altering absorption at sub-MHz frequencies [149].

Table 3. 2. Acoustic properties of sound path components

Component	**Sound Speed** (m s^{-1})	**Mass Density** (kg m^{-3})	**Absorption Coefficient** (dB MHz^{-2} cm^{-1})
Water* (20°C)	1483	998	0.0012
Skin	1620	1100	1.6
Fat	1430	916	0.4
Non-fat Soft Tissue	1580	1050	0.5
Cartilage†	1650	1100	5
Acoustic obstruction (Bone/Bowel/Lung)‡	900	100	15

All properties were from reference [61] unless otherwise noted.
*Sound speed [164], density [165], and absorption [166]
† Sound speed [94]
‡ Density and absorption were set to nonphysical values to maintain simulation stability while minimizing effective transmission.

At each target in each subject, 3 simulations were performed. One simulation placed a spatially smoothed Dirac impulse at the geometric focus (the target) and received the resulting time-varying pressure with the transducer array elements. Relative travel times to each of the elements were determined by detecting the leading edge of the arriving impulse. The other two simulations set all elements to transmit a 2-cycle pulse with 750-kHz central frequency. The

pulse was set from a waveform measured at the focus of a physical transducer in our lab with similar dimensions [147] under linear propagation conditions and analytically backpropagated to the transducer surface. In one of the 'transmit' simulations, all elements emitted the pulse simultaneously. In the other simulation, pulse emission by each element was time delayed to compensate travel time differences detected from the 'receive' simulation. For both transmit simulations, the maximum and minimum pressure amplitude were recorded at all grid points to obtain the focal pressure (maximum peak-to-peak pressure amplitude in the field). Outputs were scaled by relating maximum simulated focal pressure in the free field (water) to the maximum focal pressure of the physical transducer (80 MPa) estimated by extrapolation of hydrophone measurements at low (linear) amplitudes.

3.3 Results

The focal pressure varied substantially throughout the liver. Figure 3.3 maps the maximum achievable focal pressure by target in the liver both with and without aberration correction for one representative subject. Focal pressure was highest in shallow, subcostal regions of the liver and decreased for deeper and/or more cranial locations. With aberration correction, the focal pressure declined smoothly from subcostal regions to deeper, more cranial regions, creating a clear spatial gradient. Without aberration correction, spatial variation in pressure amplitude was more irregular. These spatial patterns in the focal pressure maps persisted across subjects. Without aberration correction, the focal pressure ranged from 11 MPa to 52 MPa. Aberration increased the focal pressure throughout all the liver, elevating the minimum and maximum

amplitudes to 17 MPa and 59 MPa. The greatest increase in focal pressure for one target was 190% (from 19 MPa to 36 MPa). Averaging across subjects, aberration correction increased the minimum focal pressure from 14 MPa ± 6 MPa to 20 ± 8 MPa and the maximum focal pressure from 53 ± 5 MPa to 60 ± 4 MPa.

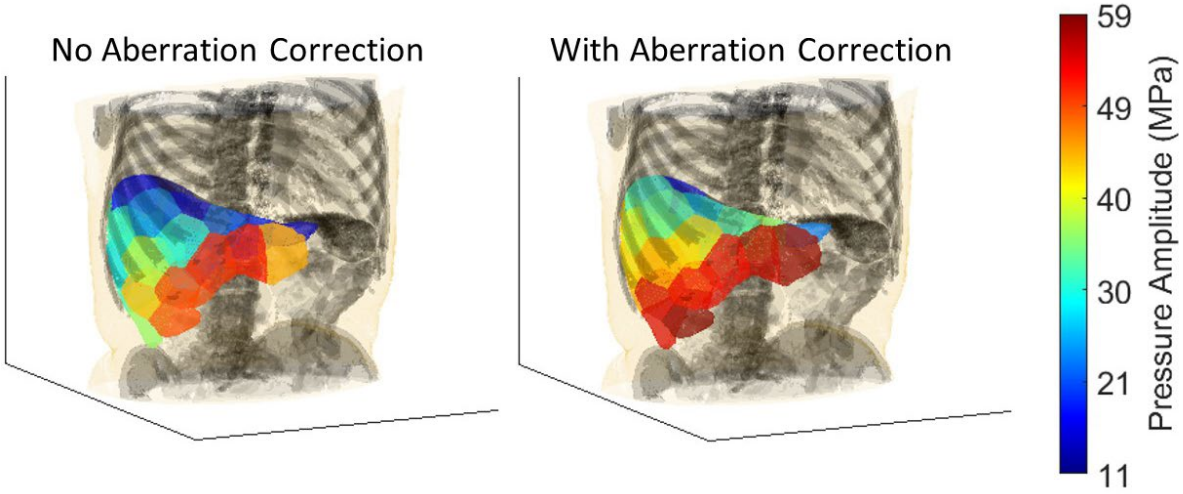


Figure 3. 3. Color-coded maps of the maximum achievable pressure amplitude per sub-volume in the liver of one subject with and without aberration correction.

Aberration correction increased the treatment envelope for histotripsy in the liver. Figure 3.4 plots the maximum achievable focal pressure against aperture blockage for all subjects and targets both with and without aberration correction. Rectangular regions at the bottom of the plots mark 20 MPa and 30 MPa, the nominal pressure amplitudes required to perform histotripsy with the shock scattering [34] and intrinsic threshold [58] mechanisms, respectively. On average, aberration correction increased the portion of the liver with focal pressure ≥30 MPa from 51 ± 23% to 75 ± 17% and increased the portion ≥20 MPa from 72% ± 19% to 83 ± 13%. As expected, the focal pressure decreased with increasing aperture blockage. Thus, several targets in cranial regions (from Couinaud segments III, IV, VII and VIII) had low (<20 MPa) maximum focal pressures. Without aberration correction, the focal pressures deviated

with large errors from a fitted linear relationship with blockage (R^2 = 0.65). Aberration correction decreased these errors, strengthening the relationship between focal pressure and blockage (R^2 = 0.79).

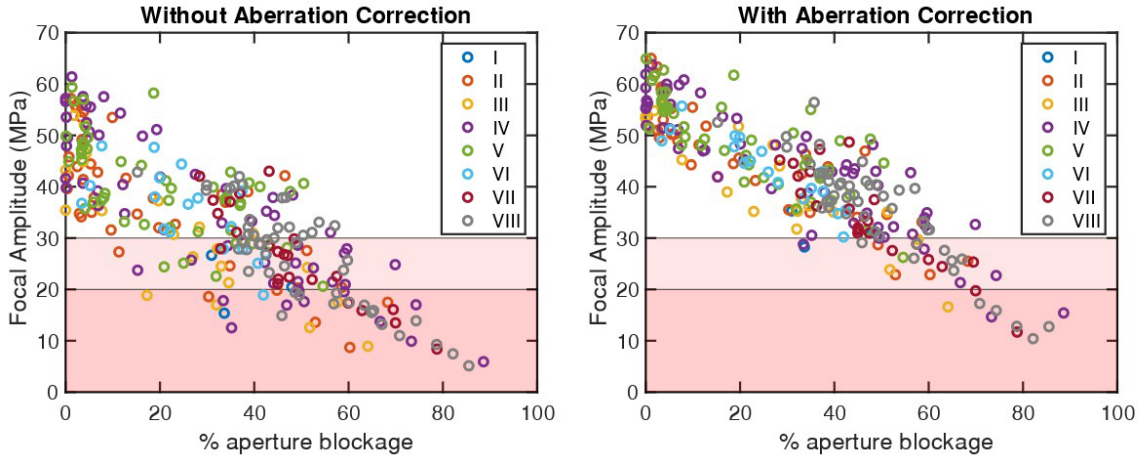


Figure 3. 4. Maximum focal pressure amplitude versus percent blocked aperture for all focusing targets in all subjects, with and without aberration correction. Marker colors denote the Couinaud segment. Shaded regions at the bottom of the plots mark 20 MPa and 30 MPa, the nominal pressure amplitudes required to perform shock-scattering histotripsy and intrinsic threshold histotripsy, respectively.

Figure 3.5 (a) shows the average maximum achievable focal pressure with and without aberration correction for each Couinaud segment. Without aberration correction, segments II, III, IV, V, and VI had high average focal pressures (>40 MPa), while segments I, VII, and VIII had lower average focal pressures (<30 MPa). Aberration correction increased the average focal pressure of all segments to >30 MPa. The pressure amplitudes in Figure 3.5 (a) represent maximum achievable outputs and therefore may exceed the amplitude required for effective therapy, especially for segments with low attenuation (II, III, IV, V, and VI). In this case, the principal benefit of aberration correction is to increase the focal gain and thereby reduce the acoustic input power required to perform therapy. The reduction in acoustic input power with aberration correction was estimated as $1 - \frac{P_{NAC}^2}{P_{AC}^2}$, where P_{AC} and P_{NAC} are the focal pressure

amplitude with and without aberration correction, respectively. The average power reduction of each Couinaud segment is given in Figure 3.5 (b). For all segments, the average power reduction exceeded 30%. Power reduction was greatest (>45%) for segments I and III.

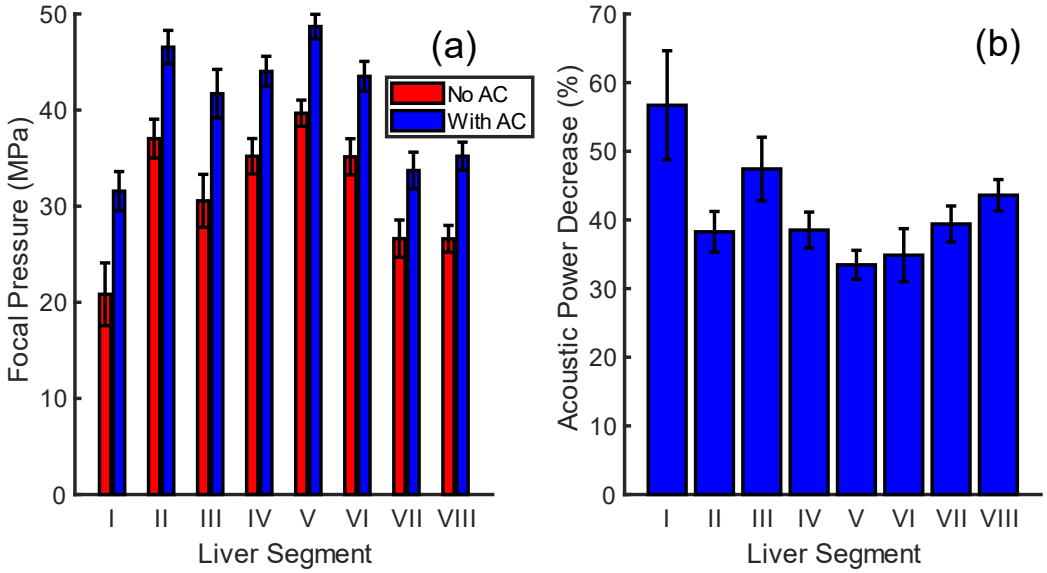


Figure 3. 5. (a) Average focal pressure by liver segment, both with (blue) and without (red) aberration correction. (b) Average percent reduction in the acoustic power input with aberration correction.

The size of the treatment envelope varied substantially across subjects. For intrinsic threshold histotripsy, the treatment envelope (percentage of the liver with focal pressure >30 MPa) ranged from 13% to 87% without aberration correction and from 53% to 97% with aberration correction. Figure 3.6 plots the treatment envelope versus (a) average aperture blockage and (b) estimated body mass index for each subject, both with and without aberration correction. As shown in Figure 3.6 (a), subjects with larger average blockage of the aperture tended to have smaller treatment envelopes. Treatment envelope size also tended to decrease with increasing body mass index (see Figure 3.6 (b)).

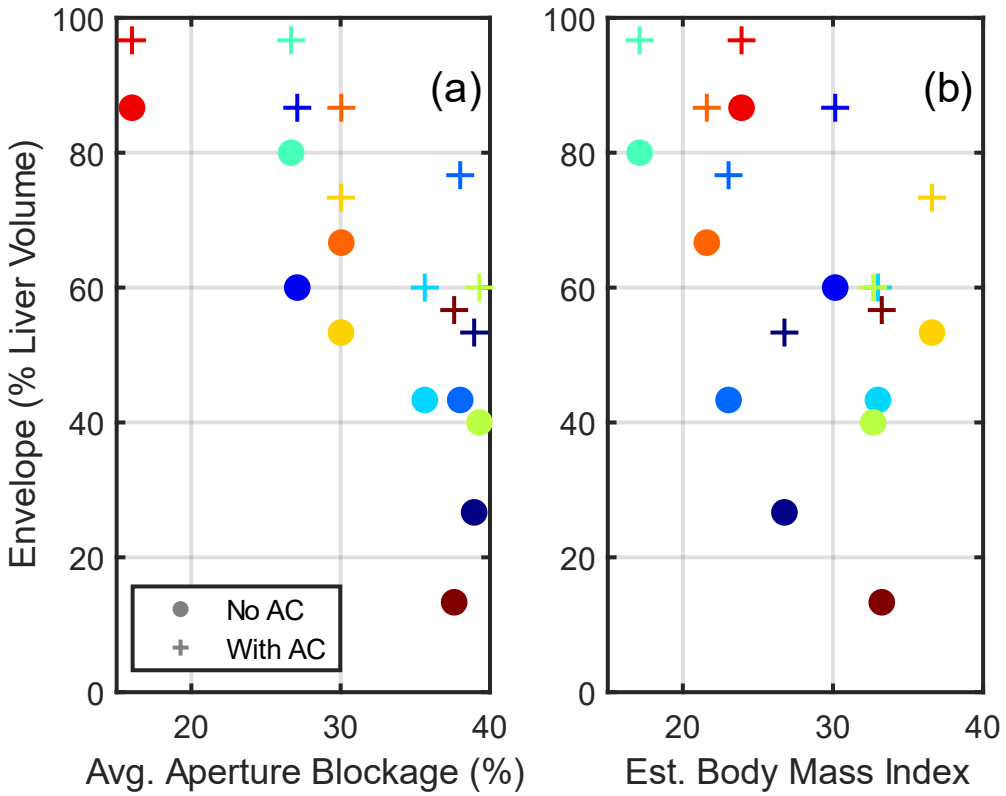


Figure 3. 6. Treatment envelope for intrinsic threshold histotripsy (volumetric region with maximum focal pressure above 30 MPa) in the liver of each subject according to average aperture blockage (a) and body mass index (b), both with (crosses) and without (dots) aberration correction. Different subjects are shown in different colors.

3.4 Discussion

Aberration correction could substantially expand the treatment envelope for histotripsy in the human liver. Simulating a phased array with similar dimensions and acoustic output to the current clinical device, aberration correction increased the average treatment envelope for intrinsic threshold histotripsy (the volume of the liver with maximum focal pressure >30 MPa) from 51% to 75% of the liver. For shock scattering histotripsy (>20 MPa), the average treatment envelope increased from 72% to 83%. These results suggest that aberration correction could enable histotripsy therapy at more locations in the liver and thereby permit treatment of more patients.

Aberration correction is critical to enable therapy at deeper, more cranial segments of the liver, where obstruction and absorption by ribs and lung strongly limit the focal pressure. For highly cranial liver segments (I, VII, and VIII), aberration correction was necessary to increase the average maximum pressure above 30 MPa, suggesting that without aberration correction, treatment of tumors in these locations would either exceed the acoustic output capability of the transducer or require very large acoustic power input, which increases tissue heating. At cranial segments I and III, aberration correction reduced the required power input by >45%. Power reduction of this magnitude would substantially reduce heating when treating cranial segments, where large portions of the acoustic path intersect highly absorbing ribs. For the more caudal, subcostal segments, aberration correction is not necessary to achieve sufficient focal pressure for therapy. However, at these locations, aberration correction still improves the safety of treatment by substantially reducing the required input power (by >30% in all segments). These findings indicate that aberration correction could improve the safety of current histotripsy treatments and enable therapy in regions that are not currently treated.

The extent of the treatment envelope varies substantially across patients. In this study, aberration correction expanded the treatment envelope to >96% of the liver in 2 subjects but to <50% of the liver in 5 other subjects. Blockage of the liver by ribs strongly limited the treatment envelope (see Fig. 3.6 (a)). For some subjects, like the one shown in Figure 3.7, large portions of the liver were below the ribs and thus acoustically accessible, producing a relatively large treatment envelope without aberration correction (53% of the liver). For the subject shown in Figure 3.8, most of the liver was obstructed by ribs, limiting the treatment envelope to just 13% of the liver without aberration correction. Notably, aberration correction expanded

the treatment envelope to 57% for this subject (an increase of 340%). This result indicates that phase correction is critical to overcome the combined attenuation from aberration and obstruction and thereby enable treatment for patients with highly obstructed livers.

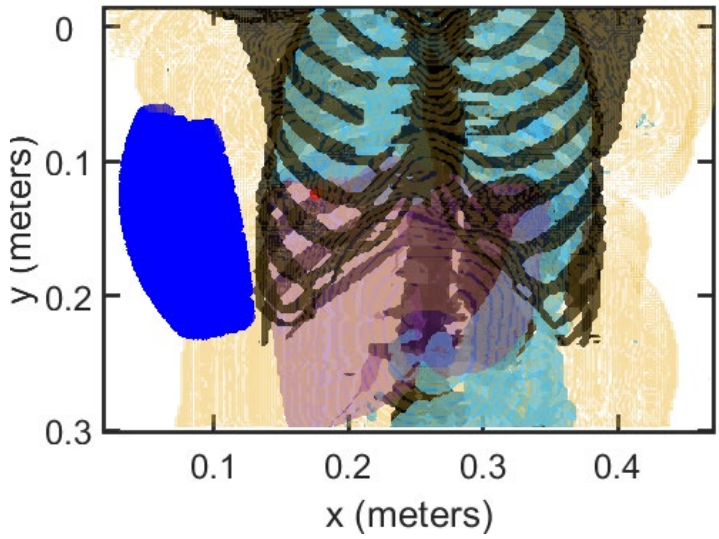


Figure 3. 7. One subject with low average blockage of the liver. The transducer (blue) is shown targeting a location (red) in the liver (purple), which is obstructed by ribs (black) and air pockets (cyan).

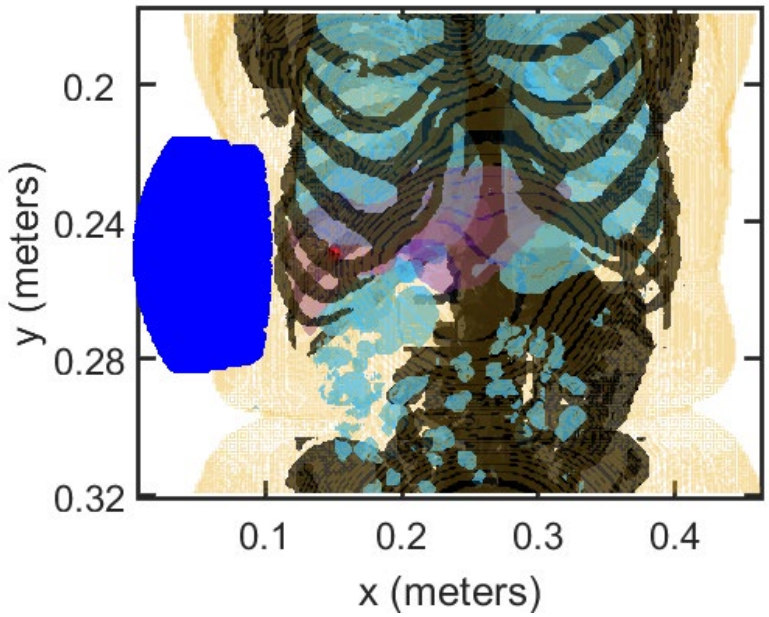


Figure 3. 8. One subject with high average blockage of the liver. The transducer (blue) is shown targeting a location (red) in the liver (purple), which is obstructed by ribs (black) and air pockets (cyan).

The treatment envelope also tended to decrease with increasing body mass. Body mass may limit the treatment envelope indirectly by restricting the range of possible orientations for the transducer. For larger patients, the transducer cannot be rotated far from the ribs without colliding into the body and thus encounters more obstruction than for smaller patients. These observations suggest that the feasibility of histotripsy treatment depends on the anatomy of each patient, including the obstruction of the liver and the body size, which both shape the acoustic window. Thus, the eligibility of each patient for histotripsy would ideally be evaluated individually with pre-operative acoustic simulations, a strategy which is currently used in other focused ultrasound modalities to plan treatments [181].

It should be noted that this study only included target locations in the liver within the working distance of the array. On average, this requirement excluded 13% of the liver (minimum of 0% and maximum of 27%). When calculating the treatment envelope, the excluded portions were counted as regions where histotripsy is not feasible. However, treatment may be possible at these locations by placing the transducer outside the body at a radial distance greater than the focal length and steering the focus to reach the target. Simulations of such scenarios have been attempted but have shown unexpected errors. Specifically, the phase correction decreases the focal pressure relative to no correction in some of these cases, suggesting that the time reversal principle is being violated. These problems may result from numerical errors in the k-Wave simulation that arise when large portions of the acoustic medium are strongly absorbing, as is often the case for these deep-seated, highly obstructed targets. These locations require further investigation and will be included in future studies. By excluding these locations, the current study may underestimate the treatment

envelope. However, because these locations typically have a highly obstructed acoustic window, their inclusion is unlikely to strongly increase the estimated treatment envelope.

Two additional limitations may cause this study to underestimate the treatment envelope. First, focal pressures were calculated by relating simulated output to the output of a physical histotripsy transducer at maximum power. This pressure cannot be measured due to the generation of cavitation at high amplitudes and therefore must be estimated. For this study, we estimated the maximum output by measuring the focal pressure as a function of electrical input power at much lower amplitudes (3 – 25 MPa) and extrapolating via a fitted polynomial [66]. This method may underestimate the pressure output at high amplitudes. An alternative method is to measure the maximum output of small sub-apertures of the array individually and then sum these measurements to approximate the full array [66]. However, this summation method ignores nonlinear distortion effects at high amplitudes and thus overestimates the focal pressure. The second limitation is that the images used for simulations represent the abdomen without any compression (e.g., without an overlying water bath bolus). Without compression, the simulated abdomens likely limit the acoustic window (range of feasible transducer positions) more than a compressed abdomen would and thus artificially decrease the maximum achievable focal pressure. However, the water bolus compresses the abdomen by only a few centimeters and is not expected to strongly alter the estimated treatment envelope.

3.5 Conclusion

This study presents the first quantitative estimates of the treatment envelope for transabdominal histotripsy in the human abdomen. The results indicate that aberration

correction can substantially expand the treatment envelope for transabdominal histotripsy in the human liver. The extent of the treatment envelope varies substantially across different patients. Aberration correction will be most critical to enable histotripsy treatment for patients with tumors in locations highly obstructed by air pockets and ribs.

Chapter 4
Aberration Correction of Transabdominal Histotripsy using Cavitation Emissions: *In vitro* study

Previous work has shown that the acoustic emissions from cavitation can serve as "point sources" for aberration correction. This study compared the efficacy of soft tissue AC for histotripsy using acoustic cavitation emissions (ACE) from bubble cloud nucleation and collapse. A receive-capable histotripsy array was pulsed to generate cavitation in ex vivo porcine liver through an intervening abdominal wall. Received ACE signals were used to determine the arrival time differences to the focus and compute corrective delays. Corrections from single pulses and from the median of multiple pulses were tested. On average, ACE AC obtained 96% ± 3% of the pressure amplitude obtained by hydrophone-based correction (compared with 71% ± 5% without AC). Both nucleation- and collapse-based corrections obtained >96% of the hydrophone-corrected pressure when using medians of ≥10 pulses. When using single-pulse corrections, nucleation obtained a range of 49%–99% of the hydrophone-corrected pressure, while collapse obtained 95%–99%.

*Note: This chapter was adapted from the publication listed below.

1. **Yeats E**, Lu N, Sukovich JR, Xu Z, Hall TL. Soft Tissue Aberration Correction for Histotripsy Using Acoustic Emissions From Cavitation Cloud Nucleation and Collapse. Ultrasound in Medicine & Biology. 2023 May 1;49(5):1182-93.

4.1 Introduction

The simulation results from Chapters 2 and 3 show that aberration strongly decreases the focal pressure amplitude of transabdominal histotripsy. Decreased focal pressure amplitude weakens the bubble cloud, hindering therapy. Efficient ablation of a large tissue volume requires a large, robust bubble cloud, which is generated at rarefactional pressures well above the cavitation threshold (P^- >40 MPa) [182]. Pressure amplitudes near the cavitation threshold (P^- = 25 – 31 MPa) generate small bubble clouds incapable of efficient homogenization. Therefore, aberration can stifle treatment by limiting the size of the bubble cloud. Sometimes, pressure loss can be overcome by increasing the transducer output power. However, because aberration reduces the focusing gain, the energy delivered to intervening tissues also increases, which can intensify unsafe tissue heating. Aberration therefore limits the safety, efficiency, and efficacy of large volume treatments with histotripsy.

The goal of this Chapter was to develop an aberration correction method to restore focal pressure amplitude and focusing gain in transabdominal histotripsy. As discussed in Section 1.3, the ideal signal to correct aberration is a point source or beacon. Prior work has shown that acoustic emissions from cavitation can serve as beacons for aberration correction [111], [120], [133]. Histotripsy non-invasively generates cavitation for therapy and thus creates beacon signals as a natural consequence [131]. Transient histotripsy cavitation bubbles emit various acoustic signals coinciding with their initial nucleation, oscillation, and eventual collapse [128]–

[130], [183]. On excitation by a sufficiently high-amplitude rarefactional pressure, inertial cavitation bubbles form and expand rapidly [167]. The explosive growth of each bubble during its nucleation produces an acoustic shock wave that propagates spherically outward [63], [132]. After reaching a maximum radius, the bubbles contract and collapse, emitting another shock wave [33], [184]–[186]. Following this first collapse, the bubble cloud can rebound to expand and collapse a second (and even a third) time, emitting additional shock waves [137].

Macoskey et al. demonstrated the feasibility of cavitation-based aberration correction for histotripsy using the signal from bubble cloud nucleation [63]. The nucleation signal has relatively large amplitude and could therefore be detected using a low sensitivity receiver. However, the nucleation signal may not be an effective beacon for aberration correction. During nucleation, all bubbles forming the cloud emit shockwaves. Because the bubbles are typically spaced by less than one-half of a wavelength at the array central frequency, the nucleation signal is less coherent than a true point source, decreasing the accuracy of the resulting phase estimates. Consequently, correction using the nucleation signal only increased the focal pressure to 77% of the amplitude achieved by correction with a hydrophone (the laboratory gold standard) [134].

Unlike nucleation, the cavitation cloud collapse typically emits a single shockwave and therefore may better approximate a point source. However, selection of a suitable beacon for AC is complex and depends on multiple factors. A singular shock wave is desirable but must have sufficiently high signal amplitude to allow detection through thick layers of tissue. Furthermore, bubble cloud behavior is dynamic and varies with focal pressure amplitude. The

properties of bubble emission signals (and their performance as beacons for AC) therefore depend on the amplitude and shape of the focus [66], [187].

This study investigates the collapse signal as a potential beacon for transabdominal histotripsy aberration correction and compares its performance to the signal from nucleation at varying input focal pressure amplitudes of the therapy array. A range of relatively low "baseline" focal pressures (near the cavitation threshold) is used to simulate strong pressure loss form aberration. We first investigate the emissions from bubble cloud nucleation and collapse optically and acoustically using high-speed images and hydrophone measurements. Then, we assess the aberration correction performance of collapse and nucleation emissions using ex vivo tissue and a phased array with geometry like that of the device currently being used in clinical trials for histotripsy ablation of liver tumors. The results of this study will help determine the signals and signal processing strategies that are most effective for histotripsy soft tissue aberration correction based on acoustic emissions.

4.2 Methods

4.2.1 Histotripsy Phased Array

This study specifically considered histotripsy as mediated by the intrinsic threshold mechanism, which generates cavitation using very short (≤2-cycle) pulses with a single high amplitude rarefactional pressure phase [58], [188]. Experiments were performed using a receive-capable 750-kHz histotripsy phased array with dimensions closely matching the device currently in clinical use. The array (14.2-cm focal radius) has a truncated circular aperture with maximum transverse extents of 23.4 and 16.5 cm (f-numbers 0.61 and 0.86, respectively) and a

4-cm circular cutout at the apex, as shown in Figure 4.1 (a). The aperture is divided into 260 tightly spaced, arc-shaped transducer elements of ~11.5 mm × 11.5 mm area arranged in concentric rings around the array center with >90% packing density [147]. The array was controlled by a custom-built electronic driving system that uses field-programmable gate arrays (FPGAs) to permit individual transmission and reception by each array element. For transmission, elements were pulsed using a 1.5-cycle, 3-μs sinusoidal electric input. The input voltage to the driver could be adjusted to transmit acoustic pulses of varying pressure amplitude. Each transducer element can be assigned an individual time delay to vary its transmission phase as needed for aberration correction. Following transmission at amplitudes exceeding the inertial cavitation threshold for soft tissue (~25 – 31 MPa) [188], acoustic signals from bubbles were captured by setting all elements to receive simultaneously. Each element had a current-sensing circuit to detect acoustic signals arriving at the element. Received signals were amplified and digitized by a standard ultrasound imaging front end integrated circuit with programmable gain amplifier (AFE5801, Texas Instruments, Dallas, Texas, USA). The receive system sensitivity was evaluated by comparing with calibrated hydrophone measurements. At the maximum gain setting, the peak-to-peak amplitude of the noise floor was found to be 5 Pa. The same setting had a saturation level of 1.1 kPa (47 dB greater). At the minimum gain setting, saturation occurred at 1.5 MPa. Throughout this study, received signals were digitized to 12 bits at a 25-MHz sampling rate before being transferred to a computer for analysis.

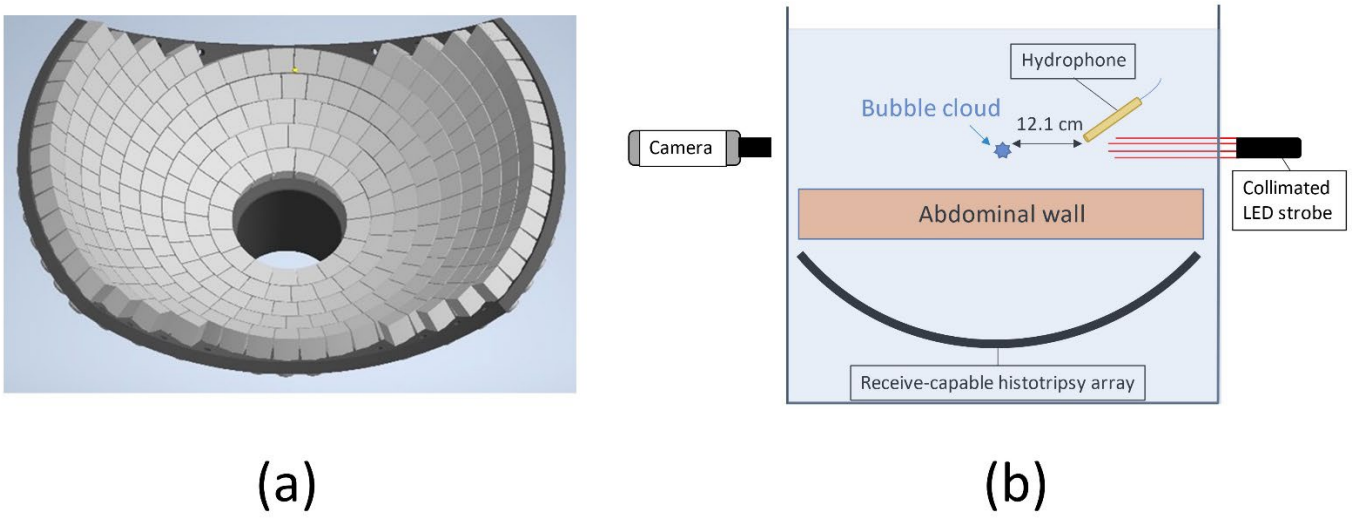


Figure 4. 1. (a) CAD model of the receive-capable histotripsy phased array used in this study. **(b)** The experimental setup used to investigate histotripsy cavitation emissions optically and acoustically. The histotripsy array from (a) generated cavitation in de-gassed water behind a sample of porcine abdominal wall tissue. A broadband hydrophone recorded acoustic cavitation emissions at its position 12.1 cm away from the focus and in the focal depth plane. A camera and collimated LED strobe light source acquired optical 'shadowgraph' images of cavitation bubbles and emitted shockwaves.

4.2.2 Optical and Acoustical Investigation of Histotripsy ACE Signals – Comparison of Bubble Cloud Nucleation and Collapse

Acoustic emissions corresponding to bubble cloud nucleation and collapse were investigated both optically and acoustically using the following experimental setup and procedure. The array described above was placed in a tank of de-gassed, deionized water. To assess how propagation through tissue affects the nature of the bubble emissions, a ~4-cm thick sample of excised porcine abdominal wall (skin, fat, muscle, connective tissue, and the 2 caudal-most segments of cartilaginous rib) was placed in between the transducer and its geometric focus, as shown in

Figure 4.1 (b). A needle hydrophone (HNR-0500, Onda Corporation, Sunnyvale, California, USA) was connected to a digital oscilloscope (Picoscope 5443D, Pico Technology, St. Neots, Cambridgeshire, UK) and placed orthogonally to the array axis at the focal depth with its tip ~12.1 cm from the geometric center. A high-speed camera (Phantom v210, Phantom Research, Wayne, New Jersey, USA) was positioned opposite a collimated LED light source (XLamp XP-E2 625 nm, Cree LED Inc, Durham, NC, USA) controlled by a custom-built driver circuit to deliver a strobe flash with a 26-ns pulse width. The camera was optically focused on the geometric focus of the array with a 1.9 × 1.9 cm field of view. Prior to imaging the shockwaves, "background" frames were acquired so that inhomogeneities in the illumination of the field of view could be removed from frames containing shockwaves in post processing. For optical and acoustic data acquisition, all array elements transmitted synchronously at a low (1 Hz) pulse repetition frequency (PRF) to produce a transient bubble cloud with each pulse. Coincident with the initiation of each transmitted pulse, the camera opened its shutter for an exposure time of 440 μs. Shadowgraph images of shockwaves emitted at nucleation and collapse were obtained by timing the flash of the strobe to correspond with each shockwave emission event. Acoustic measurement by the hydrophone and by all array elements also began at the initiation of the transmitted histotripsy pulse and continued for a total duration of 400 μs, sufficiently long to encompass the bubble cloud lifespan. Hydrophone signals were acquired at a 125-MHz sampling frequency and then high-pass filtered to attenuate frequencies below 2 MHz and thereby remove the transmitted histotripsy pulse signal and its reflections. Images and acoustic measurements of both nucleation and collapse were acquired at 3 transducer power settings. The lowest (baseline) setting was the lowest driving voltage that produced detectable collapse

signals during >20% of delivered pulses (at least 10 detectable collapse signals for every 50 generated bubble clouds). The other two settings increased the baseline driving voltage by 10% and 20%. The baseline, 10%-increase, and 20%-increase power settings generated linearly estimated focal pressures of 31, 33 and 36 MPa P^-, resulting in 1 – 3 inertial cavitation bubbles, a sparse multi-bubble cloud (<10 bubbles) and a larger (<30 bubbles) multi-bubble cloud, respectively.

4.2.3 ACE-Based Aberration Correction

After investigating the nature of the shockwaves optically and acoustically, we assessed their performance as beacons for histotripsy aberration correction in soft tissue. For histotripsy, the aim of aberration correction is to detect and compensate for differences in time of arrival at the array focus among the sound waves emitted by the individual transducer elements. The acoustic path in the forward (transducer elements to array focus) and backwards (array focus to transducer elements) directions should be equivalent via the principle of time reversal [7]. Therefore, shockwaves originating from the array's focus and propagating back to the array should accumulate arrival time differences equivalent to those accumulated in the forward direction [111], [189]. Arrival time differences detected from received shockwaves can thus be used to correct aberration in transmission.

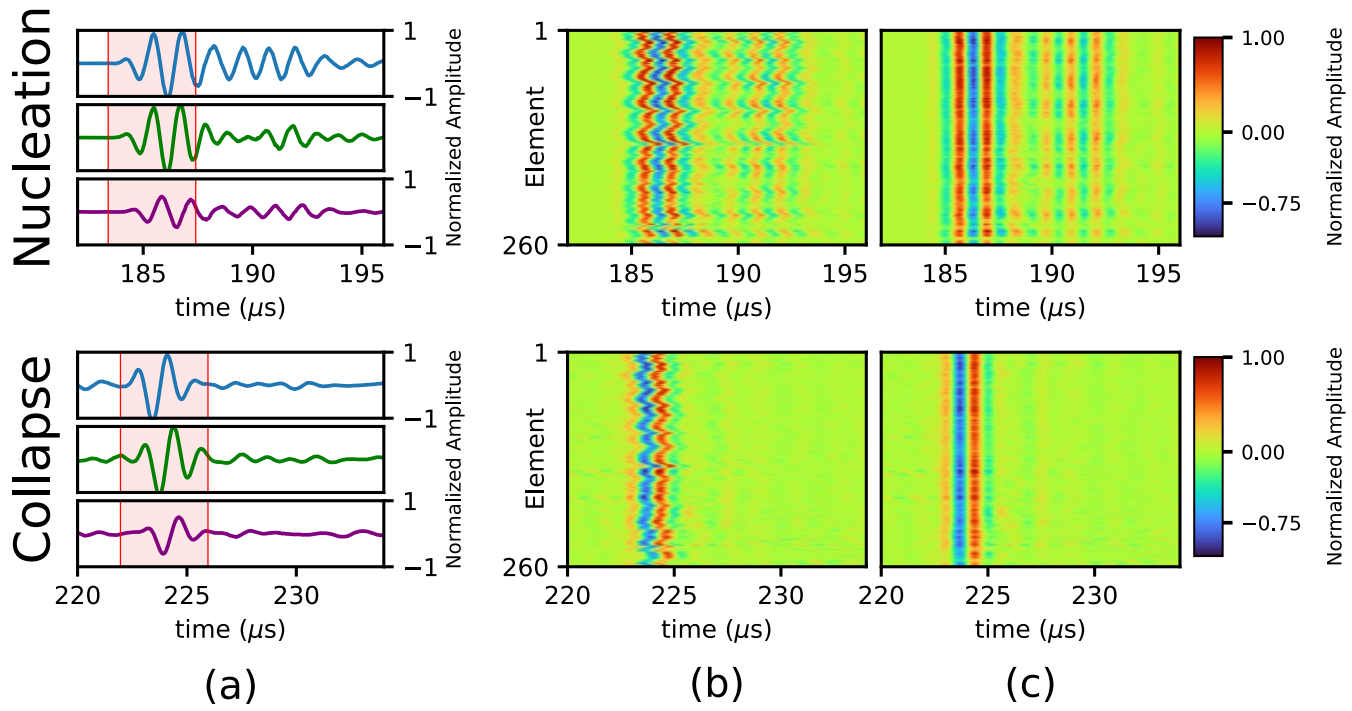


Figure 4. 2. Signals received by the histotripsy array corresponding to cavitation cloud nucleation (top) and collapse (bottom). (a) Signals acquired by 3 elements. The time windows used for cross correlation appear as red rectangular shaded regions. (b), (c) The received wavefield from 1 pulse before (b) and after (c) correction using cross correlation delays. All amplitudes are shown on a normalized scale.

Arrival time differences were detected from ACE shockwaves using the following procedure. 50 histotripsy pulses were delivered to generate cavitation. After every delivered pulse, ACE signals were recorded using all array elements over time windows appropriate for nucleation or collapse. For nucleation, signals were received between 180 – 210 µs following transmission, accommodating the round-trip travel time of sound to the focus (~190 µs) and the duration of the nucleation signal (~10-15 µs on array elements at the maximum transducer power setting tested). Compared to nucleation, the duration of the collapse signal is shorter (~3 µs on array elements), but its time of occurrence fluctuates stochastically from pulse to pulse and varies with input focal pressure amplitude (collapse occurs later for larger bubble clouds). Over the range of input focal pressures tested in this study, collapse occurrence varied between 210 –

280 μs following transmission. This window (210 – 280 μs) was therefore used to acquire collapse signals. Also, because nucleation and collapse shockwaves have different amplitudes, the received signal gain was adjusted before each acquisition to optimize the dynamic range (i.e., higher gain was used for collapse). After data acquisition, for each channel the acquired signals were median filtered (across all pulses) to identify the acoustic background signal (e.g., pulse reflections from tissues). Tissue reflections are constant across repeated pulses, while bubble nucleation is stochastic and thus causes nucleation emissions and the collapse timing to vary from pulse to pulse. The acoustic background signal from each element could therefore be extracted by median filtering and subtracted from the original signals to isolate the ACE signals. After background subtraction, a user-defined amplitude threshold was applied to identify whether cavitation was generated for a given pulse; pulses where cavitation was not detected were omitted from analysis. Pulses with cavitation were truncated by setting a time window of 4 μs (3 cycles at the central frequency) around the cavitation event with maximum amplitude. This time window was selected to encompass the duration of one shockwave (~3 μs) plus the expected arrival time variation from porcine abdominal wall (<0.6 μs). The short time window was used to limit errors from correlation between the signals from multiple shockwaves. Examples of time-windowed nucleation and collapse signals are shown in Figure 4.2 (a) as recorded on 3 elements. The time-windowed signals were then upsampled to 50 MHz and cross correlated using the element signal with highest amplitude as the reference kernel. The lags that maximized the cross-correlation values were converted to seconds and inverted to create corrective delays. Figure 4.2 (b) and (c) show the nucleation and collapse signals from one pulse

before and after alignment with corrective delays, respectively. The correction was further refined by taking the median across the delay sets computed for 10 pulses.

The above procedure was implemented and tested in all aberration correction experiments (7 total). One experiment additionally tested ACE-based corrections from single pulses and from the medians of corrections from 5, 10, 15 and 20 pulses. For the nucleation-based corrections in this experiment, background signal was removed by delivering an additional pulse at half of the amplitude used by the histotripsy pulses. This additional, sub-cavitation threshold pulse contained tissue reflections only and could thus be scaled by 2 and subtracted from the histotripsy pulses to reduce background signal. For the collapse-based corrections using 5, 10, 15 and 20 pulses, the background was extracted via median filtering and subtracted as described above. For the corrections computed from a single collapse event, 2 histotripsy pulses were delivered and subtracted. From the resulting difference, the collapse event with largest amplitude was used to compute the correction.

4.2.4 Evaluation of ACE-based Aberration Correction with *Ex Vivo* Porcine Tissue

4.2.4.1 Tissue Preparation

ACE-based aberration correction was evaluated using *ex vivo* porcine tissue. Abdominal wall tissue (skin, muscle, fat, connective tissue, and segments of the 2 caudal-most cartilaginous ribs) was used to create aberration, while a piece of liver was used as the target tissue to generate cavitation. Tissues were acquired *postmortem* from 7 female swine that were euthanized as part of a separate, unrelated study approved by the University of Michigan Institutional Animal Care and Use Committee. From each animal, a ~4-cm thick, ~24-cm × 16-

cm wide section of abdominal wall and a sample of liver were excised and stored in saline. Before experiments, the tissues were de-gassed for >2 hours and embedded in de-gassed porcine skin-derived gelatin (G2500, Sigma-Aldrich, St. Louis, Missouri, USA) to fix their position.

4.2.4.2 ACE Signal Acquisition

The following procedure was used for all experiments. The histotripsy array was placed in a water tank. The abdominal wall tissue was suspended in the sound path, leaving a 3-4 cm gap between the abdominal tissue and the array geometric focus. The liver tissue (~1 cm-thick) was positioned at the focal region. Signals for ACE AC were acquired for each combination of emission type (nucleation and collapse) and transducer power setting (baseline, baseline+10%, and baseline+20%) as follows. Before each acquisition, the liver sample was shifted to place the focus in a fresh portion of tissue. The array transmitted 50 pulses at low (1 Hz) repetition rate without any phase corrections (*i.e.*, all elements firing in phase). For each pulse, bubble emissions (when present) were received and processed according to the procedures outlined in Section III. Once corrections were computed from the received signals, the array was pulsed at 100 Hz PRF using low (linear) amplitude to test each set of corrective delays.

4.2.4.3 ACE AC Performance Evaluation

ACE AC was compared to a hydrophone-based correction method (HP AC), which served as the “gold standard.” To obtain the hydrophone correction, the liver tissue was removed. A hydrophone (CA-1135, Dynasen Inc, Goleta, California, USA) was placed at the location of maximum pressure amplitude. Then, each element was pulsed individually for 128 repetitions. The resulting hydrophone signals were averaged and saved. The arrival time for each element

was determined from cross correlation and converted to corrective delays as described in Section 5.2.3.

Aberration correction performance was evaluated using 2 primary metrics: focal pressure amplitude and focal volume. Focal pressure amplitude was defined as the maximum peak-to-peak amplitude of the pressure field. To facilitate comparison with the gold standard, all focal pressure amplitudes were normalized to the hydrophone-corrected focal pressure amplitude for the given experiment. Focal volume was approximated as an ellipsoid space wherein the pressure amplitude exceeds 50% of the maximum. Focal volume V was thus estimated from the full-width at half maximum (FWHM) of the 1-D pressure profiles in all 3 axes as $V = \frac{\pi}{6} \times FWHM_x \times FWHM_y \times FWHM_z$. In addition to these metrics, 2-D cross sectional maps of the pressure field were obtained in the array's transverse plane for ACE AC, HP AC, and no aberration correction (no AC). The 2-D maps and 1-D profiles along the transverse axes had 5-mm extent with 0.25-mm spacing, while the 1-D profiles along the depth axis had 14-mm extent with 0.5 mm spacing.

ACE AC is known to displace the focus relative to its location before correction [134]. This displacement is separate from and additional to the shift of the focus caused by aberration, which shifts the focus from the array geometric center. The displacement by ACE AC results from small deviations between the focus (spatial point of maximum pressure) and the spatial origin of cavitation bubbles. Due to these deviations, the cavitation emission signals encode a "steering" component that displaces the ACE-corrected focus relative to its location before correction. This displacement can increase targeting error. Therefore, the focal displacement

due to ACE AC was measured for all experiments and was defined as the distance between the focus location with aberration before and after correction. For comparison, the focal shift due to refraction, defined as the distance between the focus with and without aberration (and no correction), was also recorded.

4.3 Results

4.3.1 Optical and Acoustic Investigation of Histotripsy ACE Signals – Comparison of Nucleation and Collapse

Figure 4.3 shows example shockwave images and hydrophone recordings of nucleation and collapse at the maximum transducer power setting tested. Nucleation resulted in the emission of multiple spherical shockwaves that overlapped closely in space and time. The corresponding hydrophone signal spanned ~3 μs and had a peak-to-peak pressure amplitude of 84 kPa. Collapse, on the other hand, generated a single shockwave that produced a much shorter (~0.3 μs) and smaller (15 kPa peak-to-peak) signal. The collapse signal had a single broadband “spike”, characteristic of a singular shockwave, while the nucleation signal comprised several superimposed spikes, characteristic of multiple interfering shockwaves.

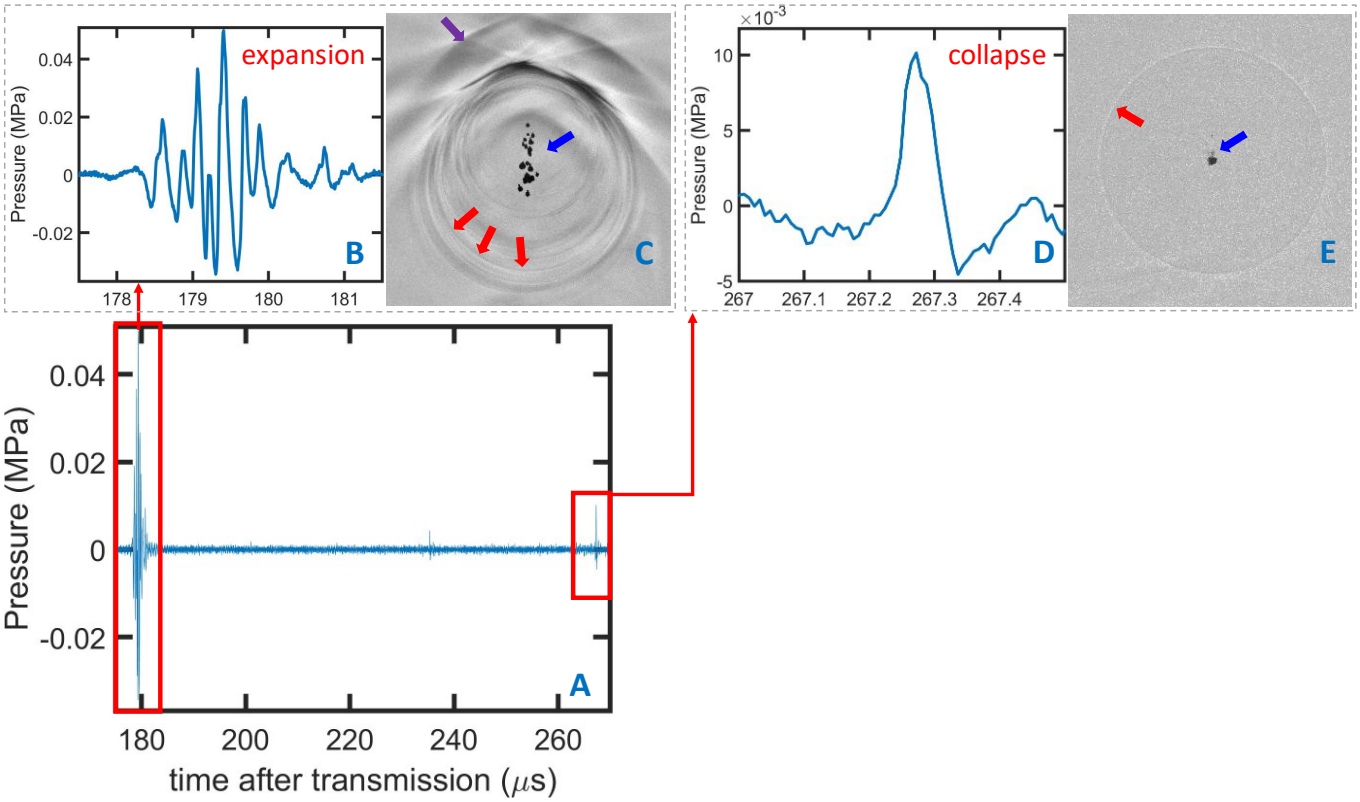


Figure 4. 3. Shockwaves from a histotripsy bubble cloud: (a) Hydrophone recordings of emissions from a histotripsy cavitation cloud, spanning nucleation to collapse. (b), (c) Hydrophone recording (b) and shadowgraph image (c) of the bubble cloud nucleation. (d), (e) Hydrophone recording (d) and shadowgraph image (e) of bubble cloud collapse. Cavitation bubbles, emitted shockwaves, and the transmitted pulse wavefront are marked by blue, red, and purple arrows, respectively.

The complexity and duration of the nucleation signal increased with source amplitude, while the collapse signal was highly consistent. Figures 4.4 and 4.5 show example hydrophone recordings and corresponding shockwave images for nucleation and collapse, respectively, at the 3 transducer power settings tested. In both figures, transducer power increases from left to right. The number of shockwaves emitted during nucleation increased with the size of the bubble cloud (and thus with the transducer power). Consequently, the nucleation signals increased in duration, amplitude, and complexity, growing from a short (~0.3 µs), lower amplitude (28 kPa peak-to-peak), singular spike at the lowest power to a longer (~3 µs), larger (96 kPa peak-to-peak) signal composed of multiple superimposed spikes at the highest power. Collapse, on the other hand, typically generated a single shockwave, independent of cloud size.

Occasionally, multiple collapse events were observed, as shown in the middle panel of Figure 4.5. The shadowgraph image obtained at 33 MPa P- shows two collapsing bubbles: one bubble (foreground, center) emitted the imaged shockwave, while the other (background, top) emitted a shockwave shortly before the image flash time. The corresponding hydrophone signal obtained at 33 MPa P- thus shows two shockwaves spaced by ~2.5 µs in time. In most cases, multiple collapse shockwaves were well-separated in time.

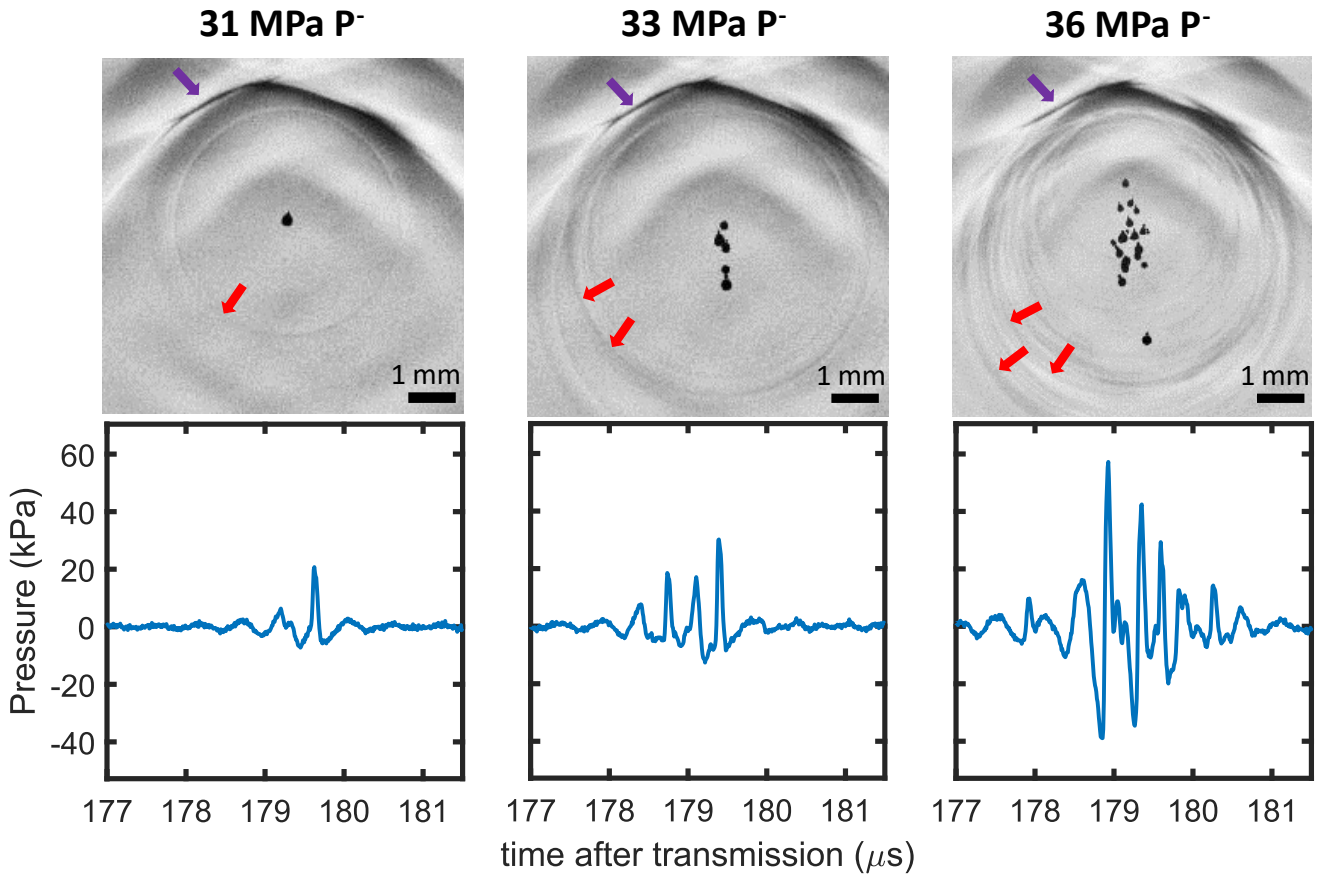


Figure 4. 4. Shockwave images (top) and hydrophone recordings (bottom) of bubble cloud nucleation at varying focal pressure amplitudes. In the shockwave images, the direction of sound propagation is from bottom to top. Red arrows mark shockwave profiles. Purple arrows mark the transmitted pulse wavefront.

The timing of collapse varied with source amplitude, while the timing of nucleation was consistent. Collapse time was later at larger source amplitudes and varied between 0 – 80

µs after the end of nucleation over the amplitude range tested here. The collapse time also fluctuated from pulse to pulse due to the stochastic nature of bubble cloud activity. Nucleation, on the other hand, had consistent timing across focal pressures, with the largest bubble cloud expanding slightly (<1 µs) earlier than the smallest bubble cloud, in agreement with previous observations [134].

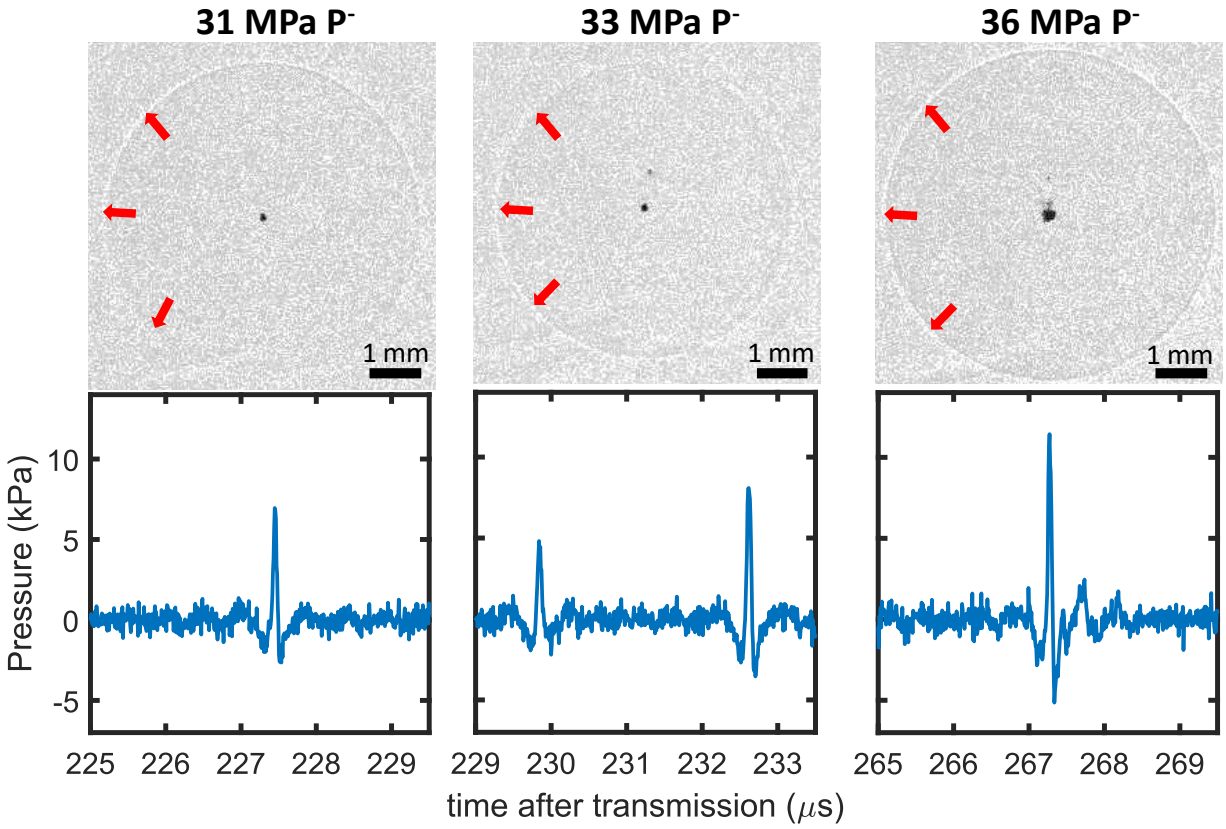


Figure 4. 5. Shockwave images (top) and hydrophone recordings (bottom) of bubble cloud collapse at varying focal pressure amplitudes. In the shockwave images, the direction of sound propagation is from bottom to top. Red arrows mark the shockwave profile.

4.3.2 Evaluation of ACE-Based Aberration Correction with *Ex Vivo* Porcine Tissue

Collapse-based aberration correction resulted in higher focal pressure amplitudes than nucleation-based correction when the corrections were computed from a single pulse, but both signals performed similarly when using the medians of 10 or more pulses. Figure 4.6 (a) plots the focal pressure amplitude obtained for one tissue sample at the highest tested power setting using nucleation- and collapse-based corrections computed from different numbers of pulses. Collapse-based corrections from single collapse events consistently increased the focal pressure to nearly match HP AC. Corrections based on single collapses attained a mean focal pressure amplitude of 0.98 HP AC with a sample standard deviation of .02 HP AC. For nucleation, corrections from single pulses had a more varied performance, attaining a mean focal pressure amplitude of 0.86 HP AC with a sample standard deviation of 0.17 HP AC. However, nucleation-based AC improved markedly after taking the median of corrections computed from ≥10 pulses. Medians of 10 or more nucleation pulses effectively matched the performance of collapse-based corrections, increasing the focal pressure to >0.96 HP AC.

Corrections based on the medians of multiple pulses also reduced the focal displacement caused by ACE-based AC. Figure 4.6 (b) plots the focal displacement caused by ACE-based corrections computed from different numbers of pulses. Corrections from single pulses displaced the focus by up to 3.2 mm (up to 1.1 mm for collapse). On the other hand, all median corrections displaced the focus by <0.6 mm (<0.5 mm for collapse). For both focal displacement and focal pressure amplitude, differences in performance among medians of 10 or more pulses were small. Therefore, all further experiments used 10-pulse medians for ACE AC.

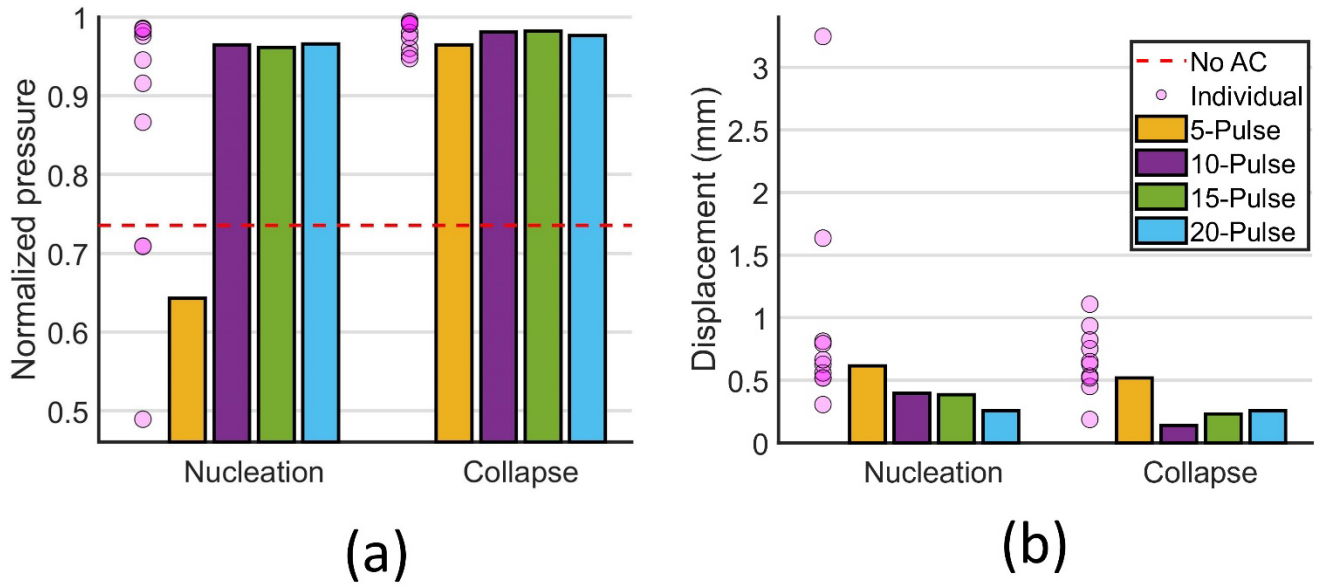


Figure 4. 6. Aberration correction using acoustic cavitation emissions from varying numbers of pulses: (a) Focal pressure amplitude, normalized w.r.t. hydrophone correction, and (b) focal displacement for one tissue sample, obtained using nucleation and collapse corrections computed from 10 individual pulses and from medians of 5, 10, 15, and 20 pulses transmitted at the highest tested transducer power setting. 'No AC' denotes 'no aberration correction.'

Soft tissue ACE AC closely approximated the performance of hydrophone correction, the gold standard method. Figures 4.7 (a) and (b) compare the focal pressure amplitude and focal volume, respectively, attained using ACE AC, HP AC, and no AC across all 7 experiments. Averaging over all ACE corrections (n = 42), ACE AC attained a focal pressure amplitude of 0.96 ± .03 HP AC. Without correction, the focal pressure was 0.71 ± .05 HP AC (n = 7). Differences in the focal pressure achieved following nucleation- and collapse-based corrections were small. The mean focal pressure attained using nucleation-based correction was 0.95 HP AC compared to 0.97 HP AC using collapse-based correction. Collapse-based AC performed consistently across source amplitudes, while nucleation-based AC attained slightly higher focal pressure (0.97 HP AC) at the lowest power setting compared to 0.93 and 0.95 HP AC at the +10% and

+20% power settings, respectively. The difference in mean performance between nucleation- and collapse-based corrections was not statistically significant at the lowest power setting but was significant (5% confidence) at the higher power settings.

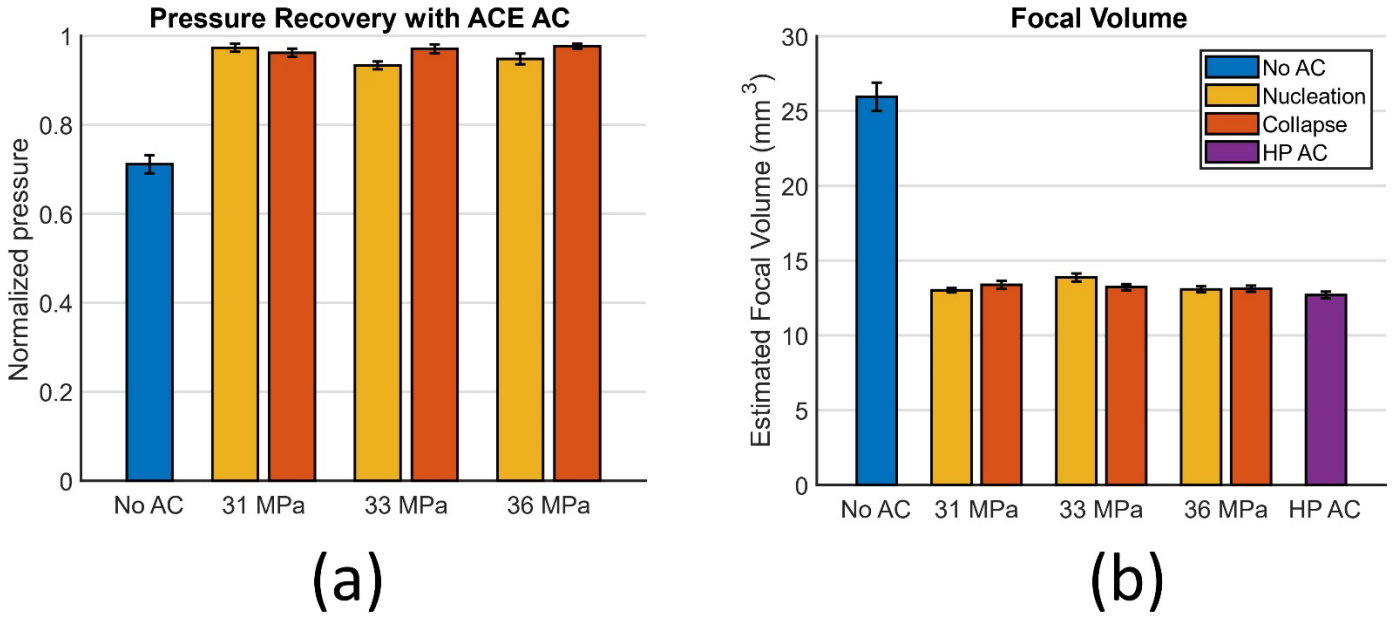


Figure 4. 7. Comparison of aberration correction using different cavitation emission signals: Bar plots comparing the performance of no aberration correction, hydrophone aberration correction, and acoustic cavitation emissions (ACE)-based aberration correction (AC) using nucleation and collapse at varying transducer power settings. Transducer power is referenced as the peak negative pressure expected at the focus without correction (i.e., 31, 33 and 36 MPa P-). Colored bars denote sample means (n = 7). Error bars denote standard errors. (a) Focal pressure normalized to hydrophone-based aberration correction (HP AC). (b) Estimated focal volume.

Similarly, ACE AC reduced focal volume to nearly match hydrophone correction. The mean focal volume across all ACE AC methods was 13.3 mm^3, compared to 12.7 mm^3 for HP AC. The focal volume reduction was consistent across ACE AC methods, with a standard deviation of 1.5 mm^3. Without aberration correction, the mean focal volume was 26 mm^3, double the corrected volume. There were no significant differences in focal volume between nucleation- and collapse-based AC at any transducer power setting.

ACE AC displaced the focus by up to 1 mm from the uncorrected location on average at the power settings tested. Figure 4.8 compares the focal displacements between nucleation- and collapse-based corrections and across varying transducer power settings. Focal displacement was larger for higher power settings (larger bubble clouds). At the lowest power setting, focal displacement was 0.5 ± 0.2 mm for both nucleation- and collapse-based corrections. Increases in the transducer power of 10% and 20% extended the average focal displacement to 0.7 ± 0.5 mm and 0.8 ± 0.5 mm, respectively. Most of the displacement (~88%, on average, across all signals and power settings) was along the transducer depth axis. The average focal shift from aberration (relative to the no aberration case) was 3.8 mm (3.5 mm along the transducer depth axis).

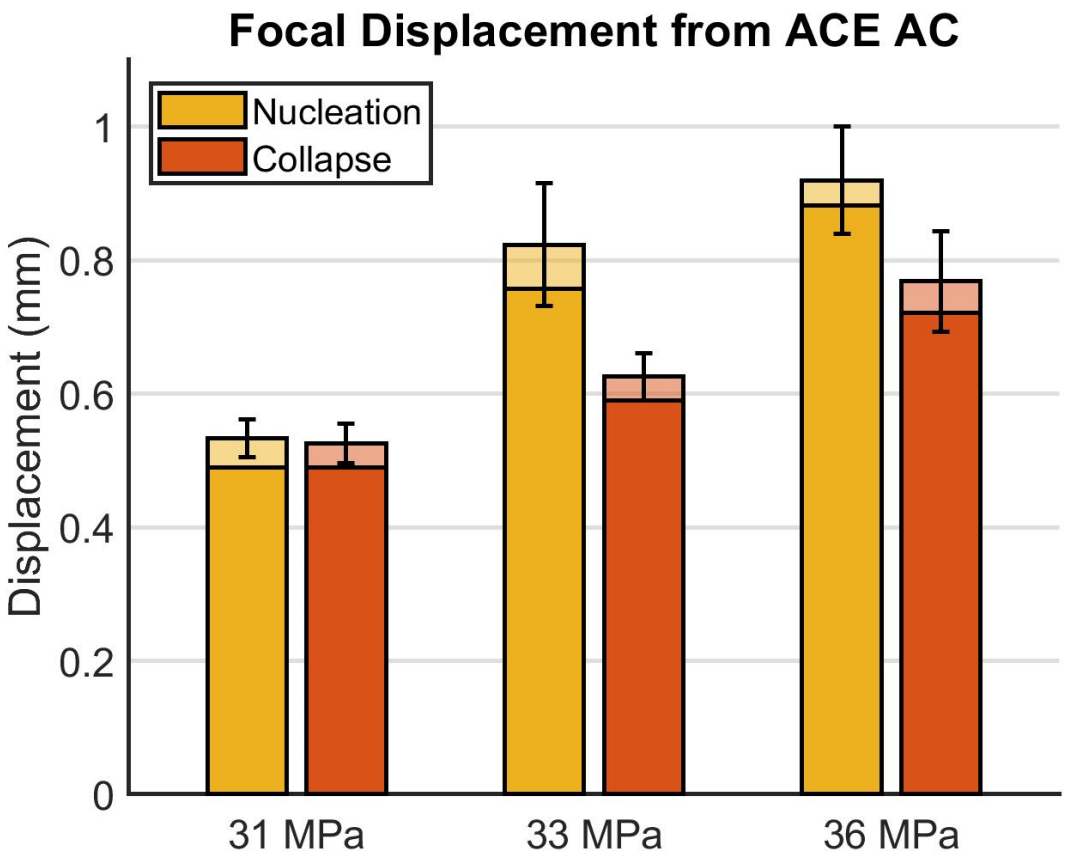


Figure 4. 8. Focal displacement due to acoustic cavitation emission (ACE) aberration correction (AC): Average displacement of the focus from the aberrated (uncorrected) location, obtained using nucleation and collapse at varying transducer power settings. Transducer power is referenced as the peak negative pressure expected at the focus without correction (i.e., 31, 33 and 36 MPa P^-). Solid color bars denote the magnitude of the shift in the axial (depth) direction. Transparent bars denote the full shift (Euclidean distance between the focus with and without correction). Error bars denote the standard error (*n*=7).

On average, collapse shockwave arrival times at the transducer elements matched the hydrophone measured arrival times of the per-element histotripsy pulses at the array's focus more closely than the nucleation shockwaves. Figure 4.9 maps the per-element arrival times (relative to the median) for one representative abdominal wall sample as measured in the forward direction (transducer elements to array focus) using the hydrophone, and reverse direction (array focus to transducer elements) using the array elements to capture the shockwaves from nucleation and collapse. The ACE-based arrival times shown were acquired from bubbles generated using the highest source amplitude tested. The overall pattern in the arrival delays matched well across all measurement methods. However, nucleation shockwaves showed larger per-element variabilities in arrival times than was observed for the collapse shockwaves. The root-mean-squared error (RMSE) between the hydrophone and nucleation shockwave arrival delays was 0.20 μs versus 0.06 μs for the collapse shockwaves. Part of the RMSE resulted from the displacement of the shockwave origin away from the focus; the displacements, as measured by scanning the hydrophone after inverting and applying the arrival time differences as element-to-element delays in transmission, were 0.4 mm and 0.1 mm for nucleation and collapse, respectively. The remaining RMSE quantifies the measurement inaccuracy of each ACE-based detection method. The difference in RMSE between nucleation and collapse persisted across tissue samples and source pressure amplitudes; the mean RMSE

was 0.19 μs for nucleation shockwaves compared to 0.12 μs for the collapse shockwaves, which was significant at the 5% confidence level.

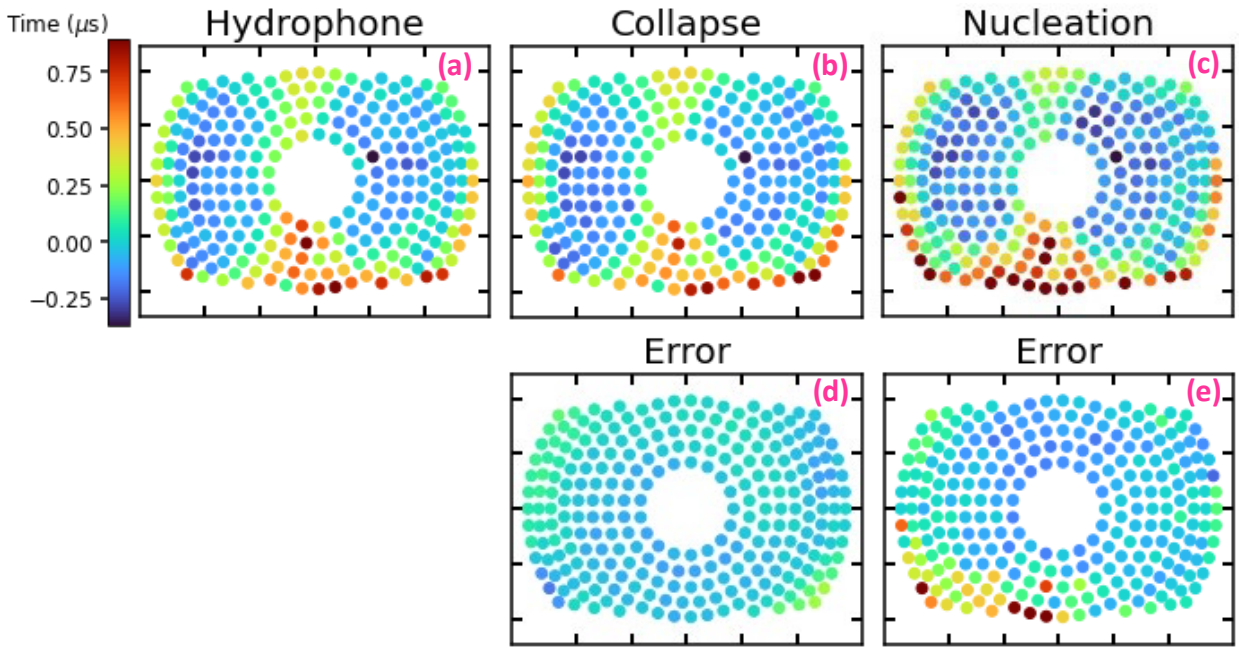


Figure 4. 9. Arrival time differences measured using hydrophone, collapse, and nucleation signals: (a), (b), (c) Color-coded array maps of relative element-to-element arrival times measured using hydrophone (a), collapse (b), and nucleation (c) signals. (d), (e) Differences from the hydrophone arrival times for collapse (d) and nucleation (e).

ACE-based correction improved focusing quality through abdominal tissue. Figure 4.10 shows transverse cross-sectional maps of the pressure field about the array's focus through one abdominal wall sample with no aberration correction, nucleation- and collapse-based correction at the highest power setting, and hydrophone-based correction. Without correction, the focus had a diffuse, irregular shape. Aberration correction resulted in a narrowed, elliptical focus with reduced side lobes. Both nucleation- and collapse- based AC closely matched the hydrophone AC pressure field map, except for the slightly higher side lobe shown in the bottom portion of the images (Fig. 4.10 (b) and (c)).

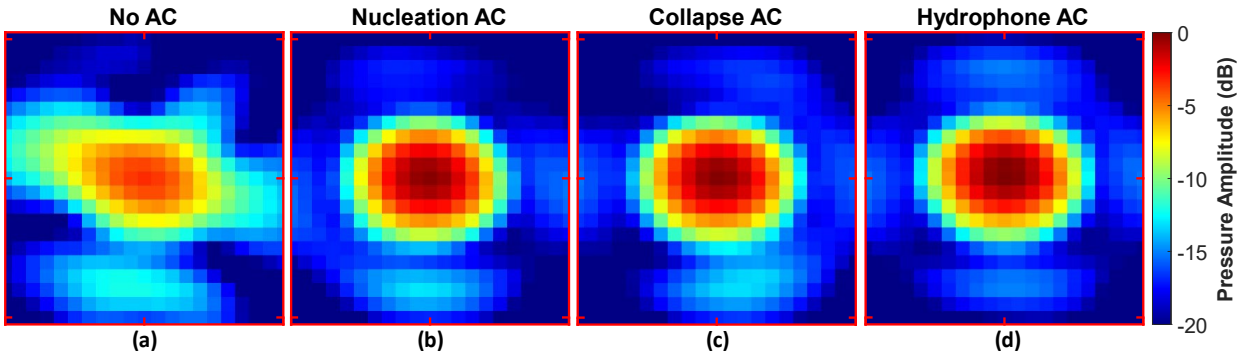


Figure 4. 10. Focusing quality with aberration correction (AC): (a) - (d) Cross section maps of the log-compressed pressure field in the transverse focal plane with no aberration correction (a), nucleation-based correction (b), collapse-based correction (c), and hydrophone-based correction (d). Cavitation-based corrections were performed at the highest transducer power setting tested. Maps extend 5 × 5 mm and are centered at the focus (peak amplitude location).

4.4 Discussion

Soft tissue aberration correction using histotripsy cavitation emission signals approximates the performance of gold standard, hydrophone-based correction. In the experiments described here, ACE AC increased the focal pressure amplitude to 96% of the hydrophone-corrected amplitude, on average, and achieved the same effective focal volume (Fig. 4.7 a,b). These results indicate that ACE AC can correct for nearly all induced focal pressure amplitude losses and focal distortions due to soft tissue aberration. ACE AC could therefore improve focusing quality and thus histotripsy ablation through soft tissue.

Collapse emissions approximate an ideal point source. As shown by Fig. 4.5, collapse typically emits a singular spherical shockwave that produces similar signals across all elements. Due to this similarity, the cross correlation can accurately determine arrival time differences from a single collapse event. Nucleation, on the other hand, emits multiple interfering shockwaves (see Fig. 4.4) that produce distinct signals on different elements. To reduce this ambiguity, the cross-correlation window was restricted to the duration of a single shockwave.

This shortened time window limits confounding errors from correlation with shockwaves emitted at different locations or timepoints. Because a single shockwave could not generally be isolated, the cross correlation of nucleation signals from a single pulse was more likely to produce inaccurate phase estimates than collapse. However, nucleation-based correction was substantially improved by taking the median of the phase estimates from multiple pulses. The multiple-pulse median removes pulse-specific errors from overlapping shockwaves while preserving time of arrival differences from aberration (Fig. 4.6). As a result, nucleation matched the performance of collapse in this study and recovered a higher percentage of the hydrophone-corrected pressure than observed previously by Macoskey et al [134]. The two studies cannot be directly compared because they used different transducers. However, we note that the previous method averaged the analytic envelopes of the nucleation signals from multiple pulses and then isolated the first-arriving shockwave by detecting the leading edge. The average (unlike the median) can obscure the arrival time differences, while edge detection (unlike cross correlation) is highly sensitive to amplitude differences. The methods used in this study permit effective ACE-based aberration correction with both nucleation and collapse shockwaves.

Because cavitation emissions can originate from slightly off-focus locations, the location of the focus following ACE AC can be displaced with respect to the location before correction. At the lowest tested source pressure, single bubble emissions resulted in displacements of ~0.5 mm. At higher pressures, clouds grew larger and more elongated, resulting in larger (~0.8 mm) displacements along the array's depth direction. These results suggest that larger focal displacements could be avoided by using a single bubble for ACE AC. Alternatively, the spatial

offset could be estimated using an optimization scheme and compensated for when generating the corrective delays [106]. It is important to note that the focal displacement caused by ACE AC is distinct from and additional to the focal shift caused by aberration, which is typically larger. Here, aberration from the abdominal wall samples shifted the focal location, with respect to the array's geometric focus, by 3.8 mm on average (3.5 mm pre-focally along the depth direction). The focal shift from aberration cannot be corrected using ACE-based methods and generally requires a simulation-based approach [76], [79]–[81], [84].

ACE AC was shown to be effective at "baseline" peak negative pressures that approached the threshold for inertial cavitation in soft tissue (25 - 31 MPa P^-) [188]. The highest tested peak negative pressure (~36 MPa P^-) generated clouds of <30 bubbles (Fig. 4.7 c), which is much smaller than the large, robust clouds desired for histotripsy ablation (>40 MPa P^-). ACE AC nonetheless performed well at all tested source pressures (see figure 4.7). This finding has two important implications. First, ACE AC could be implemented even with strong focal pressure loss from soft tissue aberration. Second, single bubbles could be used for ACE AC without loss of efficacy. ACE AC is an inherently destructive method of aberration correction and requires generating cavitation in tissue to estimate element-to-element arrival times. Conceivably, transducer power could be slowly increased until a single inertial cavitation bubble is generated at the focus for correction. Use of a single sub-millimeter bubble would reduce the transducer power required for aberration correction and minimize the amount of tissue damage incurred by ACE AC.

The results of this study suggest that ACE AC could improve histotripsy therapy through soft tissue. Aberration reduces focal pressure amplitude (Fig. 4.10 a), thereby limiting the size

of the bubble cloud. Small, weak bubble clouds create small lesions and are insufficient for ablating tissue volumes [60]. Phase correction with ACE can increase the focal pressure amplitude (Fig. 4.10 b-c) to generate a large, robust cloud that destroys tissue efficiently and homogeneously. Here, ACE AC was evaluated using a single (low f-number) transducer geometry, which produces a sharp focus and dense bubble clouds [190]. However, ACE AC could likely estimate arrival times with similar accuracy for higher f-number geometries, which produce a broader focus and more diffuse clouds. Here, a similar correction performance was observed when using a single shockwave emitted by one cavitation bubble and when using a cluster of tightly overlapping shockwaves from many nucleating bubbles, suggesting that ACE AC is robust to the number and spatial density of bubbles. Therefore, transducer geometry and focal shape are unlikely to affect the accuracy of arrival time prediction with ACE AC. It is likely, however, that if used with a higher f-number transducer, ACE AC would induce larger focal shifts than those observed here, because the bubble emissions are more likely to originate farther from the focal center.

It should be noted that ACE AC estimates arrival times under linear propagation conditions. At the large amplitudes used in histotripsy, significant nonlinear effects are observed, which may produce aberrations unaccounted for by ACE-based AC. However, nonlinear effects are unlikely to significantly affect the performance of ACE AC for two reasons. First, histotripsy transducers typically have a very low f-number (≤1), which limits nonlinear distortion to a small region around the focus [190], [191]. Therefore, linear effects dictate sound propagation speed along most of the beam path. Second, significant nonlinear distortion is exhibited by the compressional pressure phase, which sharpens due to the generation of

higher order harmonics, while the rarefactional pressure phase broadens and is thus less sensitive to small changes in arrival time incurred near the focus [192], [193]. Because the rarefactional pressure field governs histotripsy under the intrinsic threshold mechanism, nonlinear effects are unlikely to substantially alter focusing or the performance of ACE-based aberration correction.

This study demonstrates the *in vitro* feasibility of ACE AC for histotripsy through soft tissue. However, the implementation of ACE AC *in vivo* poses additional challenges not addressed here. In transabdominal histotripsy, respiratory motion cyclically alters the geometry of intervening tissues and therefore the element-to-element phase relationships. Traditional methods to maintain focusing quality despite motion include (1) a breath-hold technique to momentarily halt respiration and (2) a "gating" method that restricts active therapy to a portion of the breath cycle where the phase correction is valid. However, both approaches significantly extend treatment times. ACE AC, unlike speckle-based AC techniques, does not require iteration and therefore may permit a continuous correction that updates with signals received from each successive therapy pulse. If the therapy pulse rate is sufficiently high, then respiratory motion in between subsequent pulses will be small. Although algorithm speed was not optimized in this study, all computation for the tested corrections executed on a PC without parallelization in ~200 ms. This computation speed would permit 15 updates per breath cycle (at 20 breaths per minute). ACE AC thus has the potential to operate in "real time" and thereby maintain short treatment times.

Breathing motion also complicates the removal of background "noise" from the ACE signals *in vivo*. Most experiments in this study subtracted the median of 50 pulses fired at the

same target location to reduce signal from tissue reflections and improve SNR for correction. However, 50 pulses repeated at typical therapy rates (100 Hz) would take 0.5 s, throughout which the abdominal wall could shift substantially. This number (50 pulses) permits assessment of the upper limit of ACE AC performance but likely exceeds the number of pulses needed for effective aberration correction. Lu *et al* subtracted the collapse emissions from 2-pulse pairs to correct transcranial histotripsy aberration [84]. Here, it was found that collapse-based corrections from subtracted pulse pairs and from medians of 5 pulses performed similarly to corrections using higher numbers of pulses. For a small number of subsequent pulses (2 - 5), background subtraction could be implemented without substantial movement of tissue. This strategy is investigated in Chapter 5.

This study focused on soft tissue aberration and did not address aberration by bone. (In these experiments, ribs occluded <10% of the array aperture.) Frequency-dependent attenuation by bone can distort ACE signals and could thus limit arrival time detection efficacy for portions of the wavefront passing through ribs. However, correction of phase aberrations induced by ribs may have limited clinical value, because sound passing through bone is strongly attenuated and thus unlikely to contribute substantially to the focal pressure amplitude. Furthermore, absorption of sound by ribs heats surrounding tissue. One strategy to minimize heating when targeting transcostally might be to detect obstructed array elements by exploiting the ACE signal amplitude information. Signals received by obstructed elements have significantly lower amplitude than un-obstructed elements. Thus, ACE signal amplitude could be used to identify and 'turn off' obstructed elements. Then, the phase information from un-

obstructed elements can be used for arrival time correction of sound passing through the soft tissue between ribs.

Finally, cavitation-based techniques for aberration correction *in vivo* have two important disadvantages. First, the cavitation used for correction can potentially damage non-target tissue if the focus is shifted from the target by refraction. ACE AC cannot correct for this focal shift because the cavitation emissions arise from the refraction-shifted focus location. To correct the focus location, ACE AC must be preceded by an imaging-based correction approach. One approach might be to synchronize the acquisitions from an ultrasound imaging array with low amplitude (sub-threshold) emissions from the therapy transducer to visualize the therapy focus in real-time without generating cavitation [194]–[197]. However, this technique may be limited in regions where ultrasound imaging is poor or by its dependence on user skill. Another potential approach is to use images acquired directly before treatment to avoid complications from elastic tissue deformation. As discussed in Section 1.3, a cone-beam computed tomography (CBCT) system was recently integrated with a histotripsy therapy system by Wagner *et al*. to automate treatment targeting [198]. Point-of-care CBCT images could be used with a rapid acoustic propagation model to predict and correct phase errors for focusing at the target. The modelling-based approach can likely correct focal shift but is unlikely to recover substantial pressure amplitude, due to the limited ability to resolve and accurately assign acoustic properties to different tissues [84], [133]. Therefore, a two-step approach as originally proposed by Gateau *et al.* should be applied to first correct focal shift using images and then recover substantial pressure amplitude using ACE AC [133].

A second disadvantage of ACE AC is that the generation of cavitation for correction can be hindered or prevented in situations of severe pressure loss from aberration. If the pressure amplitude is below the intrinsic threshold for the generation of cavitation with a single pulse, cavitation could be initiated by using an alternate pulsing scheme. One strategy might be to apply many correction pulses at high PRF (>1000 Hz) to generate cavitation at amplitudes below the intrinsic threshold. Sending many pulses in succession could help increase the probability of generating single cavitation bubbles at subthreshold pressures, as in shock scattering [58]. Here, correction performance did not vary with bubble cloud size or emission signal type, suggesting that the bubbles generated at high PRF could be used for ACE AC. This strategy is investigated in Chapter 5.

4.5 Conclusion

In this study, we developed and tested a soft tissue aberration correction (AC) technique for histotripsy based on acoustic cavitation emissions (ACE) from bubble cloud nucleation and collapse. In experiments with *ex vivo* porcine tissue, ACE AC recovered nearly all focal pressure amplitude lost due to soft tissue-induced aberrations. The emission from cavitation cloud collapse approximates an ideal point source for aberration correction and therefore produces more accurate arrival time estimates than emissions from nucleation when using a single bubble cloud. However, when combining the arrival time estimates from multiple independent bubble clouds, both nucleation- and collapse-based correction nearly matched the performance of gold standard (hydrophone-based) aberration correction. The results of this study suggest

that ACE AC can substantially improve focusing quality through heterogeneous soft tissues for histotripsy therapy.

Chapter 5
Aberration Correction of Transabdominal Histotripsy using Cavitation Emissions: *In vivo* study

Chapter 4 showed *in vitro* that the phase errors from aberration can be corrected by receiving the acoustic signals emitted by cavitation. For transabdominal histotripsy *in vivo*, however, cavitation-based aberration correction is complicated by acoustic signal clutter and respiratory motion. The study in Chapter 5 develops a method that enables robust, effective cavitation-based aberration correction *in vivo* and evaluates its efficacy in the swine liver. The method begins with a high-speed pulsing procedure to minimize the effects of respiratory motion. Then, an optimal phase correction is obtained in the presence of acoustic clutter by filtering with the singular value decomposition. This aberration correction method reduced the power required to generate cavitation in the liver by 24% on average (range: 10% to 54%) and required ~2 s per focus location. These results suggest that the cavitation-based method could enable fast and effective aberration correction for transabdominal histotripsy.

*Note: Portions of this chapter were published as listed below.

1. **Yeats E,** Stocker G, Sukovich JR, Xu Z, Hall TL. In vivo soft tissue aberration correction for histotripsy using acoustic cavitation emissions. The Journal of the Acoustical Society of America. 2023 Mar 1;153(3_supplement):A103-.

5.1 Introduction

Cavitation-based AC using the collapse signal faces significant challenges *in vivo.* The *in vivo* tissue path is intact and thus produces more acoustic 'clutter' from ultrasound reflections than *in vitro*, where the excised tissues are separated by a water path [199], [200]. These reflections can obscure the collapse shockwave, which is a relatively low amplitude signal (<100 kPa peak-to-peak [201]), thereby hindering detection of the propagation time differences. The clutter signal cannot be removed by frequency-based filtering due to the narrow bandwidth of the therapy array. *In vitro*, tissue reflections have fixed timing, while the cloud collapse is stochastic and has variable timing. Therefore, the collapse signal can be isolated from reflection clutter *in vitro* by subtracting the signals received from repeated histotripsy pulses. The propagation time differences can then be determined via cross correlation of the collapse signals received by different transducer elements, as shown in Chapter 4 [84], [201]. *In vivo*, however, tissue motion causes the arrival time of reflections to vary and thus compromises the pulse-to-pulse subtraction. Therefore, the implementation of ACE AC for transabdominal histotripsy will require new signal processing strategies that address tissue motion and increased acoustic clutter *in vivo*.

The objective of this Chapter was to develop methods that enable robust and precise cavitation-based aberration correction using the collapse signal for transabdominal histotripsy *in vivo*. First, the method rapidly pulses the histotripsy array (at 1 kHz) in short bursts to

minimize the effect of tissue motion and permit effective pulse-to-pulse subtraction of received signals. Then, we take advantage of the spatial coherence properties of the collapse shock wave to isolate the collapse signal from the remaining tissue reflection clutter. Finally, to determine the phase errors, we replace the cross-correlation operation, which is sensitive to residual tissue reflection 'noise,' with an analytical approach based on the singular value decomposition (SVD). The efficacy of the ACE AC procedure was evaluated in a swine model and quantified as the reduction in acoustic power input required to generate cavitation in the liver. To maintain clinical relevance, we demonstrated the AC procedure using a histotripsy phased array with similar geometry to the FDA approved HistoSonics Edison™ platform. The results of the study show that the collapse-based method can achieve robust, effective aberration correction *in vivo* to improve the safety and efficiency of transabdominal histotripsy treatments.

5.2 Methods

5.2.1 Animal handling and *in vivo* experimental setup

This study was approved by the University of Michigan Institutional Animal Care and Use Committee. Four male swine (~45 kg) were anesthetized and intubated with mechanically assisted ventilation. Anesthesia was induced via intramuscular injection of zolazepam (Telazol; Zoetis, Kalamazoo, MI) and xylazine and sustained via inhalation of isoflurane gas. To facilitate acoustic coupling, the swine was laid supine, depilated, and covered in a mixture of ultrasound gel and degassed water. Then, a flexible membrane containing degassed, deionized water was

placed on the abdomen over the liver. Following experiments, the animals were euthanized via intravenous injection of sodium pentobarbital.

This study used the same 750-kHz, receive-capable histotripsy transducer array as in Chapter 4, which has similar dimensions to the current clinical device (see section 4.2.1) and is shown in Figure 5.1 (a). The setup for the *in vivo* aberration correction experiments is shown in Figure 5.1 (b). The histotripsy array was supported by a mechanical robotic arm (UR5, Universal Robots, Odense, Denmark) that enabled translation and rotation of the array in 3 dimensions. A 4.5-MHz ultrasound imaging transducer (C2-7-D, General Electric, Boston, MA) was inserted coaxially through the central hole of the histotripsy array and connected to a clinical imaging system (Loqic E10, General Electric, Boston, MA) to provide B-mode imaging guidance for targeting. The histotripsy array and coaxial imager were submerged in the coupling water bath to target the swine liver. For each of the 4 swine, the cavitation-based AC procedure was performed at 5 – 7 different locations in the liver.

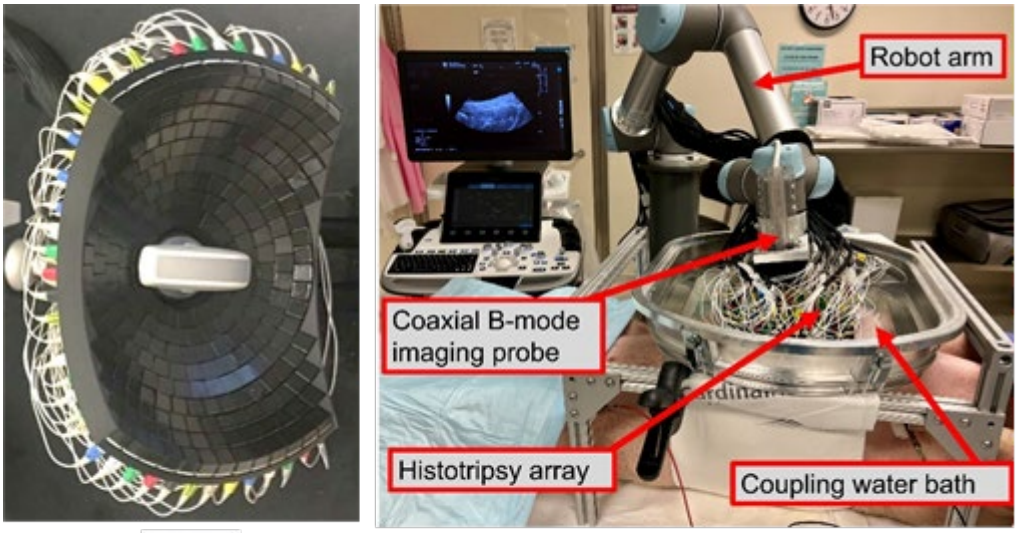


Figure 5. 1. (a): Receive-capable histotripsy array with 260 trapezoidal elements arranged in concentric rings. A central port permits insertion of an ultrasound imaging probe for qualitative image guidance. (b): The histotripsy array and a coaxially inserted ultrasound imaging probe were coupled to the pig abdomen via a bath of de-gassed water and repeatably positioned in 3 dimensions by a robotic arm for in vivo experiments.

5.2.2 *In vivo* cavitation-based aberration correction procedure

To determine the phase errors (time delays) for aberration correction, the collapse shockwave must be isolated from larger amplitude signal clutter (*e.g.*, multiple reverberations across tissue layers and specular reflections from inhomogeneities like blood vessels and bile ducts). Removal of the signal clutter is complicated by tissue motion, which continuously alters the arrival time of the reflection signals. Additionally, the narrow frequency band of the histotripsy transducer precludes any frequency-based filtering. To overcome these challenges, the *in vivo* ACE AC procedure takes advantage of special properties of the collapse shockwave, including its high spatial coherence and the dependence of its timing on focal pressure amplitude. The procedure is divided into 4 steps.

5.2.2.1 Step 1: Acquire collapse shockwave signals at high rate to minimize the effects of tissue motion

Tissue reflection clutter can be reduced by subtracting the signals from repeated acquisitions if the motion between acquisitions is small. Therefore, at each location in the liver, the histotripsy array was pulsed to generate cavitation 20 times during the expiratory pause of the breath cycle at a repetition rate of 1 kHz. Signal was received on all array elements for a period spanning 230 to 500 μs following pulse transmission to exclude the earlier-arriving nucleation signal and include the later-arriving collapse signal, the timing of which can vary depending on

focal pressure amplitude. Prior to acquiring the collapse signals for correction, the array pulsed and received 20 times using the same parameters to automatically set the receive system gain.

The pulsing rate of 1 kHz minimizes the impact of tissue motion and permits effective pulse-to-pulse subtraction of tissue reflection signals. However, at high pulsing rate, the collapse also has consistent timing from pulse to pulse and is thus also removed by subtraction. To preserve collapse signals after subtraction, we take advantage of the dependence of the collapse timing on focal pressure amplitude [202], [203]. The focal pressure amplitude was alternated for every other pulse by 15%. As a result, the collapse timing varied by a fixed duration (~30 μs) from pulse to pulse, while tissue reflection timings were approximately constant. Before subtraction, the amplitude of each signal was normalized to the integral of the signal envelope summed over all elements, as in

$$s_{A-B,e}[t_i] = \frac{s_{A,e}[t_i]}{\sum_{e_j=1}^{N_e}\sum_{t_i=1}^{N_t}\left|\varphi_{S_{A,e_j}}[t_i]\right|} - \frac{s_{B,e}[t_i]}{\sum_{e_j=1}^{N_e}\sum_{t_i=1}^{N_t}\left|\varphi_{S_{B,e_j}}[t_i]\right|} \qquad (5.1)$$

where $s_{A,e}[t_i]$ is the signal from pulse A on element e sampled at time indices t_i, $\varphi_{S_{A,e}}[t_i]$ is the discrete-time Hilbert transform of $s_{A,e}[t_i]$, N_t is the number of time indices, and N_e is the number of array elements. The subtraction in equation 5.1 reduced tissue clutter while preserving collapse signals, as shown in Figure 5.2 (a)-(c).

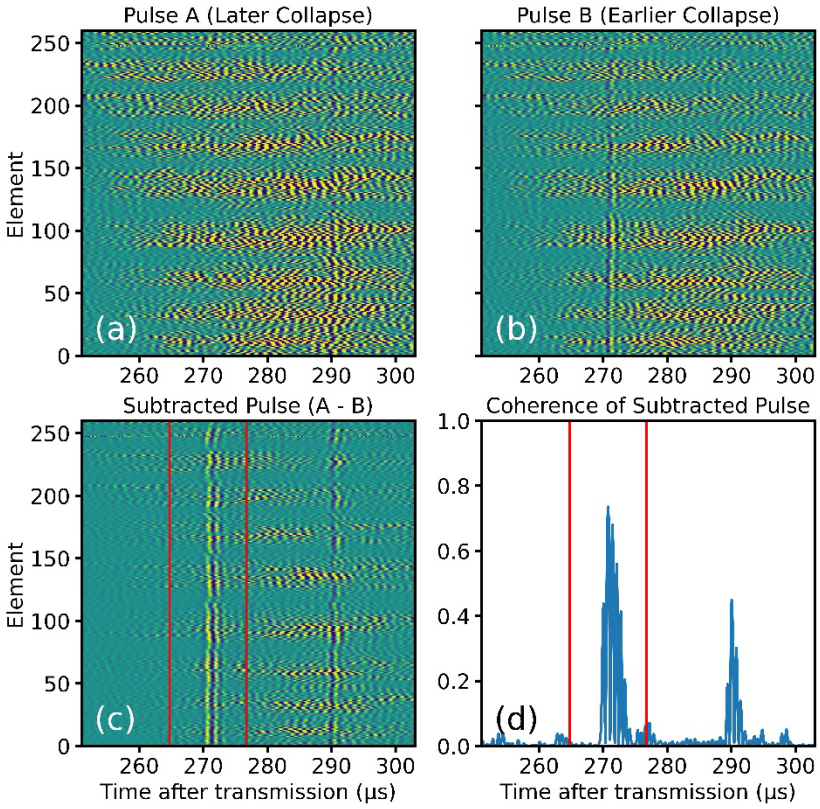


Figure 5. 2. (a), (b) Signals received on all array elements after pulse A (a) and subsequent pulse B (b). (c) Subtraction of pulse B from pulse A. (d) The coherence factor $C[t_i]$ calculated at every timepoint of the subtracted signal in (c).

5.2.2.2 Step 2: Use phase coherence to detect the collapse signal in the presence of tissue reflection clutter

The pulse-to-pulse subtraction in (1) reduces tissue reflections but leaves residual clutter of similar amplitude to the collapse signal. Therefore, the signal from collapse was automatically detected by using phase coherence instead of amplitude information. In ultrasound imaging, the phase coherence factor has been used to improve contrast in high-clutter signal environments like the abdomen [204]–[207]. Here, we apply the coherence factor introduced by Mallart and Fink for ultrasound imaging and recently used by Thomas et al. for *in vivo* AC of boiling histotripsy [102], [106]. The coherence factor C is computed at every time index t_i and is given by

$$C[t_i] = \frac{(\sum_{e_j=1}^{N_e} s_{e_j}[t_i])^2}{N_e\left(\sum_{e_j=1}^{N_e} {s_{e_j}}^2[t_i]\right)} \qquad (5.2)$$

where $s_{e_j}[t_i]$ is the subtracted signal for element e_j obtained from (1) and N_e is the total number of array elements. The coherence factor $C[t_i]$ varies between 0 and 1 designating low and high phase coherence, respectively. As a point-like source near the focus, the collapse shockwave has significantly higher spatial coherence than the tissue reflections arriving from beyond the focus. Thus, the collapse time t_c was defined as the time index of maximal coherence ($t_c = \mathrm{argmax}_{t_i}(C[t_i])$). The subtracted collapse signal was truncated by setting a 12-µs time window centered at t_c as illustrated in Figure 5.2 (c) and (d).

5.2.2.3 Step 3: Use the singular value decomposition (SVD) to retrieve the optimal phase correction in the presence of tissue clutter

In our previous *in vitro* study, element-to-element phase differences were measured via cross correlation of each element's collapse signal to a reference signal (which was set as the collapse signal with maximum peak-to-peak amplitude). *In vivo*, however, signal clutter degrades the spatial coherence of the collapse signal, decreasing the covariance of signals from spatially distant array elements and limiting the accuracy of the cross correlation. To accurately determine the phase differences in the presence of signal clutter, we use the singular value decomposition, similarly to the decomposition of the time reversal operator (DORT) technique introduced by Prada and Fink [10], [208], [209]. Unlike DORT, which operates in the frequency domain, here the SVD is applied directly in the time domain to separate the collapse signal from

overlying tissue clutter and return an optimal phase correction *in vivo*. This time domain analysis is convenient due to the narrow bandwidth of the histotripsy transducer. We define a complex-valued matrix R where each row is the subtracted, time-windowed received signal from each array element. The SVD decomposes R into orthogonal components such that R can be written as a sum of products of orthonormal vectors:

$$R = U\Sigma V^* = \sigma_1 \boldsymbol{u_1} \boldsymbol{v_1^*} + \sigma_2 \boldsymbol{u_2} \boldsymbol{v_2^*} + \ldots + \sigma_{N_e} \boldsymbol{u_{N_e}} \boldsymbol{v_{N_e}^*} \qquad (5.3)$$

Here the notation * denotes the conjugate transpose. The columns of the matrix U are orthonormal vectors $\boldsymbol{u_i}$ (left singular vectors) of length N_e that represent orthogonal components of the signal in the element domain. The columns of the matrix V are orthonormal vectors $\boldsymbol{v_i}$ (right singular vectors) of length N_t that represent orthogonal components of the signal in the time domain. Intuitively, each vector $\boldsymbol{v_i}$ can be thought of as a time-domain signal component that is modulated with a different phase and amplitude for each element by the vector $\boldsymbol{u_i}$. The real-valued, non-negative scalars $\sigma_1, \sigma_2, \ldots, \sigma_{N_e}$ (singular values) descend in order of magnitude along the diagonal matrix Σ and represent the relative contribution of each orthogonal signal component to the total signal energy.

The signal from a single, well resolved point source is constant across elements except for a phase and amplitude factor from aberration. Therefore, a point-like source is fully represented by one orthogonal component of the decomposed signal. Prada and Fink showed that the strongest point-like scatterer in the received signal forms the first eigenvector of the element-to-element covariance matrix, RR^*, which is also the first singular vector of R in the element domain [208]. In our subtracted, time-windowed data R, the collapse shockwave is the only point-like scatterer. Therefore, the first singular vector $\boldsymbol{u_1}$ contains the element-to-

element phase and amplitude differences of the collapse signal, without interference from tissue clutter. According to the principle of time reversal, the conjugate vector $\boldsymbol{u_1^*}$ contains the phase correction that maximizes coherence at the origin of the collapse shockwave (nominally the focus) [7]. Selective extraction and alignment of the collapse signal using the SVD are illustrated in Figure 5.3.

We obtain an aberration correction vector $\boldsymbol{u_1^*}$ for each of the 10 subtracted, time-windowed received data sets R. The phases of $\boldsymbol{u_1^*}$ are relative values in the range $-\pi$ to π. Occasionally, the phases were arbitrarily mapped across the discontinuity between π and -π. The resulting phase jumps were removed by adding $\pm 2\pi$ to counteract deviations exceeding $\mp\pi$ from the median phase value. Phase values were then converted to time delays for aberration correction.

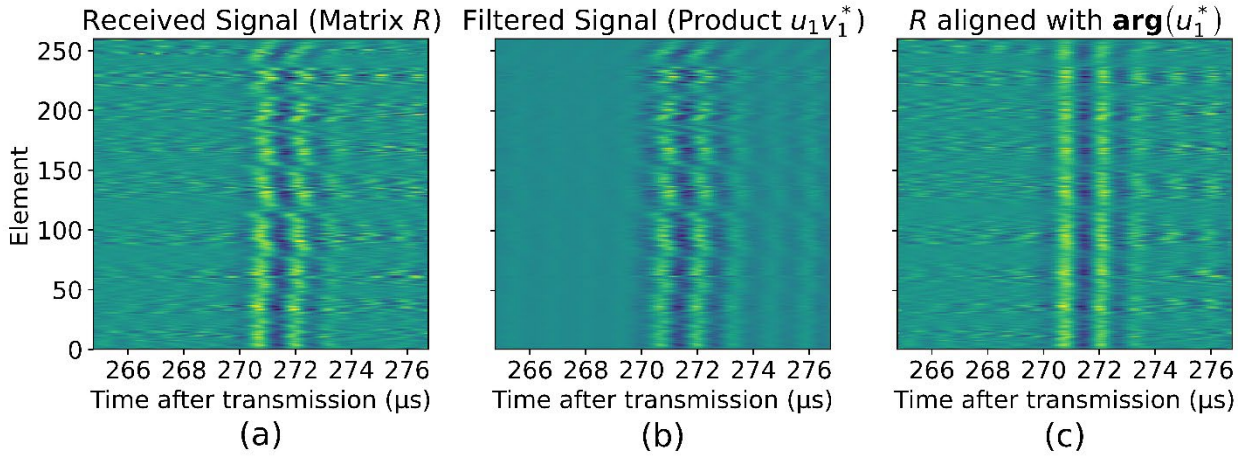


Figure 5. 3. (a) The subtracted, time-windowed receive data matrix R containing a collapse shockwave signal and overlying clutter. (b) The product $\boldsymbol{u_1 v_1^*}$, which contains only the signal component from collapse. (c) Alignment of R using the phase component of $\boldsymbol{u_1^*}$**.** Plots show the real part of signals with arbitrary intensity units on a linear scale.

5.2.2.4 Step 4: Refine the correction delays by taking the median across multiple delay sets

The per-element median was computed across the delay sets from step 3 to produce a final, robust correction. The median removes small pulse-to-pulse differences from random errors and minor spatial variations in the origin of the collapse while preserving the arrival time differences from aberration [201]. Occasionally, delay sets were obtained from pulses where (1) no cavitation (and thus no collapse) occurred or (2) the collapse shockwaves originated less than one wavelength from a strong tissue reflector (*e.g.* a bile duct) and could not be resolved by the SVD. These delay sets were automatically detected and removed before taking the median using the following procedures. Case (1) was detected if $\sigma_1 < 2\sigma_2$, because the collapse signal (a point-like source) has significantly larger singular values than speckle [208]. Case (2) typically produces delay sets with large errors and was therefore detected if >5% of elements had time delays deviating by more than one acoustic cycle (1.33 µs) from the median time delay for the set. On average, 3 of 10 total delay sets were removed (maximum removed: 6 sets). After removing these sets, the median time delay per element was applied in transmission for aberration correction.

Cavitation-based aberration correction was performed at 5 – 7 locations in the liver of each subject, with an average minimum separation of 1.7 cm, average depth below the skin of 6.0 cm (range: 3.9 – 8.6 cm), and varying obstruction by ribs. For each liver location, collapse signals were generated for correction using the lowest effective power setting. Due to varying levels of attenuation throughout the liver, the power was set by incrementally increasing the array output and repeating the acquisition (step 1 of the collapse-based AC procedure) until collapse signals could be detected. After the power was set, a correction delay set could be obtained using steps 1 - 4. Step 1 (collapse signal acquisition and data transfer) required ~1 s.

Signal processing (steps 2 – 4) required an additional 1.1 s, for a total data collection and processing time of ~2 s per correction.

5.2.3 Evaluation of Aberration Correction Efficacy

The efficacy of the collapse-based aberration correction *in vivo* was evaluated by comparing the array output power required to generate cavitation with and without correction. Cavitation probability curves were produced by ramping the output amplitude while tracking the fraction of pulses generating cavitation following the method used by Maxwell et al [58]. At each location in each pig liver, a correction was acquired as in section 5.2.2. Then, the electrical power setting of the array driver was increased from 4 mJ/pulse to 960 mJ/pulse in 15 steps. At each power setting, the histotripsy array was pulsed 25 times at 2 Hz and set to receive signals from 50 to 230 μs after transmission, capturing reflections off the skin surface and the nucleation signal. Signals obtained during active inhalation or exhalation were detected and discarded to remove confounding error from motion by taking the SVD of the signals from all pulses for one element (a 25 × N_t matrix) and thresholding the magnitude of the first eigenvector, which represents low-frequency oscillations from respiration. For each remaining signal, cavitation was detected by passively mapping the received signal energy over a 3-D volume centered at the focus (transverse extent: 5 mm, axial dimension: 12 mm, discretization: 0.5 mm) with the Time Exposure Acoustics Passive Acoustic Mapping algorithm (TEA-PAM) assuming a speed of sound of 1540 m s^{-1} [210]. Cavitation emissions strongly increased the mapped energy and could therefore be detected by applying a user-defined threshold to the energy integrated over the 3-D volume. Pulses where cavitation was detected were counted to compute a probability of cavitation at each transducer power level. This process was repeated

with and without aberration correction to produce probability curves as shown for one location in one pig liver in Figure 5.4. The pressure values along the horizontal axis represent the peak rarefactional pressure amplitude produced by the histotripsy array in the free field at each tested power setting. These pressure amplitudes were estimated by measuring output from the array at subthreshold pressures (<25 MPa) as a function of electrical input power in the free field and extrapolating via a polynomial fit [66]. (The output from the full array could not be measured directly at amplitudes generating cavitation). Then, pressure values were de-rated to account for depth-dependent absorption in tissue using

$$A_{derated} = Ae^{-\alpha_a d_a + \alpha_l d_l} \quad (5.4),$$

where A is the estimated focal pressure before derating, d_a is the thickness of the abdominal wall, d_l is the depth in liver beyond the abdominal wall, and α_a and α_l are the attenuation coefficient of the abdominal wall (1.0 dB cm^{-1}) and the liver (0.27 dB cm^{-1}) at 750 kHz [211]. Sigmoid curves were numerically fit to the probability measurements to determine the power required to reach 50% cavitation probability (the "cavitation threshold" [58]) both with and without AC.

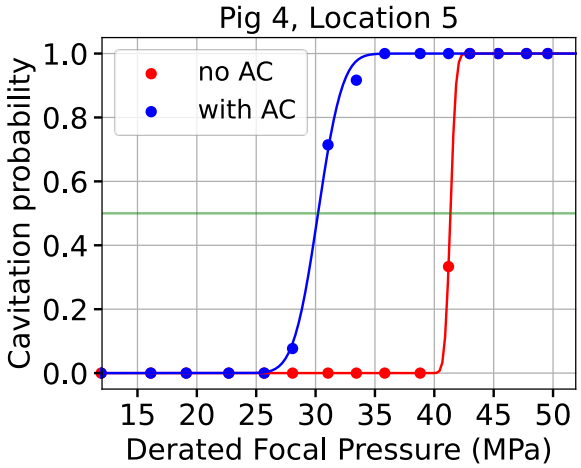


Figure 5. 4. Example cavitation probabilities and fitted curves with (blue) and without (red) aberration correction as a function of free-field equivalent focal pressure for one location in the liver of one pig. The green horizontal line marks 50% cavitation probability (the threshold).

5.3 Results

The ACE AC procedure reduced the array output amplitude required to generate cavitation at all liver locations in all subjects. The required amplitude was converted to an estimated focal pressure as described in 5.2.3 and is shown for each location both with and without aberration correction in Figure 5.5 (a). The pressure values represent the (de-rated) rarefactional pressure amplitude that would be produced at the focus in the free field using the power setting required to reach the threshold for 50% probability of cavitation in vivo. Across all subjects and locations, aberration correction reduced the equivalent free-field focal pressure from 32.0 MPa to 27.5 MPa on average, approaching the nominal rarefactional pressure amplitude for inertial cavitation generation in liver with a single pulse (24.8 MPa) [7]. Without aberration or frequency-dependent attenuation, the focal pressure required to generate cavitation would be the same across all locations (the standard deviation of the required output amplitude would be 0). Here, ACE AC decreased the standard deviation of the required pressure across subjects and locations from ±5.2 MPa to ±2.3 MPa, suggesting that the correction reduced the variation due to aberration.

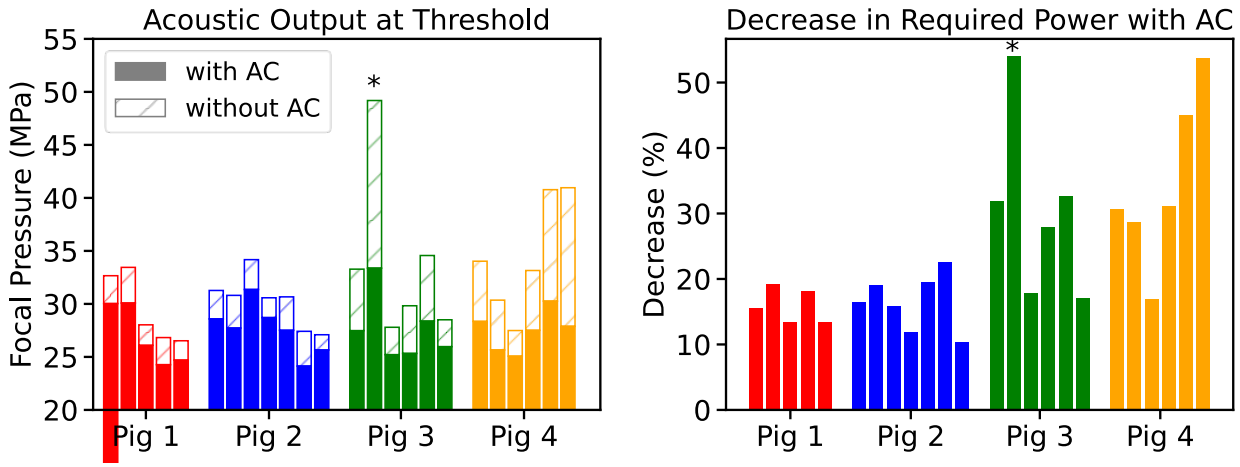


Figure 5. 5. (a) Estimated acoustic output from the histotripsy array at the cavitation threshold (50% probability of generating cavitation with a single pulse) for all liver locations in all subjects both with (solid bars) and without (hashed bars) aberration correction. The pressure values represent the peak rarefactional focal pressure amplitude that would be generated at the array focus in the free field at the array power setting required to reach the cavitation threshold in vivo. Pressure amplitudes are de-rated to account for depth-dependent absorption by tissue as described in Section 5.2.3. (b) The percent reduction in acoustic power required to reach the cavitation threshold after aberration correction. *At location 2 in pig 3, cavitation could not be generated at any power setting without aberration correction. The power reduction was estimated by setting the threshold without correction to the de-rated focal pressure at maximum array output.

On average, ACE AC reduced the acoustic power required to generate cavitation in the porcine liver by 24% (range: 10 to 54%). The percent reduction in required power is shown for all locations and subjects in Figure 5.5 (b). Power reduction varied considerably by subject and by location in the liver. The maximum range in power reduction for a single subject was from 17% to 54% (pig 4). Also, pigs 3 and 4 had higher average power reductions (30 and 34%, respectively) than pigs 1 and 2 (17% and 16%, respectively). Higher average power reductions may have resulted from deeper targets in pigs 3 and 4, which together had more locations ≥6 cm below the skin (8 of 12 locations) than pigs 1 and 2 (3 of 12 locations).

The spatial origin of each received collapse signal was estimated by passively mapping the signal energy over a 3-D grid as described in Section 5.2.3 and identifying the grid point of maximum energy. (The mapped locations are relative to the location of the aberrated focus,

which is shifted from the array geometric focus due to refraction). The average deviation of the collapse signal origin from the aberrated focus is shown for each location and subject in Figure 5.6. Across all subjects and locations, the collapse signal origin deviated from the aberrated focus by 1.3 ± 0.7 mm (mean ± standard deviation). The maximum distance was 2.9 mm from the center of the focus. Most of the deviation was along the axial direction and towards the transducer (1.1 ± 0.8 mm). The average spatial deviation of the collapse signal varied across locations in the liver (by up to 2.3 mm for a single subject). The average spatial deviation did not vary substantially across subjects.

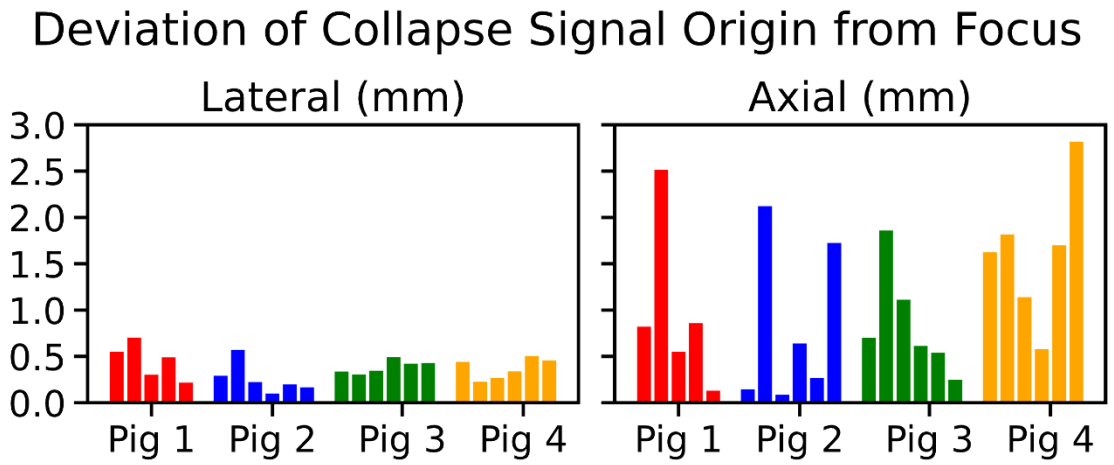


Figure 5. 6. Average spatial deviation of the collapse signal origin from the focus at each liver location. Plotted bars indicate the spatial deviation in the lateral (a) and axial (b) directions, respectively.

Variance across the correction delay estimates was reduced by taking the median per-element delay from multiple collapse signals. This effect is illustrated by Figure 5.7, which plots the average absolute difference between the delay set obtained from the median of 10 collapse signals (i.e., from 10 subtracted pulse pairs) and the delay sets obtained from the median of fewer collapse signals for different subjects and locations. The average difference between delay sets is defined as $\frac{1}{N_e}\sum_{e=1}^{N_e}\left|\tau_{e,10} - \tau_{e,m}\right|$, where $\tau_{e,m}$ is the relative delay in acoustic cycles

at the central frequency (750 kHz) detected by transducer element e after taking the median of m collapse signals. Prior to calculating the difference, the spatial deviation of each collapse signal from the focus was estimated with TEA-PAM and subtracted from the delay estimates to isolate the component from aberration. On average, the delay estimates from one collapse signal deviated from the 10-signal median by ~0.07 acoustic cycles. Increasing the number of collapse signals to 5 lowered the mean difference to ~0.02 cycles. Beyond 5 collapse signals, the mean difference decreased more slowly (to ~0.01 cycles using the median of 9 collapse signals).

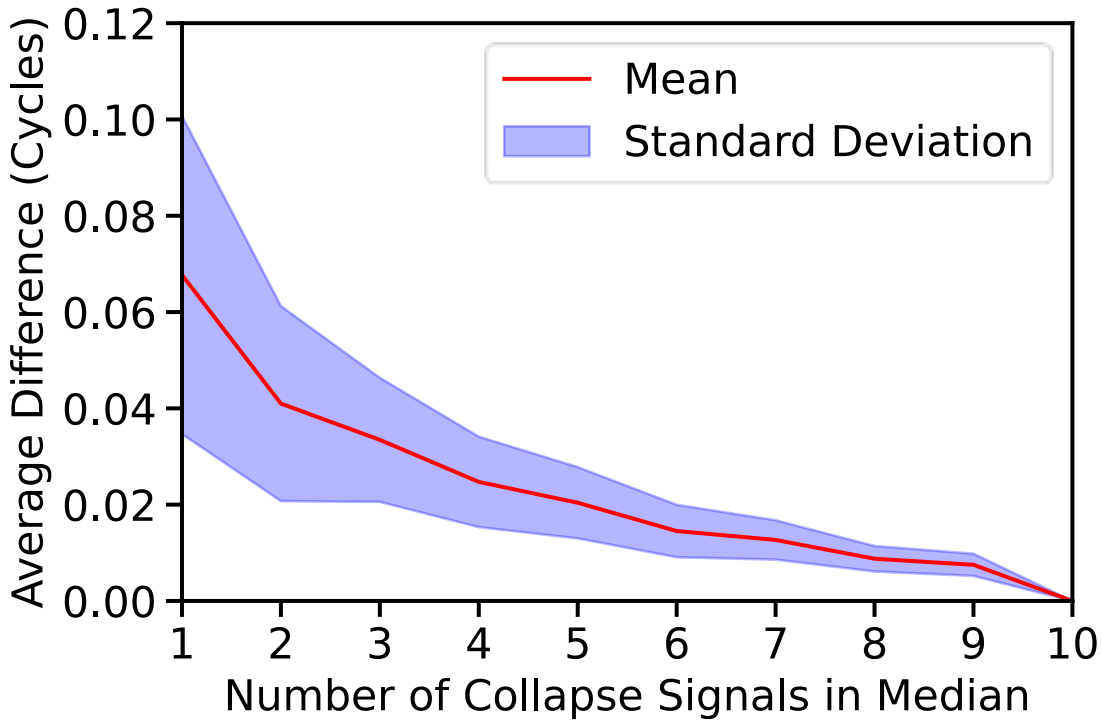


Figure 5. 7. The average difference between the final correction delay set (computed from the median over 10 collapse signals) and delay sets computed from the median of fewer collapse signals in numbers of acoustic cycles at the central frequency (750 kHz). The red line denotes the mean over locations. The blue area denotes the standard deviation.

5.4 Discussion

Cavitation-based aberration correction substantially reduces the acoustic power required to perform transabdominal histotripsy *in vivo*. Here, aberration correction reduced the power required to generate cavitation in the porcine liver by 24%, on average (range: 10 – 54%). These findings agree well with the range of power reductions observed by Thomas et al in the porcine liver using speckle-based aberration correction with boiling histotripsy (15 – 45%) [106]. At 2 of the liver locations tested in this study, the power reduction from collapse-based AC exceeded 45%. These results suggest that cavitation-based aberration correction could decrease the energy delivered to intervening tissues to reduce the risk of heating or any off-target damage and thereby improve the safety of transabdominal histotripsy treatments. Additionally, cavitation-based AC could improve the efficacy of histotripsy ablation at target locations where aberration limits the size of the bubble cloud (and thus the lesion size). Collapse emissions from a small cloud could be used to correct aberration and increase the focal pressure amplitude to generate a larger, more robust cavitation cloud capable of rapid ablation [60]. Cavitation-based aberration correction could therefore enable safer, more effective transabdominal histotripsy treatments.

The cavitation-based aberration correction procedure was robust despite acoustic signal clutter and tissue motion *in vivo*. The correction procedure successfully reduced the array output pressure required to generate cavitation at all locations tested. Variation in the required output pressure after cavitation-based AC likely resulted in large part from absorption losses not accounted for by the de-rating calculation in (4) (*e.g.*, varying absorption by ribs). Collapse signals from different cavitation clouds at the same location yielded similar phase estimates (see Fig. 5.7). As a result, the median delay over multiple collapse signals tends to converge

towards one value, suggesting that the estimated delays approach the true aberration delays. These observations indicate that the cavitation-based method could provide robust and reliable aberration correction for transabdominal histotripsy therapy.

Cavitation-based aberration correction was performed relatively quickly, requiring ~2 s for signal acquisition and processing. Due to its speed, the cavitation-based method could be used to perform correction at multiple locations without substantially extending the total treatment time. Ablation of a tissue volume requires re-focusing the beam to generate cavitation at multiple discrete locations. For large ablation targets like liver tumors, treatment of the entire volume can require hundreds of discrete re-focusing locations [212]. If the tumor volume exceeds the size of the isoplanatic patch (region where a given phase correction can be applied without loss of efficacy), the correction will need to be repeated at multiple locations. The isoplanatic patch size is unknown for transabdominal histotripsy but has been reported to be smaller than a 5-mm diameter for transabdominal ultrasound imaging [213]. At this patch size, a liver tumor of 3-cm diameter would require ~30 discrete corrections. With the collapse-based procedure, all corrections could be computed in a total of 1 minute before initiating treatment. Alternatively, collapse emissions from cavitation clouds at adjacent locations could potentially be used to adjust the correction dynamically during therapy as the beam focus is scanned through space, thereby minimizing the additional time required for multi-location correction. Unlike collapse-based AC, speckle-based AC relies on iterative estimation, requiring ~1 minute per correction in vivo. Therefore, for 30 discrete locations, speckle-based AC would require ~30 min total, unacceptably prolonging the treatment time.

One significant disadvantage of ACE AC is the requirement for sufficient focal pressure amplitude to generate cavitation signals for correction. In this study, cavitation was generated for correction at all locations at pressures below the threshold for cavitation generation with a single pulse by repeating pulses at high rates (1 kHz). However, the pigs had relatively thin abdominal walls (~3 cm). A thicker (human) abdominal wall could cause greater attenuation and thereby prevent the generation of cavitation for correction, especially at deep-seated or heavily obstructed targets. In these cases, speckle-based AC could be used first to restore sufficient focal pressure to generate cavitation. Then, the correction could be updated throughout treatment or at adjacent locations by using cavitation-based AC as described above.

Another disadvantage is that cavitation-based AC can potentially damage non-target tissue if the focus is shifted from the target due to refraction. Therefore, cavitation-based AC would ideally be preceded by a focal shift correction procedure. Such a 2-step correction approach has been demonstrated for transcranial histotripsy applications [84]. It is also important to note that cavitation-based correction can displace the corrected focus from its pre-correction location. Collapse signals often originate a few millimeters away from the focus (by an estimated 1.3 mm, on average, in this study). Consequently, the resulting correction delays can steer the beam focus away from its location before correction [201]. Most of the estimated deviation (1.1 mm) was consistently along the axial direction and towards the transducer. This deviation is modest compared to the axial extent of the focus (full-width at half maximum, 4.5 mm) for the histotripsy array used here [147]. Furthermore, in clinical trials, liver tumors were ablated with an extended margin of >5 mm [75]. Therefore, a margin of 2 mm could likely be added to the planned ablation zone to compensate for pre-focal displacement of the bubble

cloud without significantly altering treatment outcomes. Alternatively, to prevent bubble cloud displacement, the spatial deviation component could potentially be estimated and removed from the correction delays using passive acoustic mapping (e.g., TEA-PAM). Passive acoustic mapping uses travel time differences to estimate the location of an acoustic source relative to the focus. The travel time differences resulting from this deviation could be removed from the correction delays to prevent cavitation-based AC from displacing the bubble cloud.

Finally, to isolate the effects of aberration, it was necessary to acquire the correction and evaluate its performance at the same point in the breath cycle (the expiratory pause). This period was sufficiently long to allow the delivery of ~10 pulses at low (2 Hz) repetition rate without substantial motion of the tissue. At this rate, cavitation probability curves could be measured for one location within ~10 min. Evaluation of the correction performance during active inhalation and exhalation would have required samples from many more breath cycles and was not possible in this study due to experimental time constraints. Future work will assess whether a single correction (acquired at one point in the breath cycle) is effective throughout the entire breath cycle or whether the correction should be updated dynamically to compensate for tissue deformation during respiration.

5.5 Conclusion

This study presents an aberration correction procedure for transabdominal histotripsy based on receiving the emissions from cavitation cloud collapse and demonstrates its efficacy *in vivo*. The procedure is robust in the presence of abdominal signal clutter and motion. In the porcine liver, the cavitation-based aberration correction reduced the acoustic power required

to generate cavitation for histotripsy therapy by 24%, on average. This result suggests that cavitation-based aberration correction could substantially decrease the energy delivered to non-target tissues during treatment to improve the safety and efficiency of transabdominal histotripsy therapy.

Chapter 6

Summary and Future Work

This chapter summarizes the contributions of this Dissertation to the investigation of phase aberration effects and the development of aberration correction methods in transabdominal histotripsy therapy. The chapter also discusses remaining challenges to aberration correction in transabdominal histotripsy and potential methods to address these challenges. Finally, the chapter outlines future studies that could advance the clinical implementation of aberration correction in histotripsy and concludes the Dissertation with some final remarks.

6.1 Summary

The clinical translation of abdominal histotripsy has advanced significantly without aberration correction. Unlike other therapeutic ultrasound techniques, histotripsy has features like a short pulse duration and a threshold mechanism that enable precise ablation without

collateral damage in the presence of strong aberrations (see Section 1.2). Notably, histotripsy has been demonstrated to be safe and effective in clinical trials and recently received FDA clearance for the treatment of liver tumors. These outcomes indicate that tumors in acoustically accessible locations like those treated in current clinical trials can be effectively ablated without aberration correction. However, as histotripsy begins to treat tumors in more challenging locations, including deep-seated tumors and those heavily obstructed by ribs or air pockets, aberration can combine with frequency-dependent attenuation and reflection to severely decrease the peak pressure amplitude and divert energy from the focus to intervening tissues, critically limiting the efficacy and safety of histotripsy therapy. Therefore, the ultimate consequence of aberration is to restrict the number of patients who can receive histotripsy treatment. It will thus be critical to understand the effects of aberration and develop methods for correction as histotripsy rapidly approaches widespread clinical adoption and expands into other therapeutic applications in the abdomen, namely in the kidney and pancreas.

Towards these aims, this Dissertation investigated the effects of aberration and developed methods to correct aberration in abdominal histotripsy. The first part of the Dissertation quantitatively assessed the effect of human abdominal tissues on focusing quality. Specifically, a computational model was designed and validated to simulate a large aperture, low f-number histotripsy transducer focusing through the human abdomen (see Chapter 2). The simulations show that abdominal phase aberration can substantially reduce targeting accuracy and peak pressure amplitude of the histotripsy focus despite low therapeutic frequency. Importantly, the results indicate that aberration correction could restore substantial focal pressure amplitude and thereby expand the treatment envelope in the liver for the average human patient by 50%

(see Chapter 3). This finding suggests that aberration correction using a phased array with a reasonable number of elements could enable the treatment of more patients with histotripsy.

To increase focal pressure amplitude and focusing efficiency for transabdominal histotripsy, the second part of the Dissertation developed and tested an aberration correction method based on receiving the acoustic emission from cavitation cloud collapse. The method takes advantage of the high spatial coherence and deterministic phase of the collapse signal, which approximates a point source. Due to these properties, phase correction with the collapse signal was shown to effectively maximize the focal pressure amplitude through abdominal tissues *in vitro* (see Chapter 4). Challenges to implementing the collapse-based aberration correction *in vivo* were addressed in Chapter 5. Specifically, the collapse signal has relatively low amplitude (<100 kPa [201]) and is therefore obscured by higher amplitude reflections of the therapy pulse off tissue. Removal of this tissue reflection clutter is complicated by the narrow bandwidth of the histotripsy array and by respiratory motion. Therefore, Chapter 5 developed signal processing methods that isolate the collapse signal from abdominal signal clutter to obtain an optimal phase correction *in vivo*. Experiments in live pigs show that collapse-based AC substantially reduces the acoustic power required to perform histotripsy in the liver. All collapse-based correction techniques were demonstrated with a 260-element phased array of similar dimensions to the current clinical histotripsy device, suggesting that clinical implementation of collapse-based aberration correction is feasible and could substantially increase focusing quality to improve the efficacy, efficiency, and safety of transabdominal histotripsy treatments.

6.2 Outlook and Future Work

Achieving optimal focusing in transabdominal histotripsy will require further studies and additional aberration correction methods beyond those presented here. Like other signal-based methods, collapse-based aberration correction can recover substantial focal pressure amplitude but cannot correct focal shift. Therefore, to prevent off-target cavitation, collapse-based aberration correction and subsequent therapy would ideally be preceded by a targeting correction procedure. Lu et al demonstrated such a 2-step approach for transcranial histotripsy aberration correction, where the first step used an a priori CT scan of the skull as input to a ray tracing model to correct focal shift, and the second step used collapse-based AC to restore substantial focal pressure amplitude at the corrected focus location [84].

For transabdominal histotripsy, the first step (modeling-based aberration correction) has additional challenges. Unlike the rigid skull bone, which can be repeatably registered to a pre-operative image, soft tissues readily shift and deform, thereby altering the tissue path and invalidating the phase estimates obtained from the numerical model. Therefore, a model-based AC procedure for transabdominal histotripsy would ideally image at the time of treatment (the point-of-care) and rapidly compute the phase correction with a fast numerical propagation model (e.g., ray tracing). For soft tissue, focal point correction requires only a low-resolution map of the tissue acoustic properties [143]. Therefore, point-of-care modalities like cone beam CT [198] or 3D ultrasound imaging [214], [215] may be sufficient. Moreover, the findings of Chapter 2 indicate that a large portion of the focal shift results from refraction at the interface between tissue and the coupling water bath [193]. Therefore, it may be possible to correct most of the focal shift by simply mapping the tissue surface with the histotripsy array in pulse-

echo mode and using rays to model refraction at the water-tissue interface. This surface-mapping approach does not require additional imaging modalities or image segmentation and could therefore be faster than other modelling-based AC techniques. The feasibility and accuracy of this technique will be evaluated in future work.

Another significant challenge to model-based aberration correction in the abdomen is tissue motion from respiration and cardiac activity. Respiratory and cardiac motion cyclically alter the location of the target tissue with respect to the therapy array and the conformation of the tissue layers in the beam path. The target displacement can be compensated by tracking tissue motion and appropriately adjusting the array position with a mechanical positioner [216]. The changes in layer conformation, however, slightly alter the refracted beam path and therefore cause the magnitude of the focal shift to fluctuate. These fluctuations should be measured in future studies. If the fluctuations cause significant targeting error, then the model-based correction will need to be pre-computed for the entire respiratory cycle or updated in real time, increasing the requirements for computational efficiency.

One alternative to model-based AC for targeting correction could be to visualize the histotripsy beam focus in tissue by synchronizing subtherapeutic emissions from the therapy transducer with passive signal acquisition by the coaxial ultrasound imager [194], [195]. The emission from the therapy transducer is reflected by scatterers in the focal region, creating an image of the therapy focus which can be overlayed on a standard B-mode image of the tissue. Using this visual feedback, the operator can reposition the focus onto the tissue target. This focus imaging approach avoids errors from modelling, including from image segmentation, assignment of acoustic properties, and inaccuracies of the acoustic propagation model [146].

Also, this approach has similar computational complexity to B-mode imaging and could therefore be faster than modelling-based focal point correction [197]. However, the ability to visualize the focus may be limited in highly absorbing or heterogeneous tissues. Intervening ribs can strongly attenuate backscattered signals and thereby compromise imaging of the histotripsy focus and surrounding tissue. Furthermore, highly heterogeneous tissues with spatially varying echogenicity (e.g., the liver) can cause some regions of the focus to appear brighter than others, hindering focus visualization [196]. Strategies to improve histotripsy focus imaging in highly obstructive or heterogeneous tissues could be developed in future work.

After focal point correction in the first step, the second step of 2-step AC could increase focal pressure amplitude using either collapse-based AC or speckle-based AC (see Section 1.3). As discussed in previous sections (Sections 1.3, 4.4, and 5.4), collapse-based AC has important advantages over speckle-based AC when multiple corrections are needed (e.g., at different points in space or updates over time). Collapse signals approximate a point source and thus permit accurate phase correction without iteration [1]. Therefore, collapse-based AC can be very fast, here requiring ~1 s per correction in vivo (see Chapter 5). Furthermore, collapse emissions can be received from the cavitation clouds generated during therapy without additional pulse sequences, thereby minimizing the time required for aberration correction. Speckle signals, on the other hand, have stochastic phase and thus require statistical estimation techniques to extract the aberration delays. The iterative estimation technique by Thomas et al required ~1 min per correction to converge in vivo [106]. This correction time is acceptable if only a few corrections are needed (e.g., at only a few locations) but may become unacceptable

if many corrections are required (e.g., to re-focus the beam at multiple locations within a large tumor).

A disadvantage of collapse-based AC is the requirement for sufficient pressure amplitude to generate cavitation signals for correction. For therapy targets with substantial insertion loss from absorption and aberration (e.g., deep or rib-obstructed targets), the histotripsy array may not have sufficient power to reach the intrinsic threshold amplitude for generating cavitation at the focus. The histotripsy array simulated in Chapter 3 could only reach the intrinsic threshold amplitude in ~50% of the liver without aberration correction. Aberration correction increased this portion to ~75%. For these targets, cavitation could potentially be generated at focal pressure amplitudes below the intrinsic threshold by pulsing at high repetition rates (>20 kHz) over extended periods (~100 s) [217]. However, this approach may unacceptably increase correction times and potentially elevate the risk for pre-focal cavitation. Alternatively, speckle-based aberration correction could be used. It may be possible to reduce the time required for speckle-based AC by adapting a technique introduced by Bendjador et al. for aberration correction in transabdominal ultrasound imaging [10]. Instead of using iterative estimation, Bendjador et al. estimated the aberration delays by beamforming the images resulting from plane waves transmitted at varying angles and thereby obtaining multiple independent measurements of the speckle phase. The deterministic component of the speckle phase was extracted from the set of independent beamformed images via a singular value decomposition, which returns the aberration delays in the transmit angle domain. This technique could potentially be adapted to histotripsy AC by grouping the therapy array elements into individually transmitting clusters, each of which has a unique elevational and azimuthal angle

relative to the focus and can therefore produce an independent speckle signal. Also, in histotripsy, aberration correction is only required at the therapy focus (not throughout the entire image) and could potentially be performed directly in the time domain (without beamforming). One challenge to address in future work is selecting the size of the beamformed region around the histotripsy focus (or in the time domain, the length of the time window) used for phase estimation. According to Bendjador et al., the signals used for phase estimation should originate from a spatial region smaller than the isoplanatic patch (area in which the aberration delays are approximately constant). Otherwise, the aberration delays would vary over the region and hinder the estimation. However, the region should be sufficiently large (i.e., have enough independent pixels or time samples) to distinguish the underlying image (deterministic component of the phase) from stochastic, angle-dependent phase components using the SVD. This parameter must be determined experimentally. A related challenge is that the large acoustic wavelengths typical of histotripsy may limit the number of independent samples that can be obtained in a region restricted by the isoplanatic patch size. Therefore, it may be necessary to receive harmonic frequencies generated at the focus to decrease the wavelength and thereby increase the number of independent samples within the isoplanatic region [218]. The feasibility of non-iterative speckle-based aberration correction will be investigated in future work.

Ideally, speckle-based aberration correction (iterative or otherwise) would be used first to restore sufficient focal pressure amplitude to generate cavitation and then be followed by collapse-based AC to refine or update the correction as the treatment progresses or as the focus changes location. Speckle-based AC alone would either (1) extend the treatment time

(using the iterative estimation approach) or (2) estimate the aberration delay by element cluster instead of by individual element (using the SVD estimation approach). Collapse-based AC accurately determines the aberration delay for each element with relatively few therapy emissions and could therefore refine a coarse estimation of the aberration delays or update an initial estimate of the aberration delays throughout treatment without significantly extending the total procedure time.

Beyond researching additional methods for aberration correction, future studies are needed to determine how frequently aberration correction should be performed throughout treatment. The spatial frequency at which aberration correction should be repeated is determined by the isoplanatic patch, the volumetric region over which the estimated phase correction can be applied without loss of focusing quality [219]. Specifically, the isoplanatic patch dictates the number of locations requiring phase correction within a given tissue volume. The size of the isoplanatic patch depends on the heterogeneity of the tissue path, the transducer geometry, and the acoustic frequency. For a 3-MHz, small 2-D aperture (48 × 48 mm^2) array, the isoplanatic patch through human abdominal wall was estimated to be between 2.5 - 4 mm, implying that a given phase correction would have decreased efficacy if applied more than a few millimeters from the location of phase estimation [213]. Similar measurements are needed for the large apertures and low frequencies used for histotripsy. These values will help determine the spatial frequency required for aberration correction in transabdominal histotripsy.

Another factor affecting the number of required corrections during treatment is tissue motion. Respiration cyclically deforms the tissue boundaries, thus varying the element-to-

element phase differences over time. Therefore, a phase estimate from one timepoint in the breath cycle may have decreased efficacy at other timepoints. Future work should measure this variation in performance to determine whether the phase correction needs to be updated throughout the breath cycle. Dynamic updates of the phase correction could potentially be achieved using collapse-based aberration correction. Here, collapse-based aberration correction required 1 s of computation time per correction in vivo without optimizing the computational efficiency but could likely be accelerated by parallelization and/or other strategies. Increasing the collapse-based correction rate to 2 Hz would permit ~6 updates per breath cycle (respiratory rate: 0.2 – 0.3 Hz [220], [221]) and a maximum tissue displacement between updates of 0.6 cm [222], [223]. Each update would use the cavitation emissions generated by therapy pulses to maintain the correction performance throughout the breath cycle. The feasibility of dynamic updates with the collapse signal will be explored in future work.

Finally, another important aim for future work will be to improve predictions of histotripsy focusing in the human abdomen by simulating nonlinear acoustic propagation. Numerical methods to model nonlinear propagation to the degree required by histotripsy are unavailable currently but may become available soon as acoustic simulation improves. Nonlinear propagation models could improve predictions of the histotripsy focus in two important ways. First, nonlinear models could improve the simulation of aberration effects in transabdominal histotripsy by accounting for the waveform distortions and amplitude changes induced by nonlinear propagation. As discussed in Chapter 2, the rarefactional pressure undergoes relatively moderate nonlinear distortion, suggesting the suitability of the linear

model to predict phase errors in histotripsy. However, at very high pressure amplitudes, the rarefactional phase broadens substantially and decreases in amplitude relative to the positive phase. These changes could alter predictions of the rarefactional focus relative to the linear case and should be investigated as nonlinear simulation methods become available. Nonlinear propagation models could also improve predictions of histotripsy focusing by accurately estimating transducer output at high amplitudes. Transducer output cannot be directly measured at high amplitudes due to the generation of cavitation and therefore must be estimated by extrapolating measurements made at subthreshold amplitudes or by modelling. Nonlinear numerical models have been developed to characterize transducer output but do not serve all transducer geometries and excitation waveforms [224], [225]. Therefore, many estimates rely on the extrapolation of low amplitude measurements and have limited accuracy [190]. Accurate predictions of focal pressure amplitude *in situ* could substantially improve treatment planning for transadominal histotripsy and enable personalized assessment of treatment feasibility for each patient.

6.3 Conclusion

Histotripsy is at a critical moment in its clinical translation, with recent FDA clearance enabling histotripsy treatment for many liver cancer patients in need. However, some patients may not qualify for treatment due to remaining technical challenges, one of which is phase aberration. The research in this Dissertation indicates that aberration correction could improve treatment efficacy and safety to expand the envelope of histotripsy in the liver. The Dissertation also demonstrated effective aberration correction *in vivo* using an array with similar dimensions to the current clinical device. Together, these results suggest that clinical

implementation of aberration correction is feasible and allows histotripsy treatment at more locations in the liver, thereby enabling non-invasive, non-thermal histotripsy therapy for more patients worldwide.

Appendix

A.1 Simulating Focused Ultrasound with k-Wave

In this appendix, I discuss the strengths and limitations of k-Wave for simulating focused ultrasound propagation in the human body and offer advice on how to set up such simulations. I adapt some mathematical analysis from the k-Wave manual (reference [226]) and other publications to explain how the numerical model works and thereby motivate my suggestions. At the end, I include example code with comments to illustrate the steps discussed here. This appendix is not meant to replace the k-Wave manual [226], which should be the first reference for anyone learning k-Wave. Instead, this appendix aims to help those interested in simulating focused ultrasound in tissue using k-Wave by highlighting topics relevant to this purpose.

A1.1. The k-Wave Numerical Model

Propagating sound waves obey the wave equation, which is given by

$$\nabla^2 p(\mathbf{x}, t) - \frac{1}{c_0^2}\frac{\partial^2 p}{\partial t^2}(\mathbf{x}, t) = 0 \qquad \text{(A1.1)},$$

where p is the acoustic pressure, c_0 is the speed of sound, $\mathbf{x}$ is a spatial coordinate vector, and t is time. Analytical solutions to the wave equation exist for acoustic sources with simple

geometry in a homogeneous medium [227]. For an arbitrary source shape and/or propagation through heterogeneous media, solving the wave equation typically requires a numerical method, where the space and time domains are discretized, and wave propagation is simulated step by step by approximating the spatial and temporal derivatives. Commonly, the derivatives are approximated by fitting a polynomial function at a few neighboring points of the discretized domain and differentiating [228]. This scheme, called a 'finite difference' approach, requires a fine discretization of time and space (often $<\frac{\lambda}{10}$, where λ is the acoustic wavelength [229], [230]) and is thus computationally intensive. To increase computation speed while maintaining accuracy, k-Wave first expresses the wave equation in the spatial frequency domain, or k-space, as in

$$\nabla^2 p(\mathbf{k}, t) - \frac{1}{c_0^2}\frac{\partial^2 p}{\partial t^2} p(\mathbf{k}, t) = 0 \qquad \text{(A1.2)},$$

where $\mathbf{k}$ is the wavevector. A truncated Fourier series is fit to the data in k-space using the Fast Fourier Transform (FFT), and the spatial derivative is calculated rapidly using the relationship $\mathcal{F}_{x\to k_x}\left\{\frac{\partial}{\partial x} f(x)\right\} = ik_x \mathcal{F}_{x\to k_x}\{f(x)\}$, where $\mathcal{F}_{x\to k_x}$ is the spatial Fourier transform [226]. Importantly, because the Fourier series functions are sinusoids, a discretization spacing of only $\frac{\lambda}{2}$ is theoretically sufficient for accurate simulations, significantly decreasing computational requirements compared to finite difference methods [168]. The k-Wave numerical model also takes advantage of this k-space representation when approximating the temporal derivative. The time derivative cannot be calculated directly in the Fourier domain due to causality. However, by re-writing the spatial derivative in k-space, equation A1.2 becomes

$$-k^2 p(\mathbf{k}, t) - \frac{1}{c_0^2}\frac{\partial^2 p}{\partial t^2} p(\mathbf{k}, t) = 0 \qquad \text{(A1.3)},$$

where k is the magnitude of the wavevector. This re-expression converts a partial differential equation (A1.2) to an ordinary differential equation (A1.3), for which a solution is

$$p(\mathbf{k}, t) = \cos(c_0 k t)\, p(\mathbf{k}, 0) \qquad \text{(A1.4) [226]}$$

In a standard second order finite difference approach, the time derivative would be discretized as $\frac{p(\mathbf{k},t+\Delta t)-2p(\mathbf{k},t)+p(\mathbf{k},t-\Delta t)}{\Delta t^2}$, where Δt is the time step. However, by substituting the solution in equation A1.4 into the equation A1.3 and re-arranging, the discretized time derivative becomes $\frac{p(\mathbf{k},t+\Delta t)-2p(\mathbf{k},t)+p(\mathbf{k},t-\Delta t)}{\Delta t^2 \mathrm{sinc}^2(c_0 k \Delta t/2)}$ [226]. The $\mathrm{sinc}(\ldots)$ term in the denominator permits larger time steps without loss of accuracy. Using these methods (a Fourier collocation method to calculate spatial derivatives and a k-space approach to calculate the temporal derivative), k-Wave solves the wave equation for arbitrary source shapes and heterogeneous media with relatively modest computational requirements. The following sections discuss strategies, best practices, and limitations for using k-Wave to model focused ultrasound propagation in the body.

A1.2. Defining the Simulation Domain

In k-Wave, the solution to the wave equation is computed on a spatial grid of regular spacing Δx and in fixed time steps Δt. In a homogeneous medium, the k-Wave numerical model gives an exact solution to the wave equation for any grid spacing $\Delta x \leq \frac{\lambda}{2}$ and for any size time step Δt [148]. For a heterogeneous medium, however, the numerical model becomes an approximate solution whose accuracy depends on the size of the grid spacing and the time step. Typically, $\Delta x \leq \frac{\lambda}{4}$ is required to accurately model reflections at media boundaries [226]. The size of the time step depends on how the time derivative is approximated. In the heterogeneous case, the sinc term in the denominator can be constructed using any value for the speed of sound, giving

$\Delta t^2 \mathrm{sinc}^2(c_{\mathrm{ref}} k \Delta t/2)$, where c_{ref} is a reference speed of sound [177]. Together, the choice of c_{ref} and Δt determine the stability and accuracy of the k-Wave simulation. In general, choosing $c_{\mathrm{ref}} = c_{\mathrm{max}}$ helps maintain stability (prevents the exponential increase of numerical errors) [226]. However, this choice of c_{ref} must be balanced by a sufficiently small Δt to limit numerical dispersion. Alternatively, choosing $c_{\mathrm{ref}} = c_{\mathrm{min}}$ limits numerical dispersion but can allow instability, unless Δt is sufficiently small [226]. This requirement is given by:

$$\Delta t \leq \frac{2\Delta x}{c_{\mathrm{min}} \pi} \sin^{-1}\left(\frac{c_{\mathrm{min}}}{c_{\mathrm{max}}}\right) \qquad \text{(A1.5) [226]}$$

I recommend the following strategy:

(1) Determine the highest frequency f_{max} to be simulated and find the minimum wavelength as $\lambda_{\mathrm{min}} = \frac{c_{\mathrm{min}}}{f_{\mathrm{max}}}$. Set $\Delta x \leq \frac{\lambda_{\mathrm{min}}}{4}$.

(2) Set $c_{\mathrm{ref}} = c_{\mathrm{min}}$ to limit slow-accumulating numerical dispersion, which is harder to detect than an instability.

(3) Set Δt using equation A1.5.

Once the discretization level has been set, the total number of points or steps in the domain can be assigned. The number of time steps should be sufficient to span the total simulated propagation time. In the spatial domain, the number of points along each axis should reach the desired spatial extent and have small prime factors to minimize the time required to compute the spatial derivatives with the FFT. Grid dimensions with high prime factors can substantially lengthen computation times. The k-Wave Toolbox includes a useful function called CheckFactors that takes two integers defining a range and returns numbers with low prime factors to help set grid dimensions.

When choosing the dimensions of the spatial grid, it is also important to account for the thickness of the perfectly matched layer (PML), a layer of grid points surrounding the simulation domain with nonphysical absorption parameters that attenuates waves exiting one side of the domain to prevent them from re-entering at the other side due to periodic Fourier boundary conditions. The absorption in the PML is governed by a power law like in tissue but is anisotropic (only acts on perpendicular components of incident waves) to prevent reflections back into the medium. The attenuation coefficient α_{PML} (in Np/m) and the PML thickness (in grid points) can be set using optional inputs to the main simulation functions (kSpaceFirstOrder…). Simulations with strongly absorbing media (e.g., bone) typically require thicker PMLs and/or larger PML absorption coefficients to adequately attenuate exiting sound waves [226]. However, a large PML absorption coefficient can cause instability, so it may be necessary to reduce the attenuation coefficient and enlarge the PML for an equivalent performance. I have found that a PML attenuation coefficient of 20 Np/m and a PML thickness of ~5 mm (36 dB total attenuation) are sufficient for 3D simulations with highly absorbing media (bone, lung, bowel). In the main simulation function, the user can also toggle whether the PML is placed inside or outside the grid dimensions defined by the user. The grid points forming the PML are included when computing the FFT. Thus, if the PML is placed outside the grid, these additional points should be accounted for to ensure that the final grid dimensions have low prime factors.

A1.3. Simulating Acoustic Propagation in Biological Tissues

The k-Wave numerical model accurately simulates propagation through heterogeneous media when the spatial and temporal discretization is sufficiently fine to model transmission

and reflection at the highest acoustic frequency of interest. Transmission and reflection between media with similar impedance can be simulated accurately with relatively large space and time steps ($\Delta x \approx \frac{\lambda}{4}$, and a Courant Friedrichs Lewy (CFL) number of 0.2 – 0.3). However, for a large impedance difference, like soft tissue to cortical bone or air (bowel or lung), the space and time steps must decrease to maintain accuracy and stability. Air (343 m s^{-1}, 1 kg m^{-3}) has very different acoustic properties from soft tissue (1540 m s^{-1}, 1100 kg m^{-3}) and is thus especially challenging to model. I have found that the density of air must be artificially increased to at least 100 kg m^{-3} to maintain stability, even when using fine space and time steps ($\Delta x < \frac{\lambda}{6}$, CFL = 0.05). I have also found that modelling air and bone in the same simulation increases the computational requirements still further (CFL < 0.025). Therefore, if the goal is to simply model bone and air as strong attenuators (i.e., highly reflective and absorptive), it may be convenient to assign air and bone the same acoustic properties to reduce computational requirements.

The k-Wave numerical model can also simulate power law attenuation of sound by biological tissues of the form $\alpha = \alpha_0 \omega^y$, where α is the depth-dependent attenuation in dB cm^{-1}, α_0 is the attenuation coefficient in dB MHz^{-y} cm^{-1}, ω is the acoustic frequency in MHz, and y is the power law exponent. The value of α_0 can vary in space (e.g., for different tissues), while the exponent y is constant. In k-Wave, power law absorption is modelled as a spatial gradient using a fractional Laplacian (a spatial derivative to a fractional power) [149]. This term also accounts for dispersion (frequency-dependent change in the speed of sound). Due to this formulation, y can only assume values between 0 and 3 and cannot exactly equal 1 ($0 < y < 3$,

and $y \neq 1$). The value of y also determines the relative influence of absorption and dispersion in the simulation. A y value closer to 1 results in a nearly linear relationship between absorption and acoustic frequency as in biological tissue but causes strong dispersion effects, especially at lower frequencies (0 – 5 MHz) [149]. A y value closer to 2 makes the absorption scale quadratically with frequency but produces mild dispersion effects. For histotripsy simulations, frequencies typically range between 0.5 – 1 MHz. At these low frequencies, the absorption coefficient is similar at $y \approx 1$ and $y \approx 2$. Therefore, a value of $y \approx 2$ is preferable for this frequency range to avoid strong dispersion effects.

The values of α_0 are not restricted to a specific range but are practically limited by the size of the time step. The attenuation term includes two spatial derivatives temporally offset by $\frac{\Delta t}{2}$ [226]. The phase error resulting from this offset is small for moderate absorption (e.g., by soft tissues) but large for strong absorption (e.g., by bone and air). Thus, to model frequency-dependent absorption by bone and air, the time step must be decreased to maintain stability and accuracy (relative to a simulation with soft tissue only). I have found that even for a low CFL of 0.04, absorption values >15 dB cm^{-1} can cause instability.

A1.4. Simulating Focused Ultrasound Transducers in k-Wave

In k-Wave, all pressure inputs are modelled as point sources in discrete space. Therefore, finite-sized, continuous acoustic sources are modelled using some combination of discretely spaced point sources. This discrete-space source is then represented in k-space using a truncated Fourier series. In therapeutic ultrasound, we often want to model a large, spherically curved transducer as our source. However, modelling such sources in k-Wave is challenging for several reasons. First, a spherical surface is not well-represented on a regular Cartesian grid.

Spheres intersect few grid points and are thus often modelled by placing point sources near the surface. If the grid spacing Δx is large compared to the radius of curvature, this approximation will introduce significant staircasing errors [180]. Furthermore, regardless of the grid spacing, the density of point sources representing the transducer will vary along the spherical surface. Portions of the sphere at small angles to the 3 cardinal planes will abut more grid points than highly oblique portions, causing the source amplitude to vary over the surface [179]. A second problem, which affects curved and flat sources alike, is that a finite 2-D surface in 3D space is not well represented by a truncated Fourier series [178]. By definition, a truncated Fourier series is band limited. However, a transducer has finite extent in physical space and thus has infinite bandwidth in Fourier space. Representation of an infinite bandwidth source with a finite number of spatial frequencies can cause severe errors in the resulting pressure distribution [178]. To address these problems, the most recent version of the k-Wave at the time of this writing (V.1.4) incorporates a new method to define sources with the kWaveArray object class. This object class allows the user to define sources directly in continuous Cartesian space. Then, the object class projects this infinite bandwidth source distribution onto the truncated Fourier series representing a given k-Wave grid, producing a band limited representation of the source which is then sampled in discrete space and appropriately scaled to compensate for variations in point density. This combination of scaled point sources can be used as input to the simulation functions to optimally represent curved, 2D transducers in k-Wave.

Conveniently, the kWaveArray object class also permits the definition of each array element individually and stores the indices needed to locate each element in the spatial grid and in the simulation output matrices. The geometry of each element can be defined using geometrical

parameters for common shapes like rectangles or discs. Alternatively, arbitrary element shapes can be defined by supplying points on an integration surface in Cartesian space (sampled at a resolution finer than Δx) [178].

In addition to defining the spatial distribution of the source, the user can define the time variation of the pressure input (a source signal). The kWaveArray object accepts an individual time-varying pressure signal for each element and then scales each signal using the weighting factors needed to define the band limited, evenly sampled source. This process is demonstrated in example code at the end of this appendix. In histotripsy, we often want to model a short pulse (1 – 2 cycles). It is important to ensure that the signal frequencies are supported by the discrete simulation domain. The maximum wavenumber supported by the simulation grid is $k_{max} = \frac{\pi}{\Delta x}$. Therefore, the maximum supported temporal frequency is $\frac{c_{\min}\pi}{\Delta x}$. Defining a time-varying pressure input with frequencies above the maximum produces phase errors in the numerical solution and thereby distorts the simulated acoustic field. The k-Wave Toolbox has a useful function called filterTimeSeries that attenuates signal frequency components not supported by a particular simulation grid.

A1.5. Sensors and Simulation Output Data

Focused ultrasound simulations often require discretized spatial domains with millions of grid points and a duration spanning thousands of time steps. Therefore, recording the simulated pressure at each grid point and every time step would require an enormous amount of computer memory. Often we simply want to know the maxima and minima of the pressure amplitude over the ultrasound field. The k-Wave simulation functions give the option to record

just the all-time maximum and/or minimum pressure at every grid point, which greatly reduces the output file size from the simulation. This recording scheme is convenient if the goal is to simulate the pressure field produced by a transducer. In other situations, we are interested in the time-varying pressure observed at specific points in space (e.g., the signals recorded by array elements). In this case, we can reduce the size of the output file by selecting grid points to be the locations of point sensors, each of which records the simulated pressure over time. (By default, the pressure is recorded at all timepoints but can be delayed to save memory by setting the option 'record_start_time' field in the 'sensor' struct, or, if using a computing cluster, with an optional command line input – see page 54 of the manual [226]). Point sensors are omnidirectional and therefore do not behave like physical sensors with finite directivity. To approximate the response of a finite-sized sensor in k-Wave, recorded signals must be combined from multiple point sensors sampling the desired sensor surface. As discussed previously, it is challenging to model a curved sensor on a discrete Cartesian grid. Fortunately, transducers defined with the kWaveArray object class can be used as sensors. The kWaveArray object sums and scales the output from point sensors to compensate variations in spatial sampling, returning one signal for each element (see the combineSensorData member function).

A1.6. Limitations for Simulating Focused Ultrasound

The k-Wave numerical model has many advantages for simulating focused ultrasound fields in the body. The model has been extensively validated and is considered accurate for linear to moderately nonlinear simulations of ultrasound propagation in weakly heterogeneous media [231]. Also, k-Wave uses pseudospectral and k-space methods to approximate the spatial and

temporal derivatives of the wave equation, dramatically reducing computation time and resources compared to finite-difference approximations. This computational efficiency is critical for focused ultrasound, which typically requires very large simulation domains spanning hundreds of wavelengths in all dimensions. However, k-Wave has some important limitations that should be considered when designing therapeutic ultrasound simulations. First, the k-Wave numerical model is highly accurate for weakly heterogeneous media (soft tissues) but can become inaccurate for media with large speed of sound or impedance differences. The discretized time-derivative in k-space (see section A1.1) only gives an exact solution if the medium is homogeneous. If the speed of sound varies, the sinc term in the denominator causes small phase errors that accumulate as the simulation progresses [168]. The rate of error accumulation depends on how much the speed of sound in the medium varies from c_{ref}, the reference sound speed discussed in section A1.2. The interface between soft tissue (1540 m s^{-1}) and bone (3500 m s^{-1}) can be modelled accurately in k-Wave for a relative large space and time step [82], [170]. Accurately modelling the interface between soft tissue and air (343 m s^{-1}), however, is not possible in k-Wave. The impedance of air differs from that of soft tissue by several orders of magnitude. Altering the acoustic properties of air (e.g., increasing the density of air to 100 kg m^{-3}) can help limit phase errors but requires a much smaller time step than a simulation without any air. Modelling air and bone in the same simulation and/or modelling absorption increases this requirement still further. Therefore, the k-Wave model cannot fully simulate focused ultrasound propagation in the abdomen, which includes interfaces between soft tissues, air pockets, and bone and absorption. Strong reflections and absorption are

modelled in k-Wave at the expense of phase accuracy in the numerical solution. The user must consider this tradeoff when simulating focused ultrasound in the body.

Second, k-Wave is capable of simulating moderately nonlinear ultrasound propagation (up to several harmonics) [231] but cannot simulate nonlinear focal waveforms like those in histotripsy. Higher frequencies require smaller time steps for accurate simulations. Thus, simulating even a few higher harmonics generated from nonlinear propagation can strongly increase computational requirements. At best, the nonlinear capability of k-Wave could be used to simulate the field at the second or third harmonic for applications in aberration correction or therapy focus imaging.

A.2 Selected k-Wave Scripts

A.1.1 TxSim(ct, target).m

This function sets up a simulation of a 256-element transducer in transmit mode.

```
function TxSim(ct,target)

% set current directory
cd('~/myDirectory')

% add the path to your k-wave toolbox:
addpath('~/k-Wave/')

% load transducer geometry. This file contains a list of element numbers
(element_labels) and coordinates (coords) for points in Cartesian space defining the
geometry of different elements. The point cloud is spatially sampled relative to the
k-Grid spacing by a factor of 2.
load(['rosnitskiy_256_upsampled.mat'])


% load CT data
% the CT data has the same shape as the k-Wave grid and has numeric labels
designating different tissues.
load(['CT' num2str(ct) '_target' num2str(target) '_labels.mat'])
```

```
% load the waveform to be emitted by the transucer elements
load(['filtered_signal.mat'])

% grid
PML_WIDTH = 16; % set the size of the PML in grid points.

DX = 0.3e-3; % (m) % set the grid spacing
DY = DX; % (m)
DZ = DY; % (m)

NX = 810 - PML_WIDTH; % set the number of grid points in the k-Wave grid
NY = 588 - PML_WIDTH;
NZ = 540 - PML_WIDTH;

FOC_POS = [397 286 479]; % set the grid point defining the target (and focus)

% time
NT = 10500; % number of time steps
DT = 11.8064e-09; % time step in seconds

% medium
ALPHA_POWER = 2; % removes dispersion, which can be extreme for lower frequencies

WATER_BATH_TEMP = 20; % (C)

AIR_SPEED = 900; %(m / s) % best not to set a very low sound speed like 343 m/s
AIR_DENSITY = 100 % (kg / m^3) % density of air must be increased for stability
AIR_ABSORPTION = 15; % (dB / MHz^2 / cm)

CARTILAGE_SPEED = 1650; % (m / s)
CARTILAGE_DENSITY = 1100; % (kg / m^3)
CARTILAGE_ABSORPTION = 5; % (dB / MHz^2 / cm)

CORTICAL_SPEED = 3520; % (m / s) % bone
CORTICAL_DENSITY = 1960; % (kg / m^3)
CORTICAL_ABSORPTION = 15; % (dB / MHz^2 / cm)

FAT_SPEED = 1430; % (m / s)
FAT_DENSITY = 916; % (kg / m^3)
FAT_ABSORPTION = 0.4; % (dB / MHz^2 / cm)

SKIN_SPEED = 1620; % (m / s)
SKIN_DENSITY = 1100; % (kg / m^3)
SKIN_ABSORPTION = 1.6; % (dB / MHz^2 / cm)

SOFT_TISSUE_SPEED = 1580; % (m / s)
SOFT_TISSUE_DENSITY = 1050; % (kg / m^3)
SOFT_TISSUE_ABSORPTION = 0.5; % (dB / MHz^2 / cm)

% source parameters
SOURCE_FREQ = 0.75; % (MHz)

% grid

% create the computational grid
```

```
kgrid = kWaveGrid(NX, DX, NY, DX, NZ, DX);

kgrid.t_array = 0 : DT : (NT * DT);

% calculate the actual CFL and PPW
disp(['PPW = ' num2str(AIR_SPEED / (DX * SOURCE_FREQ*1e6))]);
disp(['CFL = ' num2str(CORTICAL_SPEED * DT / DX)]);

% medium

medium.sound_speed = labels; medium.density = labels;
medium.alpha_coeff = labels; medium.alpha_power = ALPHA_POWER;

medium.sound_speed(medium.sound_speed == WATER_LABEL) =
waterSoundSpeed(WATER_BATH_TEMP);
medium.density(medium.density == WATER_LABEL) = waterDensity(WATER_BATH_TEMP);
medium.alpha_coeff(medium.alpha_coeff == WATER_LABEL) = waterAbsorption(SOURCE_FREQ,
WATER_BATH_TEMP);

medium.sound_speed(medium.sound_speed == AIR_LABEL) = AIR_SPEED;
medium.density(medium.density == AIR_LABEL) = AIR_DENSITY;
medium.alpha_coeff(medium.alpha_coeff == AIR_LABEL) = AIR_ABSORPTION;

medium.sound_speed(medium.sound_speed == CARTILAGE_LABEL) = CARTILAGE_SPEED;
medium.density(medium.density == CARTILAGE_LABEL) = CARTILAGE_DENSITY;
medium.alpha_coeff(medium.alpha_coeff == CARTILAGE_LABEL) = CARTILAGE_ABSORPTION;

medium.sound_speed(medium.sound_speed == CORTICAL_LABEL) = CORTICAL_SPEED;
medium.density(medium.density == CORTICAL_LABEL) = CORTICAL_DENSITY;
medium.alpha_coeff(medium.alpha_coeff == CORTICAL_LABEL) = CORTICAL_ABSORPTION;

medium.sound_speed(medium.sound_speed == FAT_LABEL) = FAT_SPEED;
medium.density(medium.density == FAT_LABEL) = FAT_DENSITY;
medium.alpha_coeff(medium.alpha_coeff == FAT_LABEL) = FAT_ABSORPTION;

medium.sound_speed(medium.sound_speed == SKIN_LABEL) = SKIN_SPEED;
medium.density(medium.density == SKIN_LABEL) = SKIN_DENSITY;
medium.alpha_coeff(medium.alpha_coeff == SKIN_LABEL) = SKIN_ABSORPTION;

medium.sound_speed(medium.sound_speed == SOFT_TISSUE_LABEL) = SOFT_TISSUE_SPEED;
medium.density(medium.density == SOFT_TISSUE_LABEL) = SOFT_TISSUE_DENSITY;
medium.alpha_coeff(medium.alpha_coeff == SOFT_TISSUE_LABEL) = SOFT_TISSUE_ABSORPTION;
medium.sound_speed_ref = min(medium.sound_speed(:));

% source
coords(:,3) = coords(:,3) + kgrid.z_vec(FOC_POS(3)); % shift Cartesian coords into
the k-Wave grid

% instantiate the kWaveArray object class
karray = kWaveArray('SinglePrecision', true) % SinglePrecision decreases memory

elemNum = length(unique(element_labels));

% for every element in the point cloud, define an element in the kWaveArray object
for element = 1 : elemNum
```

```
    logical_indices = element_labels == element;
    integration_points = coords(logical_indices, :)';
    karray.addCustomElement(integration_points, (DX/2)^2 *
size(integration_points,2), 2, ['Element ' num2str(element)])
end

% get the band-limited representation of the source and input it to the source mask
source.p_mask = karray.getArrayBinaryMask(kgrid);

% get the correct scaling factors for all signals to represent the band-limited
source
source.p =
karray.getDistributedSourceSignal(kgrid,repmat(filtered_signal',elemNum,1));

% sensor
sensor.mask = ones(NX, NY, NZ); % define a sensor mask filling the entire field
sensor.record={'p_max_all', 'p_min_all'}; % record the max and min pressures over the
field


% run simulation
% for cluster simulations, you'll want to save the data to an .h5 file using
'SaveToDisk' option input instead of running the simulation, so that you can run the
parallelized code.
filename = ['/scratch/zhenx_root/zhenx1/yeatsem/input_data_Tx_CT' num2str(ct)
'_target' num2str(target) '_' num2str(elemNum) 'elements.h5'];
input_args = ({'DataCast', 'single', 'PMLInside', false, ...
               'PMLSize', PML_WIDTH / 2, 'Smooth', [true, false, false], ...
               'PMLAlpha', 25, 'SaveToDisk', filename});
kspaceFirstOrder3D(kgrid, medium, source, sensor, input_args{:});

end
```

A.1.2 RxSim(ct, target)

This function sets up a simulation of a 256-element transducer in receive mode.

```
function RxSim(ct,target)

% set current directory
cd('~/myDirectory')

% add k-wave path:
addpath('~/k-Wave/')

% load transducer geometry – see above
load(['rosnitskiy_256_upsampled.mat'])


% load CT data – see above
load([DIREC 'CT' num2str(ct) '_target' num2str(target) '_labels.mat'])

% grid
PML_WIDTH = 16;

DX = 0.3e-3; % (m)
DY = DX; % (m)
DZ = DY; % (m)

NX = 810 - PML_WIDTH;
NY = 588 - PML_WIDTH;
NZ = 540 - PML_WIDTH;

FOC_POS = [397 286 479];

% time
NT = 10500;
DT = 11.8064e-09;

% medium
ALPHA_POWER = 2;

WATER_BATH_TEMP = 20; % (C)

AIR_SPEED = 900; %(m / s)
AIR_DENSITY = 100; % (kg / m^3)
AIR_ABSORPTION = 15; % (dB / MHz^2 / cm)

CARTILAGE_SPEED = 1650; % (m / s)
CARTILAGE_DENSITY = 1100; % (kg / m^3)
CARTILAGE_ABSORPTION = 5; % (dB / MHz^2 / cm)

CORTICAL_SPEED = 3520; % (m / s)
CORTICAL_DENSITY = 1960; % (kg / m^3)
```

```
CORTICAL_ABSORPTION = 15; % (dB / MHz^2 / cm)

FAT_SPEED = 1430; % (m / s)
FAT_DENSITY = 916; % (kg / m^3)
FAT_ABSORPTION = 0.4; % (dB / MHz^2 / cm)

SKIN_SPEED = 1620; % (m / s)
SKIN_DENSITY = 1100; % (kg / m^3)
SKIN_ABSORPTION = 1.6; % (dB / MHz^2 / cm)

SOFT_TISSUE_SPEED = 1580; % (m / s)
SOFT_TISSUE_DENSITY = 1050; % (kg / m^3)
SOFT_TISSUE_ABSORPTION = 0.5; % (dB / MHz^2 / cm)

% source parameters
SOURCE_FREQ = 0.75; % (MHz)

% sensor parameters
RECORD_START = 80e-6; % (s)

% grid

% create the computational grid
kgrid = kWaveGrid(NX, DX, NY, DX, NZ, DX);

kgrid.t_array = 0 : DT : (NT * DT);

% calculate the actual CFL and PPW
disp(['PPW = ' num2str(AIR_SPEED / (DX * SOURCE_FREQ*1e6))]);
disp(['CFL = ' num2str(CORTICAL_SPEED * DT / DX)]);

% medium

medium.sound_speed = labels; medium.density = labels;
medium.alpha_coeff = labels; medium.alpha_power = ALPHA_POWER;

medium.sound_speed(medium.sound_speed == WATER_LABEL) =
waterSoundSpeed(WATER_BATH_TEMP);
medium.density(medium.density == WATER_LABEL) = waterDensity(WATER_BATH_TEMP);
medium.alpha_coeff(medium.alpha_coeff == WATER_LABEL) = waterAbsorption(SOURCE_FREQ,
WATER_BATH_TEMP);

medium.sound_speed(medium.sound_speed == AIR_LABEL) = AIR_SPEED;
medium.density(medium.density == AIR_LABEL) = AIR_DENSITY;
medium.alpha_coeff(medium.alpha_coeff == AIR_LABEL) = AIR_ABSORPTION;

medium.sound_speed(medium.sound_speed == CARTILAGE_LABEL) = CARTILAGE_SPEED;
medium.density(medium.density == CARTILAGE_LABEL) = CARTILAGE_DENSITY;
medium.alpha_coeff(medium.alpha_coeff == CARTILAGE_LABEL) = CARTILAGE_ABSORPTION;

medium.sound_speed(medium.sound_speed == CORTICAL_LABEL) = CORTICAL_SPEED;
medium.density(medium.density == CORTICAL_LABEL) = CORTICAL_DENSITY;
medium.alpha_coeff(medium.alpha_coeff == CORTICAL_LABEL) = CORTICAL_ABSORPTION;

medium.sound_speed(medium.sound_speed == FAT_LABEL) = FAT_SPEED;
```

```
medium.density(medium.density == FAT_LABEL) = FAT_DENSITY;
medium.alpha_coeff(medium.alpha_coeff == FAT_LABEL) = FAT_ABSORPTION;

medium.sound_speed(medium.sound_speed == SKIN_LABEL) = SKIN_SPEED;
medium.density(medium.density == SKIN_LABEL) = SKIN_DENSITY;
medium.alpha_coeff(medium.alpha_coeff == SKIN_LABEL) = SKIN_ABSORPTION;

medium.sound_speed(medium.sound_speed == SOFT_TISSUE_LABEL) = SOFT_TISSUE_SPEED;
medium.density(medium.density == SOFT_TISSUE_LABEL) = SOFT_TISSUE_DENSITY;
medium.alpha_coeff(medium.alpha_coeff == SOFT_TISSUE_LABEL) = SOFT_TISSUE_ABSORPTION;
medium.sound_speed_ref = min(medium.sound_speed(:));

% source

% set an instantaneous pressure distribution to define a point source. (a spatial
Dirac delta)
source.p0 = zeros(NX,NY,NZ);
source.p0(FOC_POS(1),FOC_POS(2),FOC_POS(3)) = 1;

% sensor
coords(:,3) = coords(:,3) + kgrid.z_vec(FOC_POS(3));

karray = kWaveArray('SinglePrecision', true);


elemNum = length(unique(element_labels));

% define the elements of the array using the kWaveArray object, just like above.
for element = 1 : elemNum
    logical_indices = element_labels == element;
    integration_points = coords(logical_indices, :)';
    karray.addCustomElement(integration_points, (DX/2)^2 *
size(integration_points,2), 2, ['Element ' num2str(element)])

end


sensor.record = {'p'}; % record time-varying pressure
sensor.mask = karray.getArrayBinaryMask(kgrid); % set band-limited source as sensor
sensor.record_start_index = round(RECORD_START / DT); % recording delay (for cluster
simulations, need to be set as input to the binary function)




% run simulation
filename = ['/scratch/zhenx_root/zhenx1/yeatsem/input_data_Rx_CT' num2str(ct)
'_target' num2str(target) '_' num2str(elemNum) 'elements.h5'];
input_args = ({'DataCast', 'single', 'PMLInside', false, ...
               'PMLSize', PML_WIDTH / 2, 'PMLAlpha', 25, 'SaveToDisk', filename});

kspaceFirstOrder3D(kgrid, medium, source, sensor, input_args{:});

end
```

A.1.3 RunBatch.sh

This bash script sets up transmit and receive k-Wave simulations for multiple CTs (subjects) and targets (locations in the liver) to run at once on the Great Lakes cluster. It loops through c (the CT identifiers) and t (the target identifiers) and for each combination, writes two new bash scripts. One bash script sets up a transmit simulation, while the other sets up a receive simulation. Both scripts call MATLAB to set up the simulation data using TxSim.m or RxSim.m. Then, the scripts call the binary 'kSpaceFirstOrder-OMP' to run the parallelized k-Wave simulation code. At the end of this script, the function sbatch sends the newly generated bash scripts to the Slurm job manager to start the simulations.

```
#!/bin/bash

for c in 5

do

for t in 1 2 4 6 8 9 10 11 12 13 14 15 16 17 19 20 21 23 24 25 26 28 29 30

do


echo "#!/bin/bash
#SBATCH --job-name=txT${t}C${c}
#SBATCH --ntasks=30
#SBATCH --mem=40g
#SBATCH --time=0-4:30:00
#SBATCH --mail-user=yeatsem@umich.edu
#SBATCH --mail-type=FAIL
#SBATCH --nodes=1
#SBATCH --account=zhenx0
#SBATCH --partition=standard

cd ~/pap3
module load matlab/R2021b
matlab -nodesktop -nojvm -r \"TxSim($c,$t); exit\"
```

```
export OMP_PLACES=cores
export OMP_PROC_BIND=true

cd ~/k-Wave/binaries
./kspaceFirstOrder-OMP -i
/scratch/zhenx_root/zhenx1/yeatsem/input_data_Tx_CT${c}_target${t}.h5 -o
/scratch/zhenx_root/zhenx1/yeatsem/output_data_Tx_CT${c}_target${t}.h5 --
p_max_all --p_min_all
exit" > tx_C${c}_T${t}.sh
sbatch tx_C${c}_T${t}.sh




echo "#!/bin/bash

#SBATCH --job-name=rxT${t}C${c}
#SBATCH --ntasks=30
#SBATCH --mem=40g
#SBATCH --time=0-4:30:00
#SBATCH --mail-user=yeatsem@umich.edu
#SBATCH --mail-type=FAIL
#SBATCH --nodes=1
#SBATCH --account=zhenx0
#SBATCH --partition=standard

cd ~/pap3
module load matlab/R2021b
matlab -nodesktop -nojvm -r \"RxSim($c,$t); exit\"

export OMP_PLACES=cores
export OMP_PROC_BIND=true

cd ~/k-Wave/binaries
./kspaceFirstOrder-OMP -i
/scratch/zhenx_root/zhenx1/yeatsem/input_data_Rx_CT${c}_target${t}.h5 -o
/scratch/zhenx_root/zhenx1/yeatsem/output_data_Rx_CT${c}_target${t}.h5 --
p_raw
exit" > rx_C${c}_T${t}.sh
sbatch rx_C${c}_T${t}.sh

done
done
exit
```

References

[1] S. W. Flax and M. O'Donnell, "Phase-aberration correction using signals from point reflectors and diffuse scatterers: basic principles," *IEEE Trans. Ultrason. Ferroelectr. Freq. Control*, vol. 35, no. 6, pp. 758–767, Nov. 1988, doi: 10.1109/58.9333.

[2] J. Yasuda, H. Yoshikawa, and H. Tanaka, "Phase aberration correction for focused ultrasound transmission by refraction compensation," *Jpn. J. Appl. Phys.*, vol. 58, no. SG, p. SGGE22, Jul. 2019, doi: 10.7567/1347-4065/ab19aa.

[3] G. E. Trahey, P. D. Freiburger, L. F. Nock, and D. C. Sullivan, "In vivo measurements of ultrasonic beam distortion in the breast," *Ultrason. Imaging*, vol. 13, no. 1, pp. 71–90, Jan. 1991, doi: 10.1016/0161-7346(91)90071-O.

[4] J. J. Dahl, D. A. Guenther, and G. E. Trahey, "Adaptive imaging and spatial compounding in the presence of aberration," *IEEE Trans. Ultrason. Ferroelectr. Freq. Control*, vol. 52, no. 7, pp. 1131–1144, Jul. 2005, doi: 10.1109/TUFFC.2005.1503999.

[5] G. F. Pinton, G. E. Trahey, and J. J. Dahl, "Sources of image degradation in fundamental and harmonic ultrasound imaging using nonlinear, full-wave simulations," *IEEE Trans. Ultrason. Ferroelectr. Freq. Control*, vol. 58, no. 4, pp. 754–765, Apr. 2011, doi: 10.1109/TUFFC.2011.1868.

[6] L. M. Hinkelman, T. D. Mast, L. A. Metlay, and R. C. Waag, "The effect of abdominal wall morphology on ultrasonic pulse distortion. Part I. Measurements," *J. Acoust. Soc. Am.*, vol. 104, no. 6, pp. 3635–3649, Dec. 1998, doi: 10.1121/1.423946.

[7] M. Fink, "Time reversal of ultrasonic fields. I. Basic principles," *IEEE Trans. Ultrason. Ferroelectr. Freq. Control*, vol. 39, no. 5, pp. 555–566, Sep. 1992, doi: 10.1109/58.156174.

[8] D. Liu and R. C. Waag, "Correction of ultrasonic wavefront distortion using backpropagation and a reference waveform method for time-shift compensation," *J. Acoust. Soc. Am.*, vol. 96, no. 2, pp. 649–660, Aug. 1994, doi: 10.1121/1.410304.

[9] G. Chau, M. Jakovljevic, R. Lavarello, and J. Dahl, "A Locally Adaptive Phase Aberration Correction (LAPAC) Method for Synthetic Aperture Sequences," *Ultrason. Imaging*, vol. 41, no. 1, pp. 3–16, Jan. 2019, doi: 10.1177/0161734618796556.

[10] H. Bendjador, T. Deffieux, and M. Tanter, "The SVD Beamformer: Physical Principles and Application to Ultrafast Adaptive Ultrasound," *IEEE Trans. Med. Imaging*, vol. 39, no. 10, pp. 3100–3112, Oct. 2020, doi: 10.1109/TMI.2020.2986830.

[11] W. Lambert, L. A. Cobus, T. Frappart, M. Fink, and A. Aubry, "Distortion matrix approach for ultrasound imaging of random scattering media," *Proc. Natl. Acad. Sci.*, vol. 117, no. 26, p. 14645, Jun. 2020, doi: 10.1073/pnas.1921533117.

[12] L. Nock, G. E. Trahey, and S. W. Smith, "Phase aberration correction in medical ultrasound using speckle brightness as a quality factor," *J. Acoust. Soc. Am.*, vol. 85, no. 5, pp. 1819–1833, May 1989, doi: 10.1121/1.397889.

[13] M. Urban, M. Bernal, and J. Greenleaf, "Phase aberration correction using ultrasound radiation force and vibrometry optimization," *IEEE Trans. Ultrason. Ferroelectr. Freq. Control*, vol. 54, no. 6, pp. 1142–1153, Jun. 2007, doi: 10.1109/TUFFC.2007.368.

[14] M. Jaeger, E. Robinson, H. G. Akarçay, and M. Frenz, “Full correction for spatially distributed speed-of-sound in echo ultrasound based on measuring aberration delays via transmit beam steering,” *Phys. Med. Biol.*, vol. 60, no. 11, pp. 4497–4515, Jun. 2015, doi: 10.1088/0031-9155/60/11/4497.

[15] R. Rau, D. Schweizer, V. Vishnevskiy, and O. Goksel, “Ultrasound Aberration Correction based on Local Speed-of-Sound Map Estimation,” in *2019 IEEE International Ultrasonics Symposium (IUS)*, Oct. 2019, pp. 2003–2006. doi: 10.1109/ULTSYM.2019.8926297.

[16] R. Ali *et al.*, “Sound speed estimation in layered media using the angular coherence of plane waves,” *Proc SPIE*, vol. 11319, Mar. 2020, doi: 10.1117/12.2548878.

[17] G. Chau, J. Dahl, and R. Lavarello, “Effects of Phase Aberration and Phase Aberration Correction on the Minimum Variance Beamformer,” *Ultrason. Imaging*, vol. 40, no. 1, pp. 15–34, Jan. 2018, doi: 10.1177/0161734617717768.

[18] Z. Liu, X. Guo, J. Tu, and D. Zhang, “Variations in Temperature Distribution and Tissue Lesion Formation Induced by Tissue Inhomogeneity for Therapeutic Ultrasound,” *Ultrasound Med. Biol.*, vol. 40, no. 8, pp. 1857–1868, Aug. 2014, doi: 10.1016/j.ultrasmedbio.2014.02.004.

[19] K. Li, Y. Chen, Y. Xu, J. Bai, Y. Chen, and X. Ji, “Tilting high-intensity focused ultrasound phased array to augment the focal steering range for treatment of uterine fibroids,” *Appl. Acoust.*, vol. 166, p. 107342, Sep. 2020, doi: 10.1016/j.apacoust.2020.107342.

[20] A. I. Farrer *et al.*, “Phase aberration simulation study of MRgFUS breast treatments,” *Med. Phys.*, vol. 43, no. 3, pp. 1374–1384, 2016, doi: 10.1118/1.4941013.

[21] R. Narumi *et al.*, “Numerical estimation of HIFU focal error for breast cancer treatment,” in *2013 IEEE International Ultrasonics Symposium (IUS)*, Jul. 2013, pp. 926–929. doi: 10.1109/ULTSYM.2013.0238.

[22] A. Grisey, M. Heidmann, V. Letort, P. Lafitte, and S. Yon, “Influence of Skin and Subcutaneous Tissue on High-Intensity Focused Ultrasound Beam: Experimental Quantification and Numerical Modeling,” *Ultrasound Med. Biol.*, vol. 42, no. 10, pp. 2457–2465, Oct. 2016, doi: 10.1016/j.ultrasmedbio.2016.06.013.

[23] K. Okita *et al.*, “Effects of breast structure on high-intensity focused ultrasound focal error,” *J. Ther. Ultrasound*, vol. 6, no. 1, p. 4, Jun. 2018, doi: 10.1186/s40349-018-0111-9.

[24] R. Ritchie, J. Collin, C. Coussios, and T. Leslie, “Attenuation and De-focusing During High-Intensity Focused Ultrasound Therapy Through Peri-nephric Fat,” *Ultrasound Med. Biol.*, vol. 39, no. 10, pp. 1785–1793, Oct. 2013, doi: 10.1016/j.ultrasmedbio.2013.04.010.

[25] R. W. Ritchie *et al.*, “Extracorporeal high intensity focused ultrasound for renal tumours: a 3-year follow-up,” *BJU Int.*, vol. 106, no. 7, p. 1004, 2010.

[26] C. Mougenot, M. Tillander, J. Koskela, M. O. Köhler, C. Moonen, and M. Ries, “High intensity focused ultrasound with large aperture transducers: A MRI based focal point correction for tissue heterogeneity,” *Med. Phys.*, vol. 39, no. 4, pp. 1936–1945, Apr. 2012, doi: 10.1118/1.3693051.

[27] A. M. Abbas, C. C.- Coussios, and O. R. Cleveland, “Patient Specific Simulation of HIFU Kidney Tumour Ablation,” in *2018 40th Annual International Conference of the IEEE Engineering in Medicine and Biology Society (EMBC)*, Jul. 2018, pp. 5709–5712. doi: 10.1109/EMBC.2018.8513647.

[28] V. Suomi, J. Jaros, B. Treeby, and R. Cleveland, “Nonlinear 3-D simulation of high-intensity focused ultrasound therapy in the Kidney,” in *2016 38th Annual International Conference of the IEEE Engineering in Medicine and Biology Society (EMBC)*, Orlando, FL, USA: IEEE, Aug. 2016, pp. 5648–5651. doi: 10.1109/EMBC.2016.7592008.

[29] T. D. Khokhlova *et al.*, “Pilot in vivo studies on transcutaneous boiling histotripsy in porcine liver and kidney,” *Sci. Rep.*, vol. 9, no. 1, p. 20176, Dec. 2019, doi: 10.1038/s41598-019-56658-7.

[30] D. Li, G. Shen, J. Bai, and Y. Chen, “Focus Shift and Phase Correction in Soft Tissues During Focused Ultrasound Surgery,” *IEEE Trans. Biomed. Eng.*, vol. 58, no. 6, pp. 1621–1628, Jun. 2011, doi: 10.1109/TBME.2011.2106210.

[31] Z. Xu *et al.*, “Controlled ultrasound tissue erosion.,” *IEEE Trans. Ultrason. Ferroelectr. Freq. Control*, vol. 51, no. 6, pp. 726–736, 2004, doi: 10.1109/TUFFC.2004.1304271.

[32] V. A. Khokhlova *et al.*, “Histotripsy methods in mechanical disintegration of tissue: Towards clinical applications,” *Int J Hyperth.*, vol. 31, no. 2, pp. 1464–5157, 2015, doi: 10.3109/02656736.2015.1007538.

[33] A. D. Maxwell, C. a. Cain, T. L. Hall, J. B. Fowlkes, and Z. Xu, “Probability of Cavitation for Single Ultrasound Pulses Applied to Tissues and Tissue-Mimicking Materials,” *Ultrasound Med. Biol.*, vol. 39, no. 3, pp. 449–465, 2013, doi: 10.1016/j.ultrasmedbio.2012.09.004.

[34] A. D. Maxwell *et al.*, “Cavitation clouds created by shock scattering from bubbles during histotripsy,” *J. Acoust. Soc. Am.*, vol. 130, no. 4, p. 1888, 2011, doi: 10.1121/1.3625239.

[35] Z. Xu, T. L. Hall, E. Vlaisavljevich, and F. T. Lee, “Histotripsy: the first noninvasive, non-ionizing, non-thermal ablation technique based on ultrasound,” *Int. J. Hyperthermia*, vol. 38, no. 1, pp. 561–575, Jan. 2021, doi: 10.1080/02656736.2021.1905189.

[36] E. Vlaisavljevich, A. Maxwell, L. Mancia, E. Johnsen, C. Cain, and Z. Xu, “Visualizing the Histotripsy Process: Bubble Cloud–Cancer Cell Interactions in a Tissue-Mimicking Environment,” *Ultrasound Med. Biol.*, vol. 42, no. 10, pp. 2466–2477, 2016, doi: 10.1016/j.ultrasmedbio.2016.05.018.

[37] N. Lu *et al.*, “Transcranial Magnetic Resonance-Guided Histotripsy for Brain Surgery: Pre-clinical Investigation,” *Ultrasound Med. Biol.*, vol. 48, no. 1, pp. 98–110, Jan. 2022, doi: 10.1016/j.ultrasmedbio.2021.09.008.

[38] J. R. Sukovich *et al.*, “In vivo histotripsy brain treatment,” *J. Neurosurg. JNS*, vol. 131, no. 4, pp. 1331–1338, Oct. 2019, doi: 10.3171/2018.4.JNS172652.

[39] A. Hendricks-Wenger *et al.*, “Histotripsy for the Treatment of Cholangiocarcinoma Liver Tumors: In Vivo Feasibility and Ex Vivo Dosimetry Study,” *IEEE Trans. Ultrason. Ferroelectr. Freq. Control*, vol. 68, no. 9, pp. 2953–2964, Sep. 2021, doi: 10.1109/TUFFC.2021.3073563.

[40] Z. Xu, G. Owens, D. Gordon, C. Cain, and A. Ludomirsky, “Noninvasive creation of an atrial septal defect by histotripsy in a canine model,” *Circulation*, vol. 121, no. 6, pp. 742–749, 2010, doi: 10.1161/CIRCULATIONAHA.109.889071.

[41] E. Vlaisavljevich *et al.*, “Non-invasive Liver Ablation Using Histotripsy: Preclinical Safety Study in an in Vivo Porcine Model,” *Ultrasound Med. Biol.*, pp. 1–15, 2017, doi: 10.1016/j.ultrasmedbio.2017.01.016.

[42] G. E. Owens *et al.*, “Intermediate-Term Effects of Intracardiac Communications Created Noninvasively by Therapeutic Ultrasound (Histotripsy) in a Porcine Model,” *Pediatr. Cardiol.*, vol. 33, no. 1, pp. 83–89, Jan. 2012, doi: 10.1007/s00246-011-0094-6.

[43] E. Vlaisavljevich *et al.*, “Image-Guided Non-Invasive Ultrasound Liver Ablation Using Histotripsy: Feasibility Study in an In Vivo Porcine Model,” *Ultrasound Med. Biol.*, vol. 39, no. 8, pp. 1398–1409, 2013, doi: 10.1016/j.ultrasmedbio.2013.02.005.

[44] W. W. Roberts, T. L. Hall, K. Ives, J. S. Wolf, J. B. Fowlkes, and C. a. Cain, “Pulsed cavitational ultrasound: A noninvasive technology for controlled tissue ablation (histotripsy) in the rabbit kidney,” *J. Urol.*, vol. 175, no. 2, pp. 734–738, 2006, doi: 10.1016/S0022-5347(05)00141-2.

[45] T. L. Hall, K. Kieran, K. Ives, J. B. Fowlkes, C. A. Cain, and W. W. Roberts, “Histotripsy of Rabbit Renal Tissue in Vivo: Temporal Histologic Trends,” *J. Endourol.*, vol. 21, no. 10, pp. 1159–1166, Oct. 2007, doi: 10.1089/end.2007.9915.

[46] T. L. Hall, C. R. Hempel, K. Wojno, Z. Xu, C. a. Cain, and W. W. Roberts, “Histotripsy of the Prostate: Dose Effects in a Chronic Canine Model,” *Urology*, vol. 74, no. 4, pp. 932–937, 2009, doi: 10.1016/j.urology.2009.03.049.

[47] T. G. Schuster, J. T. Wei, K. Hendlin, R. Jahnke, and W. W. Roberts, “Histotripsy Treatment of Benign Prostatic Enlargement Using the Vortx Rx System: Initial Human Safety and Efficacy Outcomes,” *Urology*, vol. 114, pp. 184–187, Apr. 2018, doi: 10.1016/j.urology.2017.12.033.

[48] Y. Kim, T.-Y. Wang, Z. Xu, and C. A. Cain, “Lesion generation through ribs using histotripsy therapy without aberration correction,” *IEEE Trans. Ultrason. Ferroelectr. Freq. Control*, vol. 58, no. 11, pp. 2334–2343, Nov. 2011, doi: 10.1109/TUFFC.2011.2091.

[49] Y. Kim, E. Vlaisavljevich, G. E. Owens, S. P. Allen, C. A. Cain, and Z. Xu, “In vivotranscostal histotripsy therapy without aberration correction,” *Phys. Med. Biol.*, vol. 59, no. 11, pp. 2553–2568, May 2014, doi: 10.1088/0031-9155/59/11/2553.

[50] J. R. Sukovich *et al.*, “Targeted Lesion Generation Through the Skull Without Aberration Correction Using Histotripsy,” *IEEE Trans. Ultrason. Ferroelectr. Freq. Control*, vol. 63, no. 5, pp. 671–682, May 2016, doi: 10.1109/TUFFC.2016.2531504.

[51] J. Gao, S. Cochran, and Z. Huang, “Ultrasound beam distortion and pressure reduction in transcostal focused ultrasound surgery,” *Appl. Acoust.*, vol. 76, pp. 337–345, Feb. 2014, doi: 10.1016/j.apacoust.2013.06.003.

[52] J.-L. Li, X.-Z. Liu, D. Zhang, and X.-F. Gong, “Influence of Ribs on the Nonlinear Sound Field of Therapeutic Ultrasound,” *Ultrasound Med. Biol.*, vol. 33, no. 9, pp. 1413–1420, Sep. 2007, doi: 10.1016/j.ultrasmedbio.2007.05.001.

[53] V. A. Khokhlova, S. M. Bobkova, and L. R. Gavrilov, “Focus splitting associated with propagation of focused ultrasound through the rib cage,” *Acoust. Phys.*, vol. 56, no. 5, pp. 665–674, Sep. 2010, doi: 10.1134/S106377101005012X.

[54] J. Lin, X. Liu, X. Gong, Z. Ping, and J. Wu, “Computational study on the propagation of strongly focused nonlinear ultrasound in tissue with rib-like structures,” *J. Acoust. Soc. Am.*, vol. 134, no. 2, pp. 1702–1714, Aug. 2013, doi: 10.1121/1.4812897.

[55] O. Lorton *et al.*, “A Novel Concept of a Phased-Array HIFU Transducer Optimized for MR-Guided Hepatic Ablation: Embodiment and First In-Vivo Studies,” *Front. Oncol.*, vol. 12, 2022, doi: 10.3389/fonc.2022.899440.

[56] S. Bobkova, L. Gavrilov, V. Khokhlova, A. Shaw, and J. Hand, “Focusing of High-Intensity Ultrasound Through the Rib Cage Using a Therapeutic Random Phased Array,” *Ultrasound Med. Biol.*, vol. 36, no. 6, pp. 888–906, Jun. 2010, doi: 10.1016/j.ultrasmedbio.2010.03.007.

[57] B. G. Bardsley and D. A. Christensen, “Beam patterns from pulsed ultrasonic transducers using linear systems theory,” *J. Acoust. Soc. Am.*, vol. 69, no. 1, pp. 25–30, Jan. 1981, doi: 10.1121/1.385346.

[58] A. D. Maxwell, C. A. Cain, T. L. Hall, J. B. Fowlkes, and Z. Xu, “Probability of Cavitation for Single Ultrasound Pulses Applied to Tissues and Tissue-Mimicking Materials,” *Ultrasound Med. Biol.*, vol. 39, no. 3, pp. 449–465, Mar. 2013, doi: 10.1016/j.ultrasmedbio.2012.09.004.

[59] E. Vlaisavljevich, A. Maxwell, M. Warnez, E. Johnsen, C. A. Cain, and Z. Xu, “Histotripsy-induced cavitation cloud initiation thresholds in tissues of different mechanical properties,” *IEEE Trans. Ultrason. Ferroelectr. Freq. Control*, vol. 61, no. 2, pp. 341–352, Feb. 2014, doi: 10.1109/TUFFC.2014.6722618.

[60] K. Lin *et al.*, “Histotripsy beyond the intrinsic cavitation threshold using very short ultrasound pulses: microtripsy,” *IEEE Trans. Ultrason. Ferroelectr. Freq. Control*, vol. 61, no. 2, pp. 251–265, Feb. 2014, doi: 10.1109/TUFFC.2014.6722611.

[61] F. A. Duck, “Chapter 4 - Acoustic Properties of Tissue at Ultrasonic Frequencies,” in *Physical Properties of Tissues*, F. A. Duck, Ed., London: Academic Press, 1990, pp. 73–135. doi: 10.1016/B978-0-12-222800-1.50008-5.

[62] V. A. Khokhlova *et al.*, “Histotripsy methods in mechanical disintegration of tissue: Towards clinical applications,” *Int. J. Hyperthermia*, vol. 31, no. 2, pp. 145–162, Feb. 2015, doi: 10.3109/02656736.2015.1007538.

[63] J. J. Macoskey *et al.*, “Soft-Tissue Aberration Correction for Histotripsy,” *IEEE Trans. Ultrason. Ferroelectr. Freq. Control*, vol. 65, no. 11, pp. 2073–2085, 2018, doi: 10.1109/TUFFC.2018.2872727.

[64] Y. Kim *et al.*, “Non-invasive pulsed cavitational ultrasound for fetal tissue ablation: feasibility study in a fetal sheep model,” *Ultrasound Obstet. Gynecol.*, vol. 37, no. 4, pp. 450–457, Apr. 2011, doi: 10.1002/uog.8880.

[65] P. Hytiroglou, Y. N. Park, G. Krinsky, and N. D. Theise, “Hepatic Precancerous Lesions and Small Hepatocellular Carcinoma,” *Gastroenterol. Clin. North Am.*, vol. 36, no. 4, pp. 867–887, Dec. 2007, doi: 10.1016/j.gtc.2007.08.010.

[66] E. Vlaisavljevich, T. Gerhardson, T. Hall, and Z. Xu, “Effects of f-number on the histotripsy intrinsic threshold and cavitation bubble cloud behavior,” *Phys. Med. Biol.*, vol. 62, no. 4, pp. 1269–1290, 2017, doi: 10.1088/1361-6560/aa54c7.

[67] H. Wang, E. S. Ebbini, M. O’Donnell, and C. a. Cain, “Phase aberration correction and motion compensation for ultrasonic hyperthermia phased arrays: experimental results,” *IEEE Trans. Ultrason. Ferroelectr. Freq. Control*, vol. 41, no. 1, pp. 34–43, 1994, doi: 10.1109/58.265818.

[68] K. Hynynen and R. M. Jones, “Image-guided ultrasound phased arrays are a disruptive technology for non-invasive therapy,” *Phys. Med. Biol.*, vol. 61, no. 17, p. R206, Aug. 2016, doi: 10.1088/0031-9155/61/17/R206.

[69] M. Pernot *et al.*, “High Power Phased Array Prototype for Clinical High Intensity Focused Ultrasound : Applications to Transcostal and Transcranial Therapy,” in *2007 29th Annual International Conference of the IEEE Engineering in Medicine and Biology Society*, Aug. 2007, pp. 234–237. doi: 10.1109/IEMBS.2007.4352266.

[70] X. Yin and K. Hynynen, “A numerical study of transcranial focused ultrasound beam propagation at low frequency,” *Phys. Med. Biol.*, vol. 50, no. 8, pp. 1821–1836, 2005, doi: 10.1088/0031-9155/50/8/013.

[71] P. J. White, P. von Pattenberg, and G. T. Clement, “A nonlinear method for high-intensity focused ultrasound (HIFU) aberration reduction,” in *2008 IEEE Ultrasonics Symposium*, Nov. 2008, pp. 2059–2061. doi: 10.1109/ULTSYM.2008.0508.

[72] K.-W. Lin, A. P. Duryea, Y. Kim, T. L. Hall, Z. Xu, and C. A. Cain, “Dual-beam histotripsy: a low-frequency pump enabling a high-frequency probe for precise lesion formation,” *IEEE Trans. Ultrason. Ferroelectr. Freq. Control*, vol. 61, no. 2, pp. 325–340, Feb. 2014, doi: 10.1109/TUFFC.2014.6722617.

[73] T. Christopher, “Finite amplitude distortion-based inhomogeneous pulse echo ultrasonic imaging,” *IEEE Trans. Ultrason. Ferroelectr. Freq. Control*, vol. 44, no. 1, pp. 125–139, Jan. 1997, doi: 10.1109/58.585208.

[74] X. Serres-Créixams *et al.*, “Contrast-Enhanced Ultrasound: A Useful Tool to Study and Monitor Hepatic Tumors Treated With Histotripsy,” *IEEE Trans. Ultrason. Ferroelectr. Freq. Control*, vol. 68, no. 9, pp. 2853–2860, Sep. 2021, doi: 10.1109/TUFFC.2021.3073540.

[75] J. Vidal-Jove *et al.*, “First-in-man histotripsy of hepatic tumors: the THERESA trial, a feasibility study,” *Int. J. Hyperthermia*, vol. 39, no. 1, pp. 1115–1123, Dec. 2022, doi: 10.1080/02656736.2022.2112309.

[76] G. T. Clement and K. Hynynen, “A non-invasive method for focusing ultrasound through the human skull,” *Phys. Med. Biol.*, vol. 47, no. 8, pp. 1219–1236, Apr. 2002, doi: 10.1088/0031-9155/47/8/301.

[77] R. M. Jones and K. Hynynen, “Comparison of analytical and numerical approaches for CT-based aberration correction in transcranial passive acoustic imaging,” *Phys. Med. Biol.*, vol. 61, no. 1, pp. 23–36, Nov. 2015, doi: 10.1088/0031-9155/61/1/23.

[78] G. F. Pinton, J.-F. Aubry, and M. Tanter, “Direct phase projection and transcranial focusing of ultrasound for brain therapy,” *IEEE Trans. Ultrason. Ferroelectr. Freq. Control*, vol. 59, no. 6, pp. 1149–1159, Jun. 2012, doi: 10.1109/TUFFC.2012.2305.

[79] J.-F. Aubry, M. Tanter, M. Pernot, J.-L. Thomas, and M. Fink, “Experimental demonstration of noninvasive transskull adaptive focusing based on prior computed tomography scans,” *J. Acoust. Soc. Am.*, vol. 113, no. 1, pp. 84–93, Jan. 2003, doi: 10.1121/1.1529663.

[80] F. Marquet *et al.*, “Non-invasive transcranial ultrasound therapy based on a 3D CT scan: protocol validation andin vitroresults,” *Phys. Med. Biol.*, vol. 54, no. 9, pp. 2597–2613, Apr. 2009, doi: 10.1088/0031-9155/54/9/001.

[81] S. Almquist, D. L. Parker, and D. A. Christensen, “Rapid full-wave phase aberration correction method for transcranial high-intensity focused ultrasound therapies,” *J. Ther. Ultrasound*, vol. 4, no. 1, p. 30, Dec. 2016, doi: 10.1186/s40349-016-0074-7.

[82] Y. Jing, F. C. Meral, and G. T. Clement, “Time-reversal transcranial ultrasound beam focusing using a k-space method,” *Phys. Med. Biol.*, vol. 57, no. 4, pp. 901–917, Jan. 2012, doi: 10.1088/0031-9155/57/4/901.

[83] G. W. Miller, M. Eames, J. Snell, and J.-F. Aubry, “Ultrashort echo-time MRI versus CT for skull aberration correction in MR-guided transcranial focused ultrasound: In vitro comparison on human calvaria,” *Med. Phys.*, vol. 42, no. 5, pp. 2223–2233, May 2015, doi: 10.1118/1.4916656.

[84] N. Lu *et al.*, “Two-step aberration correction: application to transcranial histotripsy,” *Phys. Med. Biol.*, vol. 67, no. 12, p. 125009, Jun. 2022, doi: 10.1088/1361-6560/ac72ed.

[85] P. Gélat, G. ter Haar, and N. Saffari, “A comparison of methods for focusing the field of a HIFU array transducer through human ribs,” *Phys. Med. Biol.*, vol. 59, no. 12, pp. 3139–3171, Jun. 2014, doi: 10.1088/0031-9155/59/12/3139.

[86] B. Quesson *et al.*, “A method for MRI guidance of intercostal high intensity focused ultrasound ablation in the liver,” *Med. Phys.*, vol. 37, no. 6Part1, pp. 2533–2540, Jun. 2010, doi: 10.1118/1.3413996.

[87] E. Cochard, C. Prada, J. F. Aubry, and M. Fink, “Ultrasonic focusing through the ribs using the DORT method,” *Med. Phys.*, vol. 36, no. 8, pp. 3495–3503, Aug. 2009, doi: 10.1118/1.3159755.

[88] J. R. Ballard, A. J. Casper, Y. Wan, and E. S. Ebbini, “Adaptive Transthoracic Refocusing of Dual-Mode Ultrasound Arrays,” *IEEE Trans. Biomed. Eng.*, vol. 57, no. 1, pp. 93–102, Jan. 2010, doi: 10.1109/TBME.2009.2028150.

[89] H.-L. Liu, H. Chang, W.-S. Chen, T.-C. Shih, J.-K. Hsiao, and W.-L. Lin, “Feasibility of transrib focused ultrasound thermal ablation for liver tumors using a spherically curved 2D array: A numerical study,” *Med. Phys.*, vol. 34, no. 9, pp. 3436–3448, 2007, doi: 10.1118/1.2759888.

[90] J.-F. Aubry, M. Pernot, F. Marquet, M. Tanter, and M. Fink, “Transcostal high-intensity-focused ultrasound: ex vivo adaptive focusing feasibility study,” *Phys. Med. Biol.*, vol. 53, no. 11, p. 2937, May 2008, doi: 10.1088/0031-9155/53/11/012.

[91] Y. Y. Botros, E. S. Ebbini, and J. L. Volakis, “Two-step hybrid virtual array ray (VAR) technique for focusing through the rib cage,” *IEEE Trans. Ultrason. Ferroelectr. Freq. Control*, vol. 45, no. 4, pp. 989–1000, Jul. 1998, doi: 10.1109/58.710577.

[92] H.-L. Liu, N. McDannold, and K. Hynynen, “Focal beam distortion and treatment planning in abdominal focused ultrasound surgery: Abdominal focused ultrasound surgery,” *Med. Phys.*, vol. 32, no. 5, pp. 1270–1280, Apr. 2005, doi: 10.1118/1.1895525.

[93] S. R. Haqshenas, P. Gélat, E. van ’t Wout, T. Betcke, and N. Saffari, “A fast full-wave solver for calculating ultrasound propagation in the body,” *Ultrasonics*, vol. 110, p. 106240, Feb. 2021, doi: 10.1016/j.ultras.2020.106240.

[94] S. A. Goss, R. L. Johnston, and F. Dunn, “Comprehensive compilation of empirical ultrasonic properties of mammalian tissues,” *J. Acoust. Soc. Am.*, vol. 64, no. 2, pp. 423–457, Aug. 1978, doi: 10.1121/1.382016.

[95] J. H. Oh, S. P. Choi, J. H. Wee, and J. H. Park, “Inter-scanner variability in Hounsfield unit measured by CT of the brain and effect on gray-to-white matter ratio,” *Am. J. Emerg. Med.*, vol. 37, no. 4, pp. 680–684, Apr. 2019, doi: 10.1016/j.ajem.2018.07.016.

[96] Y. Li, D. Robinson, and D. Carpenter, “Phase aberration correction using near-field signal redundancy. II. Experimental results,” *IEEE Trans. Ultrason. Ferroelectr. Freq. Control*, vol. 44, no. 2, pp. 372–379, Mar. 1997, doi: 10.1109/58.585121.

[97] K. Hynynen *et al.*, “500-element ultrasound phased array system for noninvasive focal surgery of the brain: A preliminary rabbit study with ex vivo human skulls,” *Magn. Reson. Med.*, vol. 52, no. 1, pp. 100–107, Jul. 2004, doi: 10.1002/mrm.20118.

[98] D. R. Daum, N. B. Smith, R. King, and K. Hynynen, “In vivo demonstration of noninvasive thermal surgery of the liver and kidney using an ultrasonic phased array,” *Ultrasound Med. Biol.*, vol. 25, no. 7, pp. 1087–1098, Sep. 1999, doi: 10.1016/S0301-5629(99)00053-8.

[99] H. Wang, E. S. Ebbini, M. O’Donnell, and C. A. Cain, “Phase aberration correction and motion compensation for ultrasonic hyperthermia phased arrays: experimental results,” *IEEE Trans. Ultrason. Ferroelectr. Freq. Control*, vol. 41, no. 1, pp. 34–43, Jan. 1994, doi: 10.1109/58.265818.

[100] R. J. McGough, M. L. Kessler, E. S. Ebbini, and C. A. Cain, “Treatment planning for hyperthermia with ultrasound phased arrays,” *IEEE Trans. Ultrason. Ferroelectr. Freq. Control*, vol. 43, no. 6, pp. 1074–1084, Nov. 1996, doi: 10.1109/58.542051.

[101] G. Montaldo, M. Tanter, and M. Fink, “Time Reversal of Speckle Noise,” *Phys. Rev. Lett.*, vol. 106, no. 5, p. 054301, Feb. 2011, doi: 10.1103/PhysRevLett.106.054301.

[102] R. Mallart and M. Fink, “The van Cittert–Zernike theorem in pulse echo measurements,” *J. Acoust. Soc. Am.*, vol. 90, no. 5, pp. 2718–2727, Nov. 1991, doi: 10.1121/1.401867.

[103] G. P. L. Thomas *et al.*, “Phase-Aberration Correction for HIFU Therapy Using a Multielement Array and Backscattering of Nonlinear Pulses,” *IEEE Trans. Ultrason. Ferroelectr. Freq. Control*, vol. 68, no. 4, pp. 1040–1050, Apr. 2021, doi: 10.1109/TUFFC.2020.3030890.

[104] C. R. Bawiec *et al.*, “Inertial Cavitation Behaviors Induced by Nonlinear Focused Ultrasound Pulses,” *IEEE Trans. Ultrason. Ferroelectr. Freq. Control*, vol. 68, no. 9, pp. 2884–2895, Sep. 2021, doi: 10.1109/TUFFC.2021.3073347.

[105] B. Zhang, G. F. Pinton, and K. R. Nightingale, “On the Relationship between Spatial Coherence and In Situ Pressure for Abdominal Imaging,” *Ultrasound Med. Biol.*, vol. 47, no. 8, pp. 2310–2320, Aug. 2021, doi: 10.1016/j.ultrasmedbio.2021.03.008.

[106] G. P. L. Thomas, T. D. Khokhlova, O. A. Sapozhnikov, Y.-N. Wang, S. Totten, and V. A. Khokhlova, “In Vivo Aberration Correction for Transcutaneous HIFU Therapy using a Multi-element Array,” *IEEE Trans. Ultrason. Ferroelectr. Freq. Control*, pp. 1–1, 2022, doi: 10.1109/TUFFC.2022.3200309.

[107] E. Herbert, M. Pernot, G. Montaldo, M. Fink, and M. Tanter, “Energy-based adaptive focusing of waves: application to noninvasive aberration correction of ultrasonic wavefields,” *IEEE Trans. Ultrason. Ferroelectr. Freq. Control*, vol. 56, no. 11, pp. 2388–2399, Nov. 2009, doi: 10.1109/TUFFc.2009.1327.

[108] G. R. Torr, “The acoustic radiation force,” *Am. J. Phys.*, vol. 52, no. 5, pp. 402–408, May 1984, doi: 10.1119/1.13625.

[109] K. Nightingale, R. Bentley, and G. Trahey, “Observations of Tissue Response to Acoustic Radiation Force: Opportunities for Imaging,” *Ultrason. Imaging*, vol. 24, no. 3, pp. 129–138, Jul. 2002, doi: 10.1177/016173460202400301.

[110] D. E. Soulioti, F. Santibanez, and G. Pinton, “Deconstruction and reconstruction of image-degrading effects in the human abdomen using Fullwave: phase aberration, multiple reverberation, and trailing reverberation,” 2021, doi: 10.48550/ARXIV.2106.13890.

[111] M. Pernot, G. Montaldo, M. Tanter, and M. Fink, “‘Ultrasonic stars’ for time-reversal focusing using induced cavitation bubbles,” *Appl. Phys. Lett.*, vol. 88, no. 3, p. 034102, Jan. 2006, doi: 10.1063/1.2162700.

[112] O. D. Kripfgans, J. B. Fowlkes, M. Woydt, O. P. Eldevik, and P. L. Carson, “In vivo droplet vaporization for occlusion therapy and phase aberration correction,” *IEEE Trans. Ultrason. Ferroelectr. Freq. Control*, vol. 49, no. 6, pp. 726–738, Jun. 2002, doi: 10.1109/TUFFC.2002.1009331.

[113] O. Couture, J.-F. Aubry, M. Tanter, and M. Fink, “Time-reversal focusing of therapeutic ultrasound on targeted microbubbles,” *Appl. Phys. Lett.*, vol. 94, no. 17, p. 173901, Apr. 2009, doi: 10.1063/1.3126039.

[114] Jongbum Seo, J. J. Choi, J. B. Fowlkes, M. O’Donnell, and C. A. Cain, “Aberration correction by nonlinear beam mixing: generation of a pseudo point sound source,” *IEEE Trans. Ultrason. Ferroelectr. Freq. Control*, vol. 52, no. 11, pp. 1970–1980, Nov. 2005, doi: 10.1109/TUFFC.2005.1561666.

[115] J. D. Rojas and P. A. Dayton, “Optimizing Acoustic Activation of Phase Change Contrast Agents With the Activation Pressure Matching Method: A Review,” *IEEE Trans. Ultrason. Ferroelectr. Freq. Control*, vol. 64, no. 1, pp. 264–272, Jan. 2017, doi: 10.1109/TUFFC.2016.2616304.

[116] B. D. Lindsey, H. A. Nicoletto, E. R. Bennett, D. T. Laskowitz, and S. W. Smith, “3-D Transcranial Ultrasound Imaging with Bilateral Phase Aberration Correction of Multiple Isoplanatic Patches: A Pilot Human Study with Microbubble Contrast Enhancement,” *Ultrasound Med. Biol.*, vol. 40, no. 1, pp. 90–101, Jan. 2014, doi: 10.1016/j.ultrasmedbio.2013.09.006.

[117] P. S. Sheeran and P. A. Dayton, “Phase-Change Contrast Agents for Imaging and Therapy,” *Curr. Pharm. Des.*, vol. 18, no. 15, pp. 2152–2165, Mar. 2012, doi: 10.2174/138161212800099883.

[118] P. S. Sheeran *et al.*, “Decafluorobutane as a Phase-Change Contrast Agent for Low-Energy Extravascular Ultrasonic Imaging,” *Ultrasound Med. Biol.*, vol. 37, no. 9, pp. 1518–1530, Sep. 2011, doi: 10.1016/j.ultrasmedbio.2011.05.021.

[119] D. Psychoudakis, J. B. Fowlkes, J. L. Volakis, and P. L. Carson, “Potential of microbubbles for use as point targets in phase aberration correction,” *IEEE Trans. Ultrason. Ferroelectr. Freq. Control*, vol. 51, no. 12, pp. 1639–1648, Dec. 2004, doi: 10.1109/TUFFC.2004.1386681.

[120] K. J. Haworth, J. B. Fowlkes, P. L. Carson, and O. D. Kripfgans, “Towards Aberration Correction of Transcranial Ultrasound Using Acoustic Droplet Vaporization,” *Ultrasound Med. Biol.*, vol. 34, no. 3, pp. 435–445, Mar. 2008, doi: 10.1016/j.ultrasmedbio.2007.08.004.

[121] C. Demené *et al.*, “Spatiotemporal Clutter Filtering of Ultrafast Ultrasound Data Highly Increases Doppler and fUltrasound Sensitivity,” *IEEE Trans. Med. Imaging*, vol. 34, no. 11, pp. 2271–2285, Nov. 2015, doi: 10.1109/TMI.2015.2428634.

[122] D. E. Soulioti, D. Espíndola, P. A. Dayton, and G. F. Pinton, “Super-Resolution Imaging Through the Human Skull,” *IEEE Trans. Ultrason. Ferroelectr. Freq. Control*, vol. 67, no. 1, pp. 25–36, Jan. 2020, doi: 10.1109/TUFFC.2019.2937733.

[123] M. A. O'Reilly and K. Hynynen, “A super-resolution ultrasound method for brain vascular mapping,” *Med. Phys.*, vol. 40, no. 11, p. 110701, Nov. 2013, doi: 10.1118/1.4823762.

[124] R. M. Jones *et al.*, "Echo-Focusing in Transcranial Focused Ultrasound Thalamotomy for Essential Tremor: A Feasibility Study," *Mov. Disord.*, vol. 35, no. 12, pp. 2327–2333, Dec. 2020, doi: 10.1002/mds.28226.
[125] J. Robin *et al.*, "In vivo adaptive focusing for clinical contrast-enhanced transcranial ultrasound imaging in human," *Phys. Med. Biol.*, vol. 68, no. 2, p. 025019, Jan. 2023, doi: 10.1088/1361-6560/acabfb.
[126] N. M. Ivancevich, G. F. Pinton, H. A. Nicoletto, E. Bennett, D. T. Laskowitz, and S. W. Smith, "Real-Time 3-D Contrast-Enhanced Transcranial Ultrasound and Aberration Correction," *Ultrasound Med. Biol.*, vol. 34, no. 9, pp. 1387–1395, Sep. 2008, doi: 10.1016/j.ultrasmedbio.2008.01.015.
[127] M. L. Fabiilli, K. J. Haworth, N. H. Fakhri, O. D. Kripfgans, P. L. Carson, and J. B. Fowlkes, "The role of inertial cavitation in acoustic droplet vaporization," *IEEE Trans. Ultrason. Ferroelectr. Freq. Control*, vol. 56, no. 5, pp. 1006–1017, May 2009, doi: 10.1109/TUFFC.2009.1132.
[128] T. G. Leighton, *The acoustic bubble*. San Diego, United States: Academic Press, 1994.
[129] P. Zhong, I. Cioanta, F. H. Cocks, and G. M. Preminger, "Inertial cavitation and associated acoustic emission produced during electrohydraulic shock wave lithotripsy," *J. Acoust. Soc. Am.*, vol. 101, no. 5, pp. 2940–2950, May 1997, doi: 10.1121/1.418522.
[130] K. Johnston *et al.*, "Periodic shock-emission from acoustically driven cavitation clouds: A source of the subharmonic signal," *Ultrasonics*, vol. 54, no. 8, pp. 2151–2158, Dec. 2014, doi: 10.1016/j.ultras.2014.06.011.
[131] J. R. Sukovich, J. J. Macoskey, J. E. Lundt, T. I. Gerhardson, T. L. Hall, and Z. Xu, "Real-Time Transcranial Histotripsy Treatment Localization and Mapping Using Acoustic Cavitation Emission Feedback," *IEEE Trans. Ultrason. Ferroelectr. Freq. Control*, vol. 67, no. 6, pp. 1178–1191, Jun. 2020, doi: 10.1109/TUFFC.2020.2967586.
[132] W. Lauterborn and A. Vogel, "Shock Wave Emission by Laser Generated Bubbles," in *Bubble Dynamics and Shock Waves*, C. F. Delale, Ed., Berlin, Heidelberg: Springer Berlin Heidelberg, 2013, pp. 67–103. doi: 10.1007/978-3-642-34297-4_3.
[133] J. Gateau, L. Marsac, M. Pernot, J.-F. Aubry, M. Tanter, and M. Fink, "Transcranial Ultrasonic Therapy Based on Time Reversal of Acoustically Induced Cavitation Bubble Signature," *IEEE Trans. Biomed. Eng.*, vol. 57, no. 1, pp. 134–144, Jan. 2010, doi: 10.1109/TBME.2009.2031816.
[134] J. J. Macoskey *et al.*, "Soft-Tissue Aberration Correction for Histotripsy," *IEEE Trans. Ultrason. Ferroelectr. Freq. Control*, vol. 65, no. 11, pp. 2073–2085, Nov. 2018, doi: 10.1109/TUFFC.2018.2872727.
[135] G. Wu, J. Wu, B. Wang, X. Zhu, X. Shi, and Y. Ding, "Importance of tumor size at diagnosis as a prognostic factor for hepatocellular carcinoma survival: a population-based study," *Cancer Manag. Res.*, vol. Volume 10, pp. 4401–4410, Oct. 2018, doi: 10.2147/CMAR.S177663.
[136] J. E. Lundt, S. P. Allen, J. Shi, T. L. Hall, C. A. Cain, and Z. Xu, "Non-invasive, Rapid Ablation of Tissue Volume Using Histotripsy," *Ultrasound Med. Biol.*, vol. 43, no. 12, pp. 2834–2847, 2017, doi: 10.1016/j.ultrasmedbio.2017.08.006.
[137] J. J. Macoskey *et al.*, "Using the cavitation collapse time to indicate the extent of histotripsy-induced tissue fractionation," *Phys. Med. Biol.*, vol. 63, no. 5, 2018, doi: 10.1088/1361-6560/aaae3b.
[138] K. A. Mørch, "On the Collapse of Cavity Clusters in Flow Cavitation," in *Cavitation and Inhomogeneities in Underwater Acoustics*, W. Lauterborn, Ed., Berlin, Heidelberg: Springer Berlin Heidelberg, 1980, pp. 95–100.
[139] Y. C. Wang and C. E. Brennen, "Shock Wave Development in the Collapse of a Cloud of Bubbles," in *Cavitation and Multiphase Flow*, vol. 194, in Fluids Engineering Division, vol. 194. , New York, NY: American Society of Mechanical Engineers, 1994, pp. 15–19. [Online]. Available: https://resolver.caltech.edu/CaltechAUTHORS:WNGcmpf94

[140] D. Ogloblina, S. J. Schmidt, and N. A. Adams, “Simulation and analysis of collapsing vapor-bubble clusters with special emphasis on potentially erosive impact loads at walls,” *EPJ Web Conf.*, vol. 180, p. 02079, 2018, doi: 10.1051/epjconf/201818002079.
[141] C. R. Dillon, A. Farrer, H. McLean, S. Almquist, D. Christensen, and A. Payne, “Experimental assessment of phase aberration correction for breast MRgFUS therapy,” *Int. J. Hyperthermia*, vol. 34, no. 6, pp. 731–743, Aug. 2018, doi: 10.1080/02656736.2017.1422029.
[142] A. T. Peek *et al.*, “Bilayer aberration-inducing gel phantom for high intensity focused ultrasound applications,” *J. Acoust. Soc. Am.*, vol. 148, no. 6, pp. 3569–3580, Dec. 2020, doi: 10.1121/10.0002877.
[143] Z. Dong, H. Zheng, Q. Zhu, and Y. Wang, “Focus prediction of high-intensity focused ultrasound (HIFU) in biological tissues based on magnetic resonance images,” *Appl. Acoust.*, vol. 197, p. 108927, Aug. 2022, doi: 10.1016/j.apacoust.2022.108927.
[144] L. M. Hinkelman, D. Liu, R. C. Waag, Q. Zhu, and B. D. Steinberg, “Measurement and correction of ultrasonic pulse distortion produced by the human breast,” *J. Acoust. Soc. Am.*, vol. 97, no. 3, pp. 1958–1969, Mar. 1995, doi: 10.1121/1.412069.
[145] A. S. Bobina, P. B. Rosnitskiy, T. D. Khokhlova, P. V. Yuldashev, and V. A. Khokhlova, “Effect of Abdominal Wall Inhomogeneities on the Focusing of an Ultrasonic Beam at Different Positions of the Transducer,” *Bull. Russ. Acad. Sci. Phys.*, vol. 85, no. 6, pp. 675–680, Jun. 2021, doi: 10.3103/S1062873821060058.
[146] J. Gu and Y. Jing, “Modeling of wave propagation for medical ultrasound: a review,” *IEEE Trans. Ultrason. Ferroelectr. Freq. Control*, vol. 62, no. 11, pp. 1979–1992, Nov. 2015, doi: 10.1109/TUFFC.2015.007034.
[147] G. E. Stocker *et al.*, “A Modular, Kerf-Minimizing Approach for Therapeutic Ultrasound Phased Array Construction,” *IEEE Trans. Ultrason. Ferroelectr. Freq. Control*, vol. PP, 2022, doi: 10.1109/TUFFC.2022.3178291.
[148] Bradley E. Treeby and Benjamin T. Cox, “k-Wave: MATLAB toolbox for the simulation and reconstruction of photoacoustic wave fields,” *J. Biomed. Opt.*, vol. 15, no. 2, pp. 1–12, Mar. 2010, doi: 10.1117/1.3360308.
[149] B. E. Treeby and B. T. Cox, “Modeling power law absorption and dispersion for acoustic propagation using the fractional Laplacian,” *J. Acoust. Soc. Am.*, vol. 127, no. 5, pp. 2741–2748, May 2010, doi: 10.1121/1.3377056.
[150] M. Tabei, T. D. Mast, and R. C. Waag, “A k-space method for coupled first-order acoustic propagation equations,” *J. Acoust. Soc. Am.*, vol. 111, no. 1, pp. 53–63, Jan. 2002, doi: 10.1121/1.1421344.
[151] W. T. Dixon, “Simple proton spectroscopic imaging.,” *Radiology*, vol. 153, no. 1, pp. 189–194, Oct. 1984, doi: 10.1148/radiology.153.1.6089263.
[152] M. Fink *et al.*, “Time-reversed acoustics,” *Rep. Prog. Phys.*, vol. 63, no. 12, pp. 1933–1995, Dec. 2000, doi: 10.1088/0034-4885/63/12/202.
[153] K. Clark *et al.*, “The Cancer Imaging Archive (TCIA): Maintaining and Operating a Public Information Repository,” *J. Digit. Imaging*, vol. 26, no. 6, pp. 1045–1057, Dec. 2013, doi: 10.1007/s10278-013-9622-7.
[154] H. R. Roth *et al.*, “A New 2.5D Representation for Lymph Node Detection Using Random Sets of Deep Convolutional Neural Network Observations,” in *Medical Image Computing and Computer-Assisted Intervention – MICCAI 2014*, vol. 8673, P. Golland, N. Hata, C. Barillot, J. Hornegger, and R. Howe, Eds., in Lecture Notes in Computer Science, vol. 8673. , Cham: Springer International Publishing, 2014, pp. 520–527. doi: 10.1007/978-3-319-10404-1_65.
[155] H. Roth *et al.*, “A new 2.5 D representation for lymph node detection in CT.” The Cancer Imaging Archive, 2015. doi: 10.7937/K9/TCIA.2015.AQIIDCNM.

[156] A. Seff *et al.*, "2D View Aggregation for Lymph Node Detection Using a Shallow Hierarchy of Linear Classifiers," in *Medical Image Computing and Computer-Assisted Intervention – MICCAI 2014*, vol. 8673, P. Golland, N. Hata, C. Barillot, J. Hornegger, and R. Howe, Eds., in Lecture Notes in Computer Science, vol. 8673. , Cham: Springer International Publishing, 2014, pp. 544–552. doi: 10.1007/978-3-319-10404-1_68.

[157] A. Seff, L. Lu, A. Barbu, H. Roth, H.-C. Shin, and R. M. Summers, "Leveraging Mid-Level Semantic Boundary Cues for Automated Lymph Node Detection," in *Medical Image Computing and Computer-Assisted Intervention -- MICCAI 2015*, vol. 9350, N. Navab, J. Hornegger, W. M. Wells, and A. Frangi, Eds., in Lecture Notes in Computer Science, vol. 9350. , Cham: Springer International Publishing, 2015, pp. 53–61. doi: 10.1007/978-3-319-24571-3_7.

[158] T. J. S. Van Mulder *et al.*, "High frequency ultrasound to assess skin thickness in healthy adults," *Vaccine*, vol. 35, no. 14, pp. 1810–1815, Mar. 2017, doi: 10.1016/j.vaccine.2016.07.039.

[159] R. N. Baumgartner, S. B. Heymsfield, A. F. Roche, and M. Bernardino, "Abdominal composition quantified by computed tomography," *Am. J. Clin. Nutr.*, vol. 48, no. 4, pp. 936–945, Oct. 1988, doi: 10.1093/ajcn/48.4.936.

[160] N. Mitsiopoulos, R. N. Baumgartner, S. B. Heymsfield, W. Lyons, D. Gallagher, and R. Ross, "Cadaver validation of skeletal muscle measurement by magnetic resonance imaging and computerized tomography," *J. Appl. Physiol.*, vol. 85, no. 1, pp. 115–122, Jul. 1998, doi: 10.1152/jappl.1998.85.1.115.

[161] K. Engelke, O. Museyko, L. Wang, and J.-D. Laredo, "Quantitative analysis of skeletal muscle by computed tomography imaging—State of the art," *Orthop. Imaging Transl. Res. Clin. Appl.*, vol. 15, pp. 91–103, Oct. 2018, doi: 10.1016/j.jot.2018.10.004.

[162] A. B. Holbrook and K. B. Pauly, "Segmentation of Costal Cartilage in Abdominal CT Data using Watershed Markers," *AIP Conf. Proc.*, vol. 911, no. 1, pp. 226–231, May 2007, doi: 10.1063/1.2744277.

[163] Y. Chen, Z. Wang, J. Hu, W. Zhao, and Q. Wu, "The domain knowledge based graph-cut model for liver CT segmentation," *Biomed. Image Restor. Enhanc.*, vol. 7, no. 6, pp. 591–598, Nov. 2012, doi: 10.1016/j.bspc.2012.04.005.

[164] W. Marczak, "Water as a standard in the measurements of speed of sound in liquids," *J. Acoust. Soc. Am.*, vol. 102, no. 5, pp. 2776–2779, Nov. 1997, doi: 10.1121/1.420332.

[165] F. E. Jones and G. L. Harris, "ITS-90 Density of Water Formulation for Volumetric Standards Calibration," *J. Res. Natl. Inst. Stand. Technol.*, vol. 97, no. 3, pp. 335–340, 1992, doi: 10.6028/jres.097.013.

[166] J. M. M. Pinkerton, "The Absorption of Ultrasonic Waves in Liquids and its Relation to Molecular Constitution," *Proc. Phys. Soc. Sect. B*, vol. 62, no. 2, pp. 129–141, Feb. 1949, doi: 10.1088/0370-1301/62/2/307.

[167] K. B. Bader, E. Vlaisavljevich, and A. D. Maxwell, "For Whom the Bubble Grows: Physical Principles of Bubble Nucleation and Dynamics in Histotripsy Ultrasound Therapy," *Ultrasound Med. Biol.*, vol. 45, no. 5, pp. 1056–1080, May 2019, doi: 10.1016/j.ultrasmedbio.2018.10.035.

[168] B. E. Treeby, J. Jaros, A. P. Rendell, and B. T. Cox, "Modeling nonlinear ultrasound propagation in heterogeneous media with power law absorption using a *k* -space pseudospectral method," *J. Acoust. Soc. Am.*, vol. 131, no. 6, pp. 4324–4336, Jun. 2012, doi: 10.1121/1.4712021.

[169] J. Koskela, E. Vahala, M. de Greef, L. P. Lafitte, and M. Ries, "Stochastic ray tracing for simulation of high intensity focal ultrasound therapy," *J. Acoust. Soc. Am.*, vol. 136, no. 3, pp. 1430–1440, Sep. 2014, doi: 10.1121/1.4892768.

[170] J. Robertson, E. Martin, B. Cox, and B. E. Treeby, "Sensitivity of simulated transcranial ultrasound fields to acoustic medium property maps," *Phys. Med. Biol.*, vol. 62, no. 7, pp. 2559–2580, Mar. 2017, doi: 10.1088/1361-6560/aa5e98.

[171] H. Montanaro *et al.*, "The impact of CT image parameters and skull heterogeneity modeling on the accuracy of transcranial focused ultrasound simulations," *J. Neural Eng.*, vol. 18, no. 4, p. 046041, May 2021, doi: 10.1088/1741-2552/abf68d.
[172] T. M. Wah *et al.*, "A Multi-centre, Single Arm, Non-randomized, Prospective European Trial to Evaluate the Safety and Efficacy of the HistoSonics System in the Treatment of Primary and Metastatic Liver Cancers (#HOPE4LIVER)," *Cardiovasc. Intervent. Radiol.*, vol. 46, no. 2, pp. 259–267, Feb. 2023, doi: 10.1007/s00270-022-03309-6.
[173] J. Civale, R. Clarke, I. Rivens, and G. ter Haar, "The use of a segmented transducer for rib sparing in HIFU treatments," *Ultrasound Med. Biol.*, vol. 32, no. 11, pp. 1753–1761, Nov. 2006, doi: 10.1016/j.ultrasmedbio.2006.06.005.
[174] L. Sibulesky, "Normal liver anatomy," *Clin. Liver Dis.*, vol. 2, no. S1, pp. S1–S3, Mar. 2013, doi: 10.1002/cld.124.
[175] M. T. Sellers, "Liver," in *Surgical Anatomy and Technique: A Pocket Manual*, L. J. Skandalakis, Ed., Cham: Springer International Publishing, 2021, pp. 551–592. doi: 10.1007/978-3-030-51313-9_13.
[176] P. B. Rosnitskiy, B. A. Vysokanov, L. R. Gavrilov, O. A. Sapozhnikov, and V. A. Khokhlova, "Method for Designing Multielement Fully Populated Random Phased Arrays for Ultrasound Surgery Applications," *IEEE Trans. Ultrason. Ferroelectr. Freq. Control*, vol. 65, no. 4, pp. 630–637, Apr. 2018, doi: 10.1109/TUFFC.2018.2800160.
[177] K. Firouzi, B. T. Cox, B. E. Treeby, and N. Saffari, "A first-order k-space model for elastic wave propagation in heterogeneous media," *J. Acoust. Soc. Am.*, vol. 132, no. 3, pp. 1271–1283, Sep. 2012, doi: 10.1121/1.4730897.
[178] E. S. Wise, B. T. Cox, J. Jaros, and B. E. Treeby, "Representing arbitrary acoustic source and sensor distributions in Fourier collocation methodsa)," *J. Acoust. Soc. Am.*, vol. 146, no. 1, pp. 278–288, Jul. 2019, doi: 10.1121/1.5116132.
[179] E. Martin, Y. T. Ling, and B. E. Treeby, "Simulating Focused Ultrasound Transducers Using Discrete Sources on Regular Cartesian Grids," *IEEE Trans. Ultrason. Ferroelectr. Freq. Control*, vol. 63, no. 10, pp. 1535–1542, Oct. 2016, doi: 10.1109/TUFFC.2016.2600862.
[180] R. A. Drainville, L. Curiel, and S. Pichardo, "Superposition method for modelling boundaries between media in viscoelastic finite difference time domain simulations," *J. Acoust. Soc. Am.*, vol. 146, no. 6, pp. 4382–4401, Dec. 2019, doi: 10.1121/1.5139221.
[181] H. P. Kok *et al.*, "Treatment planning facilitates clinical decision making for hyperthermia treatments," *Int. J. Hyperthermia*, vol. 38, no. 1, pp. 532–551, Jan. 2021, doi: 10.1080/02656736.2021.1903583.
[182] K.-W. Lin *et al.*, "Histotripsy beyond the intrinsic cavitation threshold using very short ultrasound pulses: microtripsy," *IEEE Trans. Ultrason. Ferroelectr. Freq. Control*, vol. 61, no. 2, pp. 251–265, Feb. 2014, doi: 10.1109/TUFFC.2014.6722611.
[183] E. Vlaisavljevich *et al.*, "Effects of Ultrasound Frequency and Tissue Stiffness on the Histotripsy Intrinsic Threshold for Cavitation," *Ultrasound Med. Biol.*, vol. 41, no. 6, pp. 1651–1667, 2015, doi: 10.1016/j.ultrasmedbio.2015.01.028.
[184] M. S. Plesset, "Shockwaves from Cavity Collapse," *Philos. Trans. R. Soc. Lond. Ser. Math. Phys. Sci.*, vol. 260, no. 1110, pp. 241–244, 1966.
[185] G. E. Reisman, Y.-C. Wang, and C. E. Brennen, "Observations of shock waves in cloud cavitation," *J. Fluid Mech.*, vol. 355, pp. 255–283, 1998, doi: 10.1017/S0022112097007830.
[186] E. A. Brujan, T. Ikeda, and Y. Matsumoto, "Jet formation and shock wave emission during collapse of ultrasound-induced cavitation bubbles and their role in the therapeutic applications of high-intensity focused ultrasound," *Phys. Med. Biol.*, vol. 50, no. 20, pp. 4797–4809, Sep. 2005, doi: 10.1088/0031-9155/50/20/004.

[187] K. Johnston *et al.*, “Periodic shock-emission from acoustically driven cavitation clouds: A source of the subharmonic signal,” *Ultrasonics*, vol. 54, no. 8, pp. 2151–2158, Dec. 2014, doi: 10.1016/j.ultras.2014.06.011.
[188] E. Vlaisavljevich *et al.*, “Effects of Ultrasound Frequency and Tissue Stiffness on the Histotripsy Intrinsic Threshold for Cavitation,” *Ultrasound Med. Biol.*, vol. 41, no. 6, pp. 1651–1667, Jun. 2015, doi: 10.1016/j.ultrasmedbio.2015.01.028.
[189] M. Fink and C. Prada, “Acoustic time-reversal mirrors,” *Inverse Probl.*, vol. 17, no. 1, pp. R1–R38, Jan. 2001, doi: 10.1088/0266-5611/17/1/201.
[190] E. Vlaisavljevich, T. Gerhardson, T. Hall, and Z. Xu, “Effects of f-number on the histotripsy intrinsic threshold and cavitation bubble cloud behavior,” *Phys. Med. Biol.*, vol. 62, no. 4, pp. 1269–1290, Jan. 2017, doi: 10.1088/1361-6560/aa54c7.
[191] T. Khokhlova *et al.*, “Dependence of inertial cavitation induced by high intensity focused ultrasound on transducer F-number and nonlinear waveform distortion,” *J. Acoust. Soc. Am.*, vol. 144, no. 3, pp. 1160–1169, Sep. 2018, doi: 10.1121/1.5052260.
[192] D. Wu *et al.*, “Amplitude and phase relation of harmonics in nonlinear focused ultrasound,” *AIP Adv.*, vol. 12, no. 6, p. 065317, Jun. 2022, doi: 10.1063/5.0096071.
[193] E. Yeats, D. Gupta, Z. Xu, and T. L. Hall, “Effects of phase aberration on transabdominal focusing for a large aperture, low f-number histotripsy transducer,” *Phys. Med. Biol.*, vol. 67, no. 15, p. 155004, Jul. 2022, doi: 10.1088/1361-6560/ac7d90.
[194] T. N. Nguyen, M. N. Do, and M. L. Oelze, “Visualization of the Intensity Field of a Focused Ultrasound Source In Situ,” *IEEE Trans. Med. Imaging*, vol. 38, no. 1, pp. 124–133, Jan. 2019, doi: 10.1109/TMI.2018.2857481.
[195] M. Thies and M. L. Oelze, “Combined Therapy Planning, Real-Time Monitoring, and Low Intensity Focused Ultrasound Treatment Using a Diagnostic Imaging Array,” *IEEE Trans. Med. Imaging*, vol. 41, no. 6, pp. 1410–1419, Jun. 2022, doi: 10.1109/TMI.2021.3140176.
[196] M. Thies and M. L. Oelze, “Real-Time Visualization of a Focused Ultrasound Beam Using Ultrasonic Backscatter,” *IEEE Trans. Ultrason. Ferroelectr. Freq. Control*, vol. 68, no. 4, pp. 1213–1223, Apr. 2021, doi: 10.1109/TUFFC.2020.3035784.
[197] X. Zhou *et al.*, “Acoustic Beam Mapping for Guiding HIFU Therapy In Vivo Using Sub-Therapeutic Sound Pulse and Passive Beamforming,” *IEEE Trans. Biomed. Eng.*, vol. 69, no. 5, pp. 1663–1673, May 2022, doi: 10.1109/TBME.2021.3126734.
[198] M. G. Wagner *et al.*, “An X-ray C-arm Guided Automatic Targeting System for Histotripsy,” *IEEE Trans. Biomed. Eng.*, pp. 1–12, 2022, doi: 10.1109/TBME.2022.3198600.
[199] J. Long, W. Long, N. Bottenus, and G. Trahey, “Coherence-based quantification of acoustic clutter sources in medical ultrasound,” *J. Acoust. Soc. Am.*, vol. 148, no. 2, pp. 1051–1062, Aug. 2020, doi: 10.1121/10.0001790.
[200] M. A. Lediju, M. J. Pihl, J. J. Dahl, and G. E. Trahey, “Quantitative Assessment of the Magnitude, Impact and Spatial Extent of Ultrasonic Clutter,” *Ultrason. Imaging*, vol. 30, no. 3, pp. 151–168, Jul. 2008, doi: 10.1177/016173460803000302.
[201] E. Yeats, N. Lu, J. R. Sukovich, Z. Xu, and T. L. Hall, “Soft Tissue Aberration Correction for Histotripsy Using Acoustic Emissions From Cavitation Cloud Nucleation and Collapse,” *Ultrasound Med. Biol.*, vol. 49, no. 5, pp. 1182–1193, May 2023, doi: 10.1016/j.ultrasmedbio.2023.01.004.
[202] J. J. Macoskey *et al.*, “Using the cavitation collapse time to indicate the extent of histotripsy-induced tissue fractionation,” *Phys. Med. Biol.*, vol. 63, no. 5, p. 055013, Mar. 2018, doi: 10.1088/1361-6560/aaae3b.
[203] S. C. Haskell, N. Lu, G. E. Stocker, Z. Xu, and J. R. Sukovich, “Monitoring cavitation dynamics evolution in tissue mimicking hydrogels for repeated exposures via acoustic cavitation emissions,” *J. Acoust. Soc. Am.*, vol. 153, no. 1, pp. 237–247, Jan. 2023, doi: 10.1121/10.0016849.

[204] Pai-Chi Li and Meng-Lin Li, "Adaptive imaging using the generalized coherence factor," *IEEE Trans. Ultrason. Ferroelectr. Freq. Control*, vol. 50, no. 2, pp. 128–141, Feb. 2003, doi: 10.1109/TUFFC.2003.1182117.
[205] J. Camacho, M. Parrilla, and C. Fritsch, "Phase Coherence Imaging," *IEEE Trans. Ultrason. Ferroelectr. Freq. Control*, vol. 56, no. 5, pp. 958–974, May 2009, doi: 10.1109/TUFFC.2009.1128.
[206] M. A. Lediju, G. E. Trahey, B. C. Byram, and J. J. Dahl, "Short-lag spatial coherence of backscattered echoes: imaging characteristics," *IEEE Trans. Ultrason. Ferroelectr. Freq. Control*, vol. 58, no. 7, pp. 1377–1388, Jul. 2011, doi: 10.1109/TUFFC.2011.1957.
[207] M. A. Lediju Bell, R. Goswami, J. A. Kisslo, J. J. Dahl, and G. E. Trahey, "Short-Lag Spatial Coherence Imaging of Cardiac Ultrasound Data: Initial Clinical Results," *Ultrasound Med. Biol.*, vol. 39, no. 10, pp. 1861–1874, Oct. 2013, doi: 10.1016/j.ultrasmedbio.2013.03.029.
[208] C. Prada and M. Fink, "Eigenmodes of the time reversal operator: A solution to selective focusing in multiple-target media," *Wave Motion*, vol. 20, no. 2, pp. 151–163, Sep. 1994, doi: 10.1016/0165-2125(94)90039-6.
[209] C. Prada, S. Manneville, D. Spoliansky, and M. Fink, "Decomposition of the time reversal operator: Detection and selective focusing on two scatterers," *J. Acoust. Soc. Am.*, vol. 99, no. 4, pp. 2067–2076, Apr. 1996, doi: 10.1121/1.415393.
[210] M. Gyongy and C. -C. Coussios, "Passive Spatial Mapping of Inertial Cavitation During HIFU Exposure," *IEEE Trans. Biomed. Eng.*, vol. 57, no. 1, pp. 48–56, Jan. 2010, doi: 10.1109/TBME.2009.2026907.
[211] V. Zderic, A. Keshavarzi, M. A. Andrew, S. Vaezy, and R. W. Martin, "Attenuation of porcine tissues in vivo after high-intensity ultrasound treatment," *Ultrasound Med. Biol.*, vol. 30, no. 1, pp. 61–66, Jan. 2004, doi: 10.1016/j.ultrasmedbio.2003.09.003.
[212] J. E. Lundt, S. P. Allen, J. Shi, T. L. Hall, C. A. Cain, and Z. Xu, "Non-invasive, Rapid Ablation of Tissue Volume Using Histotripsy," *Ultrasound Med. Biol.*, vol. 43, no. 12, pp. 2834–2847, Dec. 2017, doi: 10.1016/j.ultrasmedbio.2017.08.006.
[213] W. C. Pilkington, "Isoplanatic patch size for aberration correction in ultrasonic imaging," Ph.D., University of Rochester, United States -- New York, 2005. [Online]. Available: https://proxy.lib.umich.edu/login?url=https://www.proquest.com/dissertations-theses/isoplanatic-patch-size-aberration-correction/docview/305429726/se-2?accountid=14667
[214] J. J. Cerrolaza, N. Safdar, E. Biggs, J. Jago, C. A. Peters, and M. G. Linguraru, "Renal Segmentation From 3D Ultrasound via Fuzzy Appearance Models and Patient-Specific Alpha Shapes," *IEEE Trans. Med. Imaging*, vol. 35, no. 11, pp. 2393–2402, Nov. 2016, doi: 10.1109/TMI.2016.2572641.
[215] M. Marsousi, K. N. Plataniotis, and S. Stergiopoulos, "An Automated Approach for Kidney Segmentation in Three-Dimensional Ultrasound Images," *IEEE J. Biomed. Health Inform.*, vol. 21, no. 4, pp. 1079–1094, Jul. 2017, doi: 10.1109/JBHI.2016.2580040.
[216] G. P. L. Thomas, T. D. Khokhlova, and V. A. Khokhlova, "Partial Respiratory Motion Compensation for Abdominal Extracorporeal Boiling Histotripsy Treatments With a Robotic Arm," *IEEE Trans. Ultrason. Ferroelectr. Freq. Control*, vol. 68, no. 9, pp. 2861–2870, Sep. 2021, doi: 10.1109/TUFFC.2021.3075938.
[217] Z. Xu, J. B. Fowlkes, E. D. Rothman, A. M. Levin, and C. A. Cain, "Controlled ultrasound tissue erosion: The role of dynamic interaction between insonation and microbubble activity," *J. Acoust. Soc. Am.*, vol. 117, no. 1, pp. 424–435, Jan. 2005, doi: 10.1121/1.1828551.
[218] T. Khokhlova, A. Maxwell, W. Kreider, V. Khokhlova, M. O'Donnell, and O. Sapozhnikov, "A method for phase aberration correction of high intensity focused ultrasound fields using acoustic nonlinearity," *J. Acoust. Soc. Am.*, vol. 140, no. 4_Supplement, pp. 3083–3083, Oct. 2016, doi: 10.1121/1.4969607.

[219] P. B. Fellgett, E. H. Linfoot, and R. O. Redman, “On the assessment of optical images,” *Philos. Trans. R. Soc. Lond. Ser. Math. Phys. Sci.*, vol. 247, no. 931, pp. 369–407, Jan. 1997, doi: 10.1098/rsta.1955.0001.

[220] B. D. de Senneville, C. Moonen, and M. Ries, “MRI-Guided HIFU Methods for the Ablation of Liver and Renal Cancers,” in *Therapeutic Ultrasound*, J.-M. Escoffre and A. Bouakaz, Eds., in Advances in Experimental Medicine and Biology. , Cham: Springer International Publishing, 2016, pp. 43–63. doi: 10.1007/978-3-319-22536-4_3.

[221] E. S. Worm, M. Høyer, W. Fledelius, and P. R. Poulsen, “Three-dimensional, time-resolved, intrafraction motion monitoring throughout stereotactic liver radiation therapy on a conventional linear accelerator,” *Int. J. Radiat. Oncol. Biol. Phys.*, vol. 86, no. 1, pp. 190–197, 2013, doi: 10.1016/j.ijrobp.2012.12.017.

[222] F. Marquet, J. F. Aubry, M. Pernot, M. Fink, and M. Tanter, “Optimal transcostal high-intensity focused ultrasound with combined real-time 3D movement tracking and correction,” *Phys. Med. Biol.*, vol. 56, no. 22, pp. 7061–7080, 2011, doi: 10.1088/0031-9155/56/22/005.

[223] P. J. Bryan, S. Custar, J. R. Haaga, and V. Balsara, “Respiratory movement of the pancreas: An ultrasonic study,” *J. Ultrasound Med.*, vol. 3, no. 7, pp. 317–320, 1984, doi: 10.7863/jum.1984.3.7.317.

[224] W. Kreider *et al.*, “Characterization of a multi-element clinical HIFU system using acoustic holography and nonlinear modeling,” *IEEE Trans. Ultrason. Ferroelectr. Freq. Control*, vol. 60, no. 8, pp. 1683–1698, Aug. 2013, doi: 10.1109/TUFFC.2013.2750.

[225] P. V. Yuldashev, M. M. Karzova, W. Kreider, P. B. Rosnitskiy, O. A. Sapozhnikov, and V. A. Khokhlova, “‘HIFU Beam:’ A Simulator for Predicting Axially Symmetric Nonlinear Acoustic Fields Generated by Focused Transducers in a Layered Medium,” *IEEE Trans. Ultrason. Ferroelectr. Freq. Control*, vol. 68, no. 9, pp. 2837–2852, Sep. 2021, doi: 10.1109/TUFFC.2021.3074611.

[226] B. Treeby, B. Cox, and J. Jaros, “k-Wave, A MATLAB toolbox for the time domain simulation of acoustic wave fields; User Manual Version 1.1.” Aug. 27, 2016. Accessed: Nov. 03, 2023. [Online]. Available: http://www.k-wave.org/manual/k-wave_user_manual_1.1.pdf

[227] R. J. McGough, T. V. Samulski, and J. F. Kelly, “An efficient grid sectoring method for calculations of the near-field pressure generated by a circular piston,” *J. Acoust. Soc. Am.*, vol. 115, no. 5, pp. 1942–1954, 2004, doi: 10.1121/1.1687835.

[228] G. F. Pinton, J. Dahl, S. Rosenzweig, and G. E. Trahey, “A heterogeneous nonlinear attenuating full- wave model of ultrasound,” *IEEE Trans. Ultrason. Ferroelectr. Freq. Control*, vol. 56, no. 3, pp. 474–488, Mar. 2009, doi: 10.1109/TUFFC.2009.1066.

[229] I. M. Hallaj and R. O. Cleveland, “FDTD simulation of finite-amplitude pressure and temperature fields for biomedical ultrasound,” *J. Acoust. Soc. Am.*, vol. 105, no. 5, pp. L7–L12, Mar. 1999, doi: 10.1121/1.426776.

[230] G. F. Pinton, “Subresolution Displacements in Finite Difference Simulations of Ultrasound Propagation and Imaging,” *IEEE Trans. Ultrason. Ferroelectr. Freq. Control*, vol. 64, no. 3, pp. 537–543, Mar. 2017, doi: 10.1109/TUFFC.2016.2638801.

[231] E. Martin, J. Jaros, and B. E. Treeby, “Experimental Validation of k-Wave: Nonlinear Wave Propagation in Layered, Absorbing Fluid Media,” *IEEE Trans. Ultrason. Ferroelectr. Freq. Control*, vol. 67, no. 1, pp. 81–91, Jan. 2020, doi: 10.1109/TUFFC.2019.2941795.